DISSERTATION
submitted to the
Combined Faculties for the Natural Sciences and for Mathematics
of the Rupertus Carola University of
Heidelberg, Germany
for the degree of
Doctor of Natural Sciences

presented by
Diplom-Physiker Hans Graf
born in Öhringen

Oral examination: April 21st, 2004

Experimental Investigations on Multiphase Phenomena in Porous Media

Referees: Prof. Dr. Kurt Roth
Prof. Dr. Peter Bastian

Experimentelle Untersuchungen von Mehrphasenphänomenen in porösen Medien

Die Beschreibung des Transports von Wasser und gelösten Stoffen in porösen Medien basiert traditionell ausschließlich auf den hydraulischen Eigenschaften. Da für den ungesättigten Fall aber Wasser und Luft gleichzeitig denselben Porenraum teilen, ist eine genauere Untersuchung der Gasphase notwendig, um ihren Einfluss auf die grundlegenden Prozesse (Phasenkontinuität, Hysterese, Phaseneinschluss,...) speziell nahe Wassersättigung zu verstehen. Hierfür wurde eine Apparatur zur experimentellen Bestimmung der hydraulischen Eigenschaften mittels eines transienten Experiments dahingehend erweitert, dass simultan die Bestimmung der wichtigsten Gasflussparameter möglich war. So konnten Kontinuität und Leitfähigkeit der Gasphase an Laborsäulen bestimmt werden. Die Auswertung der hydraulischen Daten erfolgte mittels inverser Modellierung. Darauf basierend wurden die pneumatischen Eigenschaften mit verschiedenen Gasleitfähigkeitsmodellen simuliert.

Die Möglichkeiten der simultanen Bestimmung hydraulischer und pneumatischer Eigenschaften wurden an künstlichen porösen Medien aus gesintertem Glas demonstriert. Ein Vergleich der Messungen mit Luftleitfähigkeitsmodellen hat die Notwendigkeit einer Reskalierung der effektiven Luftsättigung zur Berechnung der Leitfähigkeit gezeigt.

Anhand verschiedener homogen und heterogen geschütteten Sandpackungen konnte der Einfluss der Struktur auf die hydraulischen und pneumatischen Materialeigenschaften verdeutlicht werden. Zwei pathologische Strukturen wurden rein hydraulisch und zusätzlich auch noch pneumatisch analysiert. Die Kombination beider Messmethoden ermöglichte Rückschlüsse auf die grundlegenden Strukturelemente der Proben.

Experimental Investigations on Multiphase Phenomena in Porous Media

Modeling of water flow and solute transport in porous media is typically based on the water dynamics only, while the gaseous phase is neglected. Since the two fluids share the same pore space a particular investigation of the gaseous phase is mandatory to understand its influence on the basic processes (continuity, hysteresis, entrapment,...) especially near water saturation.

For the multiphase measurements an existing multistep outflow setup for determination of hydraulic properties with laboratory sized columns, was improved by an additional airflow measurement device where gas phase continuity and conductivity could be measured simultaneously. Measured hydraulic data was analyzed by inverse modeling on which the pneumatic data analysis was based. Several gas conductivity models were tested.

The possibilities of a combined measurement of hydraulic and pneumatic properties were demonstrated with artificial porous media made of sintered glass. The comparison of measurement and simulations of air conductivity showed the necessity of a rescaling of the effective air saturation for predictions.

The influence of the sample structure on the hydraulic and pneumatic properties was illustrated with several homogenous and heterogeneous samples of repacked sands. The differences between purely hydraulic and combined measurement could be shown with experiments carried out with two pathologic structures. For this samples the basic structure elements could be detected by the combination of hydraulic and pneumatic measurements.

Contents

List of Figures

List of Tables

List of Symbols

This list contains the most important symbols used. Where possible, a reference (equation and page number) is given and the dimension is indicated in brackets.

The mathematical structure of symbols is indicated by their typographical appearance:

a	scalar
$\mathbf{a}$, $\widehat{\mathbf{a}}$	vector, unit length vector
A	tensor
sin	standard function

Subscripts usually refer to a component of a vector (x, y, z, or 1, 2, 3) or to the phase (a, w, s).

The arguments of functions are suppressed if they are clear from the context, e.g., $\partial_x f$ instead of $\partial_x f(x)$. They are written, however, if the dependence on an argument is emphasized, e.g., $K_d(C_w)$ for a nonlinear adsorption isotherm. Similarly, derivatives are written as shorthand operators: ∂_x, ∂_{xx} for the first and second partial derivative with respect to x, respectively, and d_t for the total derivative $\partial_t + \mathbf{v} \cdot \nabla$ with respect to time. If the derivative is to be emphasized, the long form $\frac{\partial \diamond}{\partial x}$ is used.

Sign Convention

The normal vector $\mathbf{n}$ on the surface of some volume points outwards. The vertical (z) axis points downward, in the direction of the acceleration of gravity. Its origin is typically chosen at the soil surface. Accordingly, z is called the depth.

Lowercase Latin Symbols

b	Klinkenberg parameter	2.56 37
h	hydraulic head [L]	2.15 21
j_a	volumetric air flux [$\mathrm{L\,T^{-1}}$]	3.1 52
j_w	volumetric water flux [$\mathrm{L\,T^{-1}}$]	2.32 27
k_a	pneumatic conductivity [$\mathrm{L\,T^{-1}}$]	2.42 34
k_a^*	slip enhanced pneumatic permeability [$\mathrm{L^2}$]	2.56 37

$k_{a,c}$	pneumatic conductivity of entire column [$\mathrm{L\,T^{-1}}$]	3.9 63
$k_{a,n}$	pneumatic conductivity of a single node [$\mathrm{L\,T^{-1}}$]	3.9 63
k_i	intrinsic permeability [$\mathrm{L^2}$]	2.33 28
$k_{r,a}$	relative pneumatic conductivity [-]	2.46 35
$k_{r,w}$	relative hydraulic permeability [-]	2.45 35
k_w	hydraulic conductivity [$\mathrm{L\,T^{-1}}$]	2.37 30
m	van Genuchten parameter	2.15 21
n	van Genuchten parameter	2.15 21
p_a	pressure in air phase [$\mathrm{F\,L^{-2}}$]	2.6 11
p_c	capillary pressure [$\mathrm{F\,L^{-2}}$]	2.6 11
p_e	entry pressure [$\mathrm{F\,L^{-2}}$]	2.12 20
p_w	pressure in water phase [$\mathrm{F\,L^{-2}}$]	2.6 11
r	pore radius [L]	2.7 12

Uppercase Latin Symbols

$\mathsf{K}_{a,sat}$	saturated pneumatic conductivity [$\mathrm{L}T^{-1}$]	2.67 43
$\mathsf{K}_{w,sat}$	saturated hydraulic conductivity [$\mathrm{L}T^{-1}$]	2.32 27
P_d	domain dependent factor [-]	2.25 25
$\overline{R}$	mean pore radius [L]	2.39 34
S_a	air phase saturation [-]	2.2 9
$S_{a,e}$	effective air phase saturation [-]	2.64 42
$S^*_{a,f}$	effective mobile air phase saturation [-]	2.60 39
$S_{a,r}$	residual air saturation [-]	2.12 20
$S_{a,t}$	effective trapped air phase saturation [-]	2.57 39
S_e	effective water saturation [-]	2.12 20
S_w	water saturation [-]	2.1 9
$S_{w,r}$	residual water saturation [-]	2.12 20
$S_{w,s}$	maximum water saturation [-]	2.12 20

Lowercase Greek Symbols

α	van Genuchten parameter [$\mathrm{L^{-1}}$]	2.15 21
γ	contact angle [$^\circ$]	2.5 10
η_a	viscosity of air [$\mathrm{F\,T\,L^{-2}}$]	2.70 44
η_w	viscosity of water [$\mathrm{F\,T\,L^{-2}}$]	2.33 28

θ_a	volumetric air content [-]	2.2 9
$\theta_{a,ea}$	air content at emergence point of air phase [-]	2.64 42
$\theta_{a,r}$	residual air content [-]	2.38 34
$\theta_{a,s}$	maximum air content [-]	2.38 34
θ_w	volumetric water content [-]	2.1 9
$\theta_{w,ew}$	water content at emergence point of water phase [-]	2.63 42
$\theta_{w,r}$	residual water content [-]	2.1 9
$\theta_{w,s}$	saturated water content [-]	2.38 34
θ_Δ	saturation at reversal point [-]	2.25 25
λ	Brooks and Corey parameter	2.12 20
ρ_a	mass density of air [$\mathrm{M\,L^{-3}}$]	2.70 44
ρ_w	mass density of water [$\mathrm{M\,L^{-3}}$]	2.33 28
σ_{as}	surface tension of air with respect to solid [$\mathrm{M\,T^{-2}}$]	2.5 10
σ_{wa}	surface tension of water with respect to air [$\mathrm{M\,T^{-2}}$]	2.5 10
σ_{ws}	surface tension of water with respect to solid [$\mathrm{M\,T^{-2}}$]	2.5 10
τ	tortuosity parameter	2.41 34
ϕ	porosity [-]	2.1 9
ψ_g	gravitational potential [$\mathrm{ML^{-1}T^{-2}}$]	2.8 12
ψ_m	matric potential [$\mathrm{ML^{-1}T^{-2}}$]	2.9 12
ψ_s	osmotic potential [$\mathrm{ML^{-1}T^{-2}}$]	2.9 12
ψ_{tp}	tensiometer potential [$\mathrm{ML^{-1}T^{-2}}$]	2.9 12

Measurement of air conductivity as a function of water content is a promising tool for obtaining new information useful in analyzing problems of aeration as well as infiltration and drainage in soils. However it is a tool which soil scientists seldom use and has never been developed for routine use. *(A. T. Corey, 1986)*

1 Introduction

Investigation of multiphase flow in porous media is important in many branches of science and engineering. In the technical field, this includes blast furnaces, catalytic converters, or fuel cells like the low temperature direct methanol fuel cells where methanol, hydrogen and oxygen share the pore space of the reforming membrane. In the field of bio reactors, the porous medium is the substrate for bacteria which have to be "fed" by fluids and gases, transforming them in their specific ways. Historically, the petroleum industry was one of the earliest interested in a detailed description of multiphase phenomena. Crude oil, natural gas, and water share the pore space in the deposits and a distinct knowledge of the basic processes could directly increase the efficiency of exploitation.

Huge fields of multiphase research are the agronomic and environmental sciences. These include groundwater hydrology and soil science with their distinct branches. The dynamics of water movement in soil is of great importance for many issues of environmental and economic interest, for instance, for the quantity and quality of groundwater, for agricultural production, or for the design and management of hazardous waste sites. The governing equations which describe the dynamics of water movement are highly nonlinear due to the strong increase of soil's hydraulic conductivity with water saturation. The problem arises most drastically with infiltration of water, the phenomenon of greatest interest for the transport of dissolved chemicals (fertilizers, pesticides, heavy metals, gasoline additives, ...) where an important characteristic is the residence time of the solute in the highly reactive root zone. Infiltration leads to the movement of roughly the same volumes of water and air in opposite directions. For this reason, the system must be understood quantitatively well near water saturation.

The dynamics of soil air has been of secondary interest to soil and agricultural scientists, because the gas exchange between soil and the atmosphere was thought to be unimportant for most phenomena. The attention was renewed, when the pollution of soil by organic compounds had to be removed. The pollutants, which came from accidental spills or leakage in production plants or waste deposits, infiltrated into the unsaturated zone where they would threaten agricultural acreages or the groundwater. As many of these chemicals are only slightly soluble in water but highly volatile they could be transported significantly by advective components of the air phase, therefore, an understanding of the air phase as well as of the water phase has become important.

Motivation

The usual approach for description of unsaturated fluid flow involves the assumption that the air phase essentially remains at a constant pressure, equal to atmospheric; the system is then reduced to the consideration of the water phase only. This approach is called the Richards approximation (Richards 1931) and is the standard method in soil science. Combined with some parameterizations for the material properties, specifically for the soil water characteristic and for the hydraulic conductivity (e.g., Brooks and Corey 1966, van Genuchten 1980, Burdine 1953, Mualem 1976) it is possible to solve the resulting system of equations numerically. It has been shown to be a good approximation for most applications, however, there are some situations where air phase can significantly retard the movement of the water phase.

Obviously, there exists an important domain near complete water saturation where the assumptions of the Richards equation are violated and where a complete multiphase formulation is mandatory. While this insight is not new, its implications have not often been appreciated. They affect the simulation of water movement near saturation as well as the popular inverse methods (Kool et al. 1985, van Dam et al. 1994) for estimating hydraulic properties. The latter affect appears particularly severe, since, incorrectly prescribing the Richards equation as the dynamics model, can fold all structural deviations into the estimated parameter functions. As mentioned above in a more extended perspective, the problem raised is also relevant to other issues, for instance for the aeration of soil and for the movement of non-aqueous phase liquids.

Since different multiphase modeling approaches have been developed during the last decades there is an need for data to support mathematical descriptions of consistent parametric two phase flow models.

In this study, a versatile experimental approach for studying water and air movement in nearly water-saturated porous media is demonstrated. For determination of hydraulic material properties the transient method of multistep outflow is combined with an inverse parameter estimation approach. The aim of the experimental design, is the simultaneous measurement of air conductivity within a running multistep outflow experiment. The method of simultaneous measurement is used as a tool for fast determination of hydraulic and pneumatic properties of porous media. With this new setting, the influence of soil air on water transport, especially the range of saturation where the Richards approximation could be applied, should be investigated. Pneumatic conductivity of the sample can be determined to get an insight in gas transport properties. For this study, the simultaneous measurements are applied to laboratory size columns of different types.

A major experimental hurdle is to keep the pore space stable for a prolonged time. This is difficult for high water saturations because clay minerals can cause soil swelling and the typically high water fluxes cause internal erosion. In addition, there is always the problem of microbiological growth and associated clogging of soil

pores. Since these processes cannot be suppressed completely in soils, the problems are circumvented altogether by working with columns made of sintered glass beads which are rigid by construction and which can be treated with chemicals to both prevent the growth of microorganisms and to remove possible precipitates.

The influence of the structure of a sample on multiphase processes is examined by a set of different homogeneous and heterogeneous repacked sand columns. Hysteresis of the hydraulic and pneumatic relations can be investigated at different scales with a focus on textural and structural influence on the total effect.

The measured air conductivity data is simulated with three types of models which are based on different fundamental assumptions. A comparison of the simulation results show the advantages of the different approaches and the limitations of each air conductivity model.

Experimental Background for Multiphase Phenomena

Investigations of multiphase phenomena have been subjected to the inquiry of petroleum engineers in the first half of the 20th century when the parallel flow of oil, gas, and water in oil reservoirs was investigated (Muskat and Meres 1936, Leverett 1939). Their model was based on the assumption of local equilibrium, according to which the relative phase conductivities and the capillary pressure could be expressed through the universal functions of local saturation.

In the soil science, the Richards approximation could conveniently describe fluid transport with a relatively simple model, therefore much investigation was carried out on the soil water phase only. With the simple parameterizations of the functional relationships of hydraulic properties it has been possible to simulate water-flow in unsaturated porous media and come to a good agreement with measured data (Brooks and Corey 1966, van Genuchten 1980, Burdine 1953, Mualem 1976).

The influence of the soil air phase has been subjected to various hysteresis theories in which it was not possible to neglect soil air. The change of hydraulic conductivity with the history of the examined samples was reported by Kozeny (1927), who explained the hysteresis effect by air entrapment. The development of entrapped air was described by Miller and Miller (1956) for the different behavior of air-water interfaces during drainage and imbibition of a porous medium. Several studies were carried out for the investigation of the influence of hysteresis on the moisture retention characteristic (e.g. Topp 1969, Parlange 1976). The models developed for this phenomena are reviewed in Viaene et al. (1994). The influence of entrapped air on the conductivity relations were also investigated by different authors. The hysteresis of the pressure-conductivity relation was obvious as it is directly connected to the pressure-saturation relation. Hysteresis of the saturation-conductivity relation has been observed with two different results. The experimental data of Poulovassilis (1969) and Topp and Miller (1966) found a hysteretic behavior, whereas Nielsen et al. (1986) and Kool and Parker (1987) found negligible influence of hysteresis on the relation.

A mathematical description of hysteretic water flow was developed by Parker et al. (1987) and Lenhard and Parker (1987) for both the hysteretic retention characteristic and the saturation-conductivity relation. Their model was based on a scaling of the distinct phase saturations, where the entrapped part of a phase was separated from the mobile part. Experimental observation of air entrapment effects on hydraulic functions confirmed this approach (Stonestrom and Rubin 1989a) and demanded an explicit consideration of the soil air phase in experiments (Faybishenko 1995, Fischer et al. 1997, Dury et al. 1999).

Since transient methods for soil analysis became popular during the last decade the so-called dynamic effects have been revived. The effect was reported by Topp et al. (1967) who found differences in pressure-saturation relationship for static, steady state flow and transient flow measurements. At a given pressure water contents were significantly higher for the static, or steady state conditions than for the transient. A review of the different studies in this field can be found at Hassanizadeh et al. (2002). The mechanisms which lead to dynamic effects in water flow can be summarized:

- Dynamic effects have been investigated experimentally at different scales. At the pore scale Lu et al. (1994) have found for the capillary rise of water that the fluid exhibits a jump behavior, which crucially depends on the wetting state of the pore surface.

- Water entrapment during drainage: water in smaller pores is isolated, which results in larger saturation. Relative conductivity is expected to be lower, as the mobile portion of water is decreased. This is in contrast to observations (Wildenschild et al. 2001).

- Pore water blockage near the bottom boundary during drainage. At large pressure steps the lower layer of the sample is drained and, assuming air availability, a capillary barrier is built (Gee et al. 2002). Relative conductivity is expected to be lower.

- Wildenschild and Hopmans (1999) investigated the rate dependence of unsaturated hydraulic properties, performing one-step and multistep outflow experiments. They found that water content was higher for fast drainage with large pressure steps. Dynamic effects were less significant in fine-textured media.

- Air entrapment for drainage at high saturation. The water can only be drained if air can replace it. For non-continuous air phase, water cannot be drained effectively which results in higher saturation under dynamic conditions.

- Microscale air phase displacement was investigated by Mortensen et al. (2001) in a two-dimensional sample, where the non-uniqueness of flow properties was a result of fast air finger flow and slower air back-filling.

- Friedman (1999) described the differences between static and transient measurements by the dynamic contact angle instead of a static one. For a given capillary pressure, the degree of liquid saturation decreased with increasing liquid flow velocity, for wetting processes and vice versa for drainage.

With this study, hydraulic and pneumatic properties of porous media will be examined simultaneously within one single transient experiment in order to have a full set of material properties. The complex procedures of determination of either the hydraulic or the pneumatic properties will be simplified to get an instrument which can be routinely used.

2 Theory of Immiscible Fluids in Porous Media

To compile the theoretical and experimental framework for water- and gas-transport in unsaturated porous media, there is a need for some definitions of porous media, the scales of interest, and the conceptual models which are used to describe multiphase processes on the respective scales (Sections 2.1 - 2.3). A specific effect of multiphase processes is the history dependence of the system. The hysteresis effects on hydraulic functions is examined more closely in Sections 2.2.4 and 2.3.5.

The parameterizations which describe the soil hydraulic and pneumatic properties are introduced in Section 2.4 followed by the mathematical description of multiphase flow processes in Section 2.5.

2.1 Porous Media

Porous media occur in various forms, e.g. as soil, rock, sand, paper, porcelain, or any kind of filter. These materials are characterized by their microscopic structure which exhibit a large number of void spaces. Voids which are interconnected, are called pores and a network of pores enable fluids to occupy them and move through the pore system. Multiphase flow processes in the case of this study describe the flow of the two immiscible fluids water and air, which can be observed at different length scales, where flow processes are governed by specific fundamentals. Transitions between scales are possible if a material property, which can be observed at a small scale, can be averaged to get an effective property at the larger scale, e.g. the surface tension at the micro scale has an impact on the capillarity at the pore scale (see equation 2.5). Figure 2.1 gives an overview of the typical length scales (molecular, pore, and continuum scale) which are common in literature. With a focus on fluid flow, each scale has a specific structure, which are the elements comparable in size with the scale of observation, and the texture, which describes the influence of elements much smaller than the observed scale (Vogel and Roth 2002).

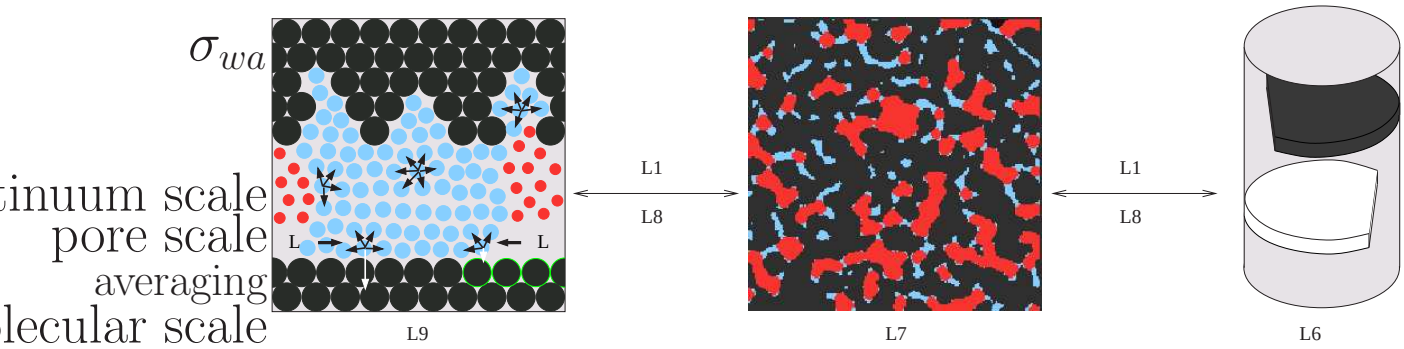

Figure 2.1: Typical length scales in porous media (blue: water; red: air; black: solid)

Molecular Scale

Molecular scale in this context means a length scale of Ångstrøm (10^{-10}m). At this scale, the focus is on molecular interactions between the fluid particles and the solid material (Figure 2.1 left). Forces between the particles are primary based on electrical interactions. The interactions lead to effective properties like wetting behavior of the matrix, surface films, and sorption of water and solutes. Adsorption of water in films at the solid surface is influenced by surface properties. Besides the influence of hydrophobic or hydrophilic surfactants, the geometry of the surface has an impact on the evaporation of water as the radii of the menisci reduce the steam pressure of water above the water air interface. For smooth surfaces, the connectivity of water can be lost during the drainage process and "pendular rings" which are isolated portions of water, will develop. This effect is expected to be much less pronounced in the case of a rough surface which offers edges and wedges for the water to leak out (Dullien et al. 1988).

Pore Scale

Pore scale is within the scope of micrometers (10^{-6}-10^{-3}m). The individual molecules are averaged to an ensemble of particles, which is described in a statistical way (Figure 2.1, center). The molecular scale state variables (e.g., velocity, molecular mass, etc.) are averaged to pore scale ensemble properties like density, pressure, or temperature.

With the known geometry of the solid phase and the accompanying surface properties, the motion of the fluid phases can be described by the Navier-Stokes equation. This depends on the mean free path length being much smaller than the diameter of the pores. Numerical solution methods for this approach are limited by the speed of computers available to small sample volumes because of the high spatial resolution required.

Alternatively, processes can be described with pore network model simulations using simplified models and geometry, e.g. the Young-Laplace equation applied to a

capillary network. These are a kind of shortcut in determining effective parameters, as they reduce the porous medium and the fluids to a few effective properties (a review of several pore scale modeling approaches can be found in Blunt (2001)).

Continuum Scale

Figure 2.1 (right) shows an example for the continuum scale which is represented by a column scale sample. Phases are no longer assigned to special locations. They are averaged and distributed over the whole space with their specific fractions. Influence of the pore geometry and surface properties and interactions between fluids are included in the relevant effective state variables. Effective properties are influenced by the texture and the structure of the sample. The example shows a column with three different constituents which have their respective material properties. Sampling of these materials result in new effective material properties of the entire column.

2.1.1 REV, Averaging, and Continuum Approach

Extensive variables (e.g. bulk density or phase contents of a soil sample) have to be averaged on a specific sample volume. If the mean value becomes constant with increasing volume of observation, i.e. the influence of microscopic structure elements can be described by a macroscopic property, then the value where it has become stable is called the "representative elementary volume" (REV) (Bear 1972). This concept is necessary for the examination of larger soil volumes where the specific phase geometries become too complex for explicit observation. Small scale variables

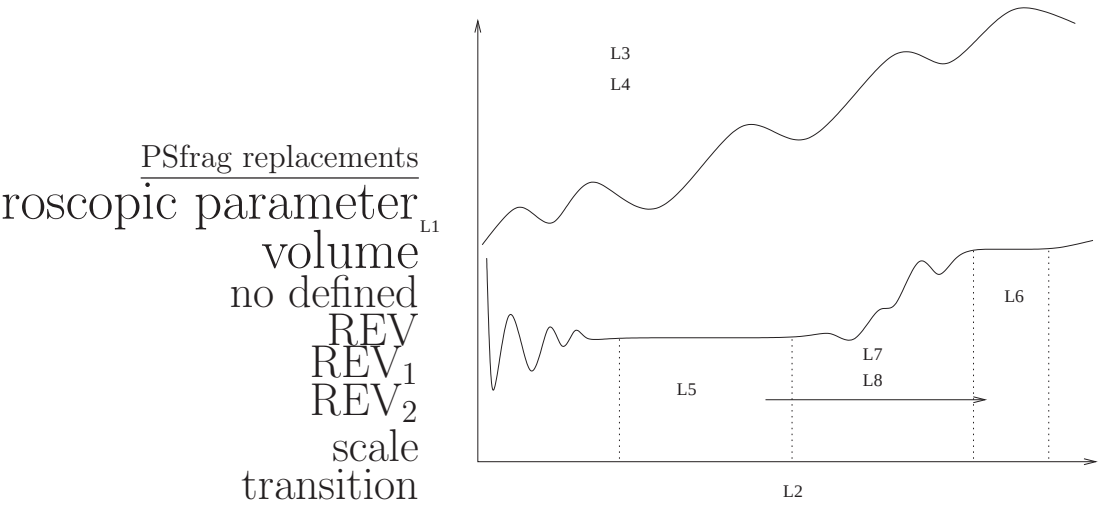

Figure 2.2: Definition of a representative elementary volume. The threshold when the observed value is constant with increasing volume is called an REV with respect to the measured property.

are averaged to get effective material property at the scale of interest. Different variables can have different REVs in the same porous medium. For some parameters there are several plateaus in the parameter-value vs. observed-volume curve. This means that they have different REVs at different scales. Figure 2.2 shows a soil with a discrete hierarchical structure resulting in REV_1 and REV_2. Knowledge of an REV at the observed volume is necessary in making transitions between different scales possible. For the example in Figure 2.1 (right) the first REV could be assigned to the texture of the single materials and the second to the entire column.

The upper curve in Figure 2.2 shows another example. For this parameter there is no REV within the range of the observed volumes. Averaging methods used for transitions between scales cannot be applied here and maybe a REV can be found by further increasing the sample volume.

2.1.2 Porosity, Liquid Content and Saturation

In an unsaturated porous medium, two or more fluids share the same pore space. Each fluid occupies its respective partial pore volume fraction. The most common approach is to distinguish between wetting and non-wetting fluids. For this study the fluids of interest are water, the wetting fluid which is indexed as w, and air, the non-wetting fluid denoted as a. In this two-phase system, the volume fraction of the total pore volume (defined as the porosity ϕ of the medium) occupied by one of the liquids is called saturation S.

The volumetric water content is defined as:

$$\theta_w = S_w \phi \quad [-] \tag{2.1}$$

The volumetric air content is:

$$\theta_a = S_a \phi \quad [-] \tag{2.2}$$

with:

$$\sum_i \theta_i \equiv \phi \quad \text{where} \quad i = a\,;\, w \tag{2.3}$$

and

$$\sum_i S_i \equiv 1 \quad \text{where} \quad i = a\,;\, w \tag{2.4}$$

2.2 Capillarity

As the macroscopic distribution of water and air in porous media depends on microscopic effects, a zoom into the smaller scales with their governing processes is necessary.

2.2.1 Micro Scale Effects

Surface Tension

Forces between molecules of a single phase are cohesive forces. For molecules at the interface between two immiscible fluids, the forces are stronger within its own fluid than to the other fluid. The effect is sketched in Figure 2.1 (left) where the forces on several fluid particles are indicated by arrows. The forces on the particle in the center is balanced whereas the particle at the left water-air interface is drawn back into the water phase. This imbalance of forces gives the surface its specific curvature, since the system as a whole has the tendency to reach a condition of minimum energy. The enlargement of the surface A demands some energy E_A which is stored in the surface and is given back when the surface area is reduced. The energy per area is defined as specific surface tension σ (Gerthsen et al. 1992):

$$E_a = \sigma \cdot A$$

2.2.2 Capillarity Effects at the Pore Scale

Wettability

Different fluids (air, water, oil, etc.) show different adsorption behavior on the soil matrix. The microscopic interactions are summed up to the macroscopic surface property which is called wettability.

Figure 2.3 shows two immiscible fluids in contact with a solid surface. The angle between the fluid-fluid interface and the solid surface is called the contact angle which is defined for steady state conditions as:

$$\gamma = \frac{\sigma_{as} - \sigma_{ws}}{\sigma_{wa}} \tag{2.5}$$

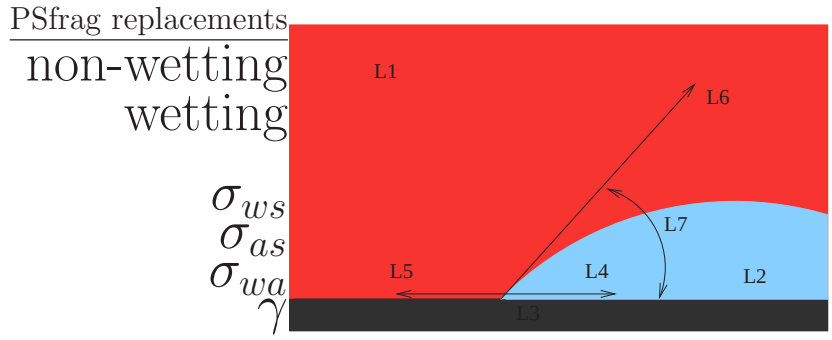

Figure 2.3: Definition of surface tension and contact angle in a three phase system

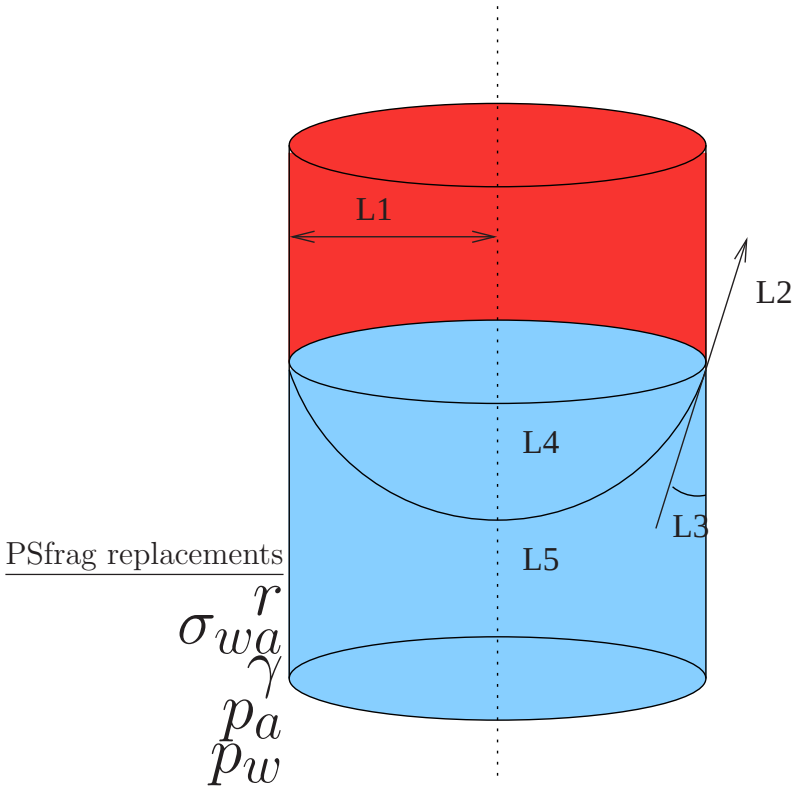

Figure 2.4: Surface element in a capillary

The indices s, a, and w, represent the solid, air, and wetting phase, respectively. For example σ_{wa} is the surface tension of water with respect to air. Equation 2.5 is known as Young's equation. If $\frac{\sigma_{sn}-\sigma_{sw}}{\sigma_{nw}} > 1$, it is not possible to have a steady state, as the wetting fluid spreads over the solid surface. For a contact angle γ (Figure 2.3) less than $90\,^\circ$ the fluid is called wetting w, for larger contact angles it is called non-wetting phase, a (air) (Bear 1972).

Another aspect related to wettability is the speed at which fluids spread over a solid surface. This speed is affected by the surface tensions and viscosity of the fluids. Spreading speed is increased by lower surface tensions or by lower viscosities.

Capillary Pressure

At the pore scale the porous medium can be idealized as an accumulation of capillary tubes. If two immiscible fluids are in contact with each other and equilibrium is reached, the pressure of the non-wetting phase p_a at the interface between the fluids is greater than the pressure of the wetting phase p_w (see Figure 2.4). The difference between the phase pressures of the two fluids is called capillary pressure:

$$p_c = p_a - p_w \tag{2.6}$$

The Young-Laplace equation for capillarity defines the curvature dependent capillary pressure as:

$$p_c = \frac{2\sigma_{wa}\cos\gamma}{r} \tag{2.7}$$

with σ_{wa} surface tension of water with respect to air
γ contact angle
r radius of the observed meniscus

Capillary pressure depends on the one hand on the geometric properties of the pore (radius r) and on the other hand on the surface tension (contact angle γ) which is a function of the chemical compositions of the fluids and the solid surfaces.

All the above assumptions were made under the precondition that there is only pure water in contact with simple solid surfaces. The influence of solutes in water or surfactants at solid surfaces is not incorporated in this view.

Potentials

Potential energy of soil water, the so-called soil water potential, is a summary of several partial potentials:

The gravitational potential is the energy density of water at a position z moved from a reference state z_0:

$$\psi_g = -\rho_w g(z - z_0) \quad \text{for} \quad \rho_w = const. \tag{2.8}$$

The tensiometer potential is the sum of hydrostatic potential, pneumatic potential, and matrix potential.

$$\psi_{tp} = \psi_h + \psi_p + \psi_m \tag{2.9}$$

Pneumatic potential is only necessary if air pressure in the porous medium is not at atmospheric pressure, i.e. air bubbles are entrapped and do not communicate with an air reservoir.

The osmotic potential is the energy density required for a change of solute concentration in a fluid. As mentioned above, only pure water has been used for this study which makes osmotic potential obsolete for further consideration.

2.2.3 Capillarity Effects at the Continuum Scale

In a multiphase system there exists a fundamental connection between saturations of the wetting phase and the non-wetting phase, and capillary pressure. Figure 2.5 shows a pore at two different capillary pressures p_{c_1} (solid) and p_{c_2} (dashed). For the pressure p_{c_1} the interfacial area has the curvature radius r_1 and the wetting phase

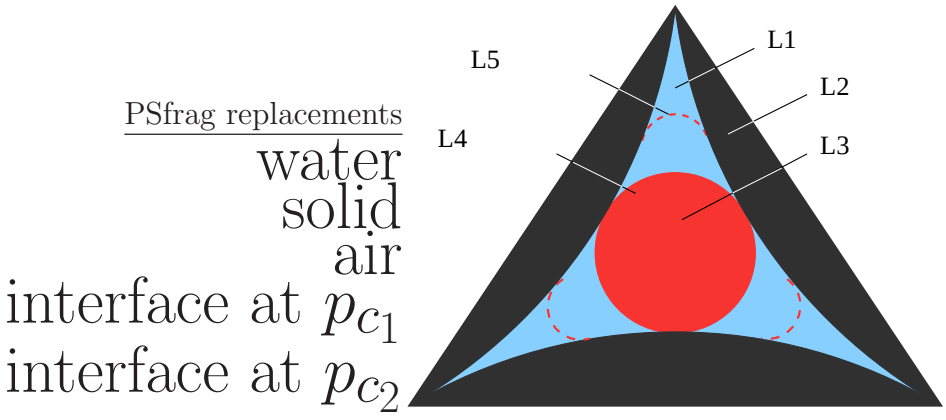

Figure 2.5: Model of pore cross-section with two different states of saturation of water, corresponding to the pressures p_{c_1} and p_{c_2} and their respective interfaces (Corey 1994)

saturation S_{w_1}. With decreasing capillary pressure ($p_{c_1} \rightarrow p_{c_2}$), the wetting phase is drawn back to that part of the pore with smaller dimensions and the new interface radius r_2 corresponds to smaller saturation S_{w_2}. Therefore, saturation is a function of capillary pressure. The pressure which is necessary to start drainage of a water-filled pore is called air entry pressure p_e. Since interconnected pores have different diameters, the desaturation of the pore space occurs in discrete jumps depending on the largest pore available for drainage (Corey and Brooks 1975).

Macroscale capillarity in analogy to the microscale capillarity is a function of surface tension σ, contact angle γ, and via pore radii r, of the pore geometry. This results in a relation between capillary pressure and saturation:

$$p_c = p_c(S_w) \tag{2.10}$$

which is the so-called soil water characteristic.

2.2.4 Hysteresis in Soil Water Retention Function

The soil water characteristic is not a unique static function since the $p_c(S_w)$ relationship depends on the pressure (or saturation) history. If the response of the porous system depends on the history of the driving forces which imply these responses, this kind of dependency is called hysteretic behavior. This means, in the case of the capillary pressure relation, that the drainage behavior (non-wetting phase is repelling the wetting phase) differs from the imbibition behavior (wetting phase is repelling non-wetting phase). To predict transport properties, knowledge of this pattern is necessary. The distribution of phase saturation has a strong impact on the flow paths available for solute displacement.

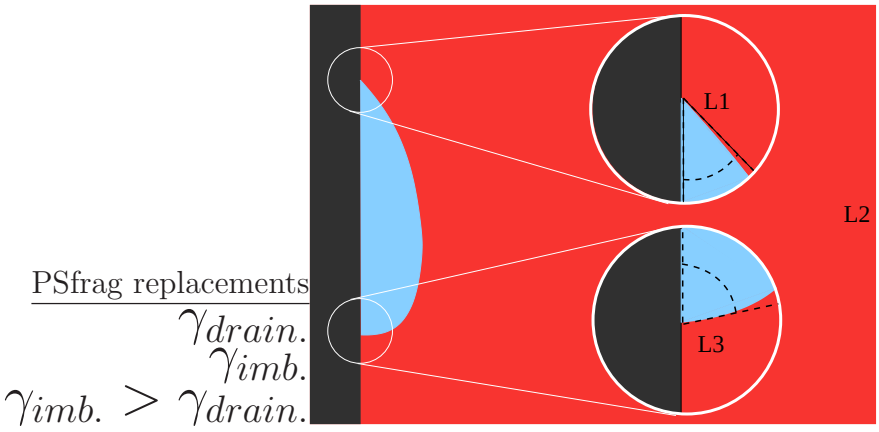

Figure 2.6: Raindrop effect visualizing dependence between contact angle and wetting front behavior. The drop is running down a homogeneous surface. The zoom on the right side shows the difference between the advancing (bottom) and receding wetting front (top).

The physical basics of hysteresis have to be viewed on different scales and their macroscopic results are the total of different effects.

Micro Scale Hysteresis

On the micro scale, the contact angle was the parameter including all surface fluid interactions (Figure 2.3). For the dynamic case, the correlation between contact angle and the mode of displacement is shown in Figure 2.6. The drop is running down a solid surface. At the lower end one can see the large contact angle of the advancing front, where the dry solid has to be wetted. At the upper end the receding contact angle is much smaller as the solid was originally wet. The effect is known as "raindrop effect". The difference between the static contact angel (Figure 2.3) and the dynamic one (Figure 2.6) strongly depends on the displacement velocity. For further details about the influence of dynamic contact angle see Friedman (1999).

Pore Scale Hysteresis

Pore scale hysteresis is the result of two major effects. The first, is the so-called "ink bottle effect", which is sketched in Figure 2.7. The two capillaries (a) and (b) each have their specific height of capillary rise. For capillaries with non-uniform diameter, saturation history has an impact on the height of capillary rise. Figure 2.7 (c) shows drainage of the irregular capillary. The receding water table is blocked at a pore neck. (d) shows the imbibition case, where the advancing water table is blocked by the pore body and the height of capillary rise corresponds to that of the larger tube (b). Although the same pressure is applied to all capillaries, the

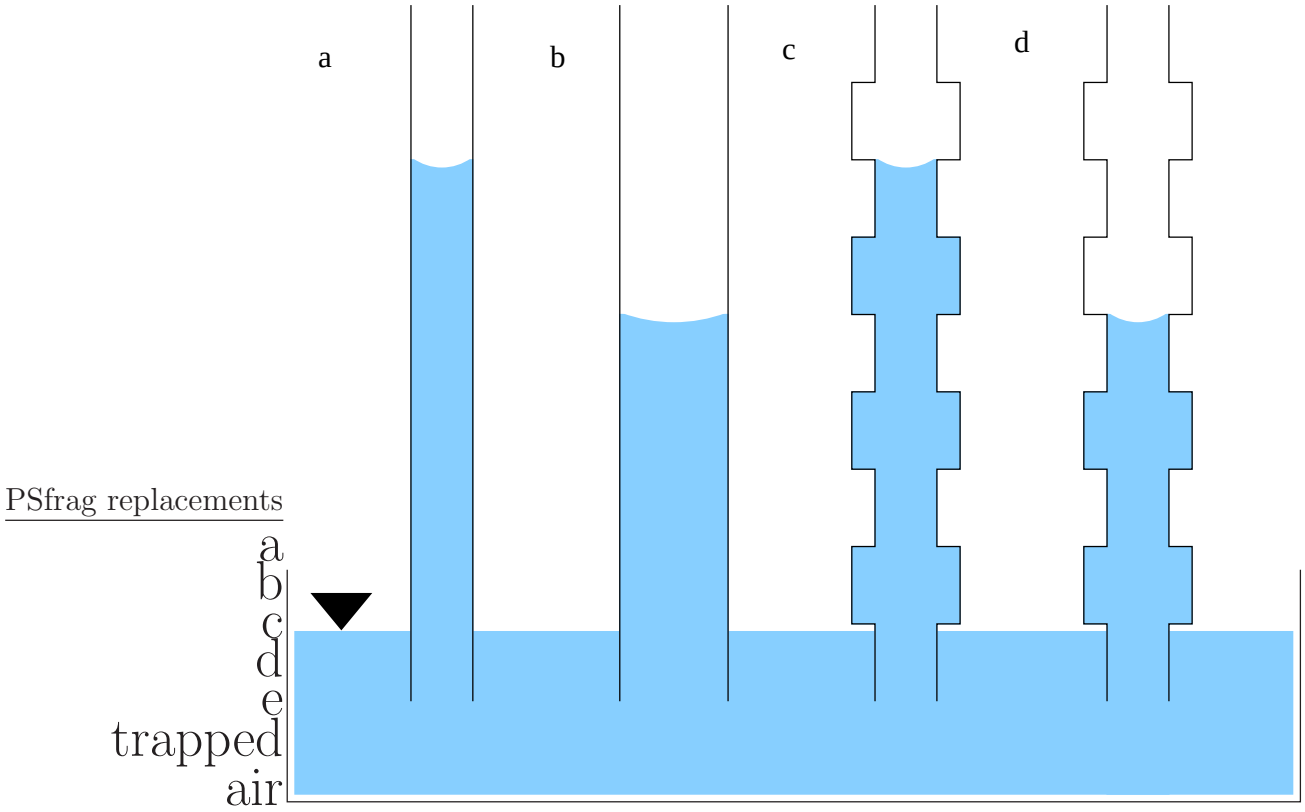

Figure 2.7: Model of drainage and imbibition heights of capillary rise. (a) Capillary rise in small tube equivalent to pore necks. (b) Capillary rise in large tube equivalent to pore bodies. For mixed pore diameters, capillary rise in drainage (c) differs from imbibition (d) (Dullien 1979).

drained tube (c) contains obviously more water than the imbibed (d).

The second effect, causing pressure saturation hysteresis, is phase entrapment. Displacement of one fluid by the other, can break the continuity of the displaced fluid by separating portions of it, which are then enclosed in the invading fluid. Two mechanisms which end in phase entrapment are sketched in Figure 2.8 and 2.9.

The "snap-off" effect describes an inclusion of non-wetting phase bubbles in the pore bodies. It depends on the surface properties (wettability) and on the ratio between the sizes of pore bodies and pore throats.

The effect of "by-passing" is shown in Figure 2.9 where an initially dry pore system is imbibed. The smaller pore is filled with water due to its capillarity, while air in the larger pore is separated from the air continuum.

Entrapment is not limited to the gaseous phase, as water cut off from the communicating liquid phase is also entrapped. This water is placed in small pores which

are surrounded by larger ones, or in "pendular rings" which are shown in Figure 2.5 as the p_{c_2} state.

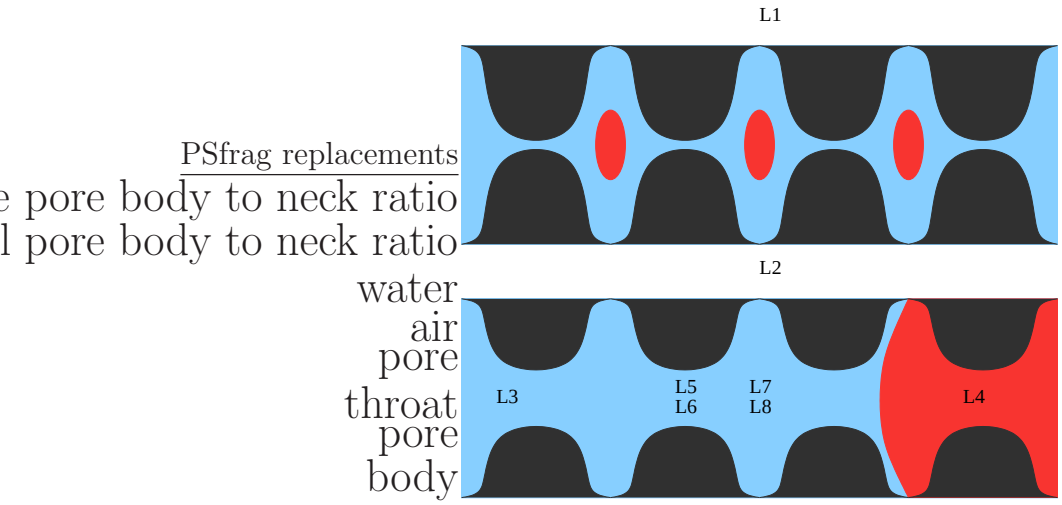

Figure 2.8: Influence of the pore geometry on the inclusion of a fluid caused by the "snap-off" effect. (Chatzis and Dullien 1983)

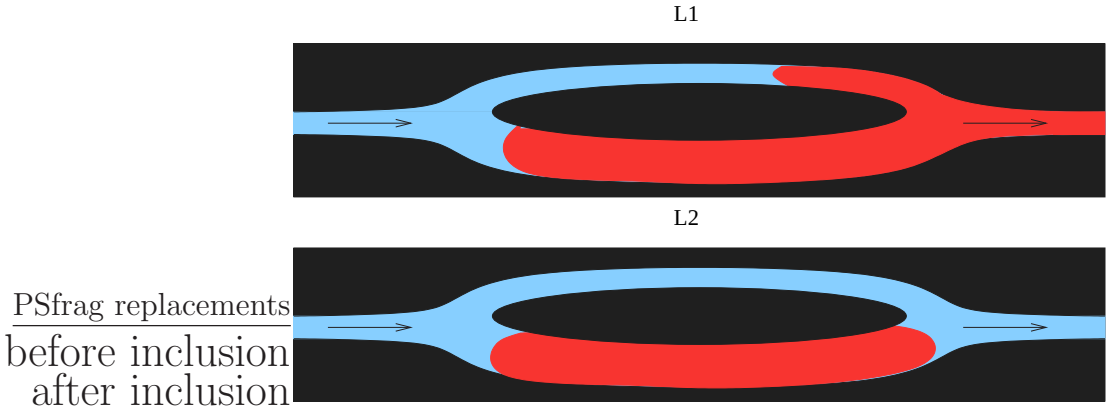

Figure 2.9: Influence of pore geometry on the inclusion of a fluid caused by the "by-passing" effect. (Chatzis and Dullien 1983)

Macroscale Hysteresis

Figure 2.10 shows the pressure saturation relation for a macroscopic soil sample ($\phi = 0.32$). The special cases of the hysteretic retention curves are classified in three categories: primary, main, and scanning curves with their respective drainage and wetting branches:

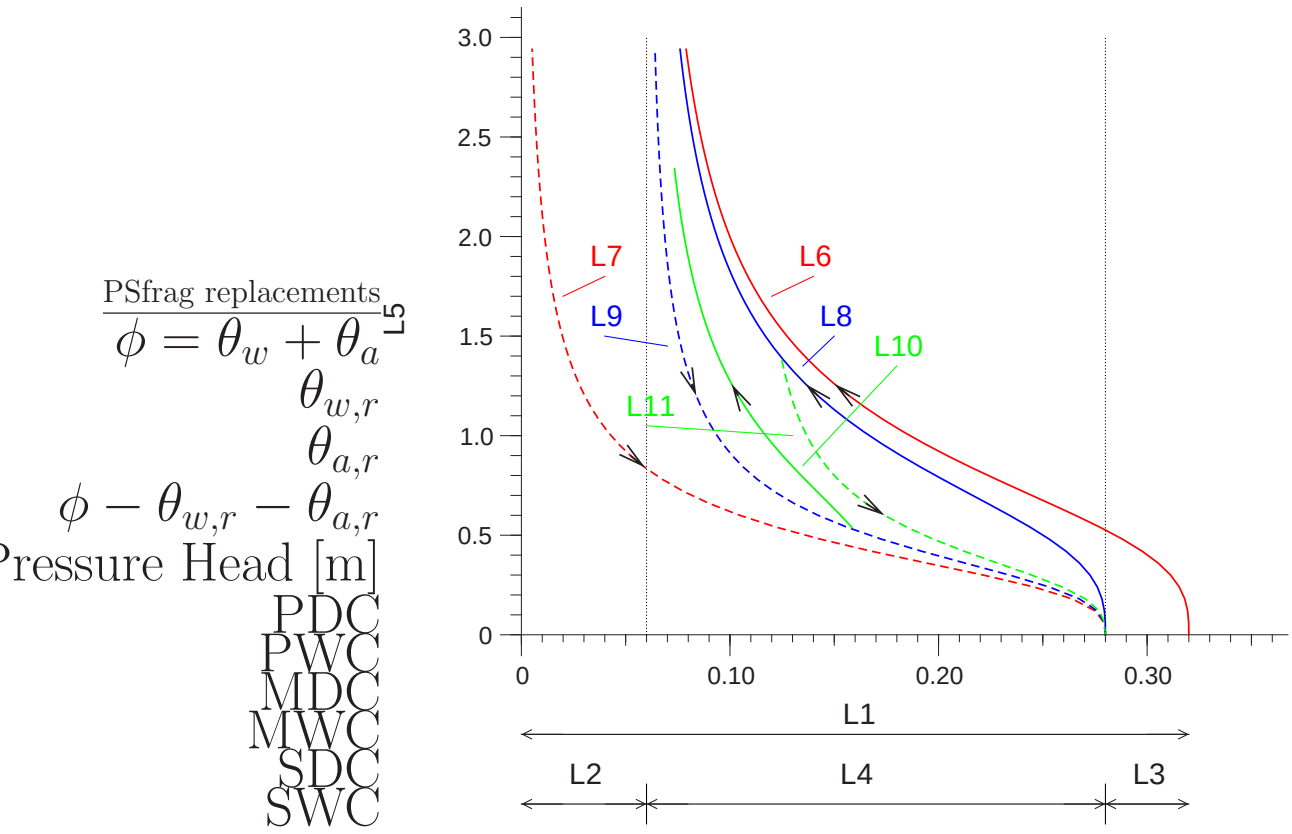

Figure 2.10: Hysteresis in the $p_c(S)$ relationship. Solid lines refer to drainage processes and dashed lines to imbibition. Primary curves (red) start with full saturation of the respective fluids, whereas main curves (blue) fix the range of measurement starting with unsaturated conditions. The scanning curves (green) can start at any point within the limits of PDC and PWC when the sign of $\partial h/\partial t$ changes.

- Primary drainage curve (PDC): The sample is fully saturated with water and the applied capillary pressure is $p_c = 0$. Decreasing capillary pressure starts drainage when pressure reaches the air entry value, p_e, which is the pressure corresponding to the largest pore connected to the air reservoir. Minimum saturation, the residual water saturation $\theta_{w,r}$ is reached, if any further decrease in capillary pressure results in a negligible decrease in saturation. It is a result of an unconnected water phase and the water remaining in the sample is associated with surface films or pendular rings. Since phase continuity is lost, it is not possible to remove this amount of water by a further decrease in capillary pressure.

  Primary wetting curve (PWC): The totally dry sample (complete air satura-

tion) is saturated with water by increasing capillary pressure. Due to phase entrapment effects, the maximum water content $\theta_{w,s}$ is less than porosity and the difference $\theta_{a,r} = \phi - \theta_{w,s}$ is the maximum residual air content which cannot be removed by increasing capillary pressure as phase continuity is lost.

- Main drainage and wetting curve (MDC, MWC): The main curves form the hydraulic limits of the fluid distribution. It is not possible to obtain fluid contents outside these limits by normal hydraulic fluid flow, i.e. fluid flow governed by Darcy's law. MDC and MWC approach each other asymptotically when $h \to 0$ and $h \to \infty$.

- Scanning drainage and wetting curve (SDC, SWC): Scanning curves are the typically measured retention curves of undisturbed soils in laboratory. They start at any point within the range derived by the main curves[1] and also end at any point.

The different ranges of water content and the resulting effective saturations are described by (Luckner et al. 1989):

$$S_w = \frac{\theta_w - A}{\phi - A - B} \tag{2.11}$$

with the scaling factors A and B which are summarized in Table 2.1 representing primary and main curves.

	PDC	PWC	MDC	MWC
A	$\theta_{w,r}$	0	$\theta_{w,r}$	$\theta_{w,r}$
B	0	$\theta_{a,r}$	$\theta_{a,r}$	$\theta_{a,r}$

Table 2.1: Values of the scaling factors A and B for PDC, PWC, MDC, and MWC.

Hysteresis influenced by macroscale structure elements

The effect of pressure saturation hysteresis is also caused by macroscale structures at the continuum scale. In samples with heterogeneous structure, a type of large scale "snap-off" can be observed. For example, a fine-textured lens should be embedded in a coarse-textured material. Drainage of this sample should be induced, by a fast decrease of capillary pressure to a value less than air entry pressure of the coarse material and higher than the air entry pressure of the fine material. Drainage of the coarse material could disconnect the fine lense from the water phase which would cause drainage by further decrease of capillary pressure to be impossible, or it could

[1] Investigations carried out with undisturbed soil samples usually do not start at full saturation of one phase and therefore measurement do not result in a primary curve.

drastically reduce hydraulic conductivity which would cause drainage to be very slow. For coarse-textured lenses embedded in fine-textured material the opposite effect is observed. During imbibition of an initially dry sample pneumatic contact from the lenses to the air reservoir is lost and air is entrapped within the lenses. Both effects occur even more in the fast transient multistep outflow experiments where diffusion of the involved fluids and phase transitions have only little impact.

2.2.5 Experimental Methods to Determine Pressure-Saturation Relation

There are several standard methods for determination of the pressure saturation relation. They can be sorted according to increasing precision:

- Long column: A long homogeneous column with a water reservoir at the lower end is allowed to reach equilibrium. Forces acting on the fluids are result of gravity and capillarity. Saturation is determined at several heights by slicing the sample. The discrete resolution of saturations is limited to a pressure range, limited by the height of the sample.

- Centrifuge: The small initially saturated sample is placed in a centrifuge, where it is turned around with a specific velocity. After some time the centrifugal and capillary forces reach equilibrium and the saturation can be determined. This method is good for determining residual wetting fluid saturation. The pressure range depends on the power of the centrifuge and the mechanical stability of the sample.

- Hanging water column: The sample is placed on a water saturated porous plate with a high air entry pressure. Pressure is applied via water phase by a water column of specific height. After reaching equilibrium saturation is measured gravimetrically. With this method a maximum water phase pressure of about $300\,\mathrm{cm}_{WC}$ [2] can be applied.

- Pressure cell: The sample is placed on a porous plate inside a pressure container. A high air pressure is applied to the container, which induces displacement of water. The system is allowed to reach equilibrium and saturation is measured gravimetrically. This method can be very time consuming as the equilibrium state is reached after many days (depending on actual saturation). With decreasing of the applied pressure (up to some ten bars), the state of water is not clear anymore which brings some difficulties in the interpretation of the results (Klute and Dirksen 1986).

[2] The water potential is indicated in cm_{WC} throughout this study, which is the equivalent of a hanging **w**ater **c**olumn.

- The Brooks' method (Brooks 1980) works the opposite way. Saturation is controlled by adding a defined portion of water to the sample. After reaching equilibrium the achieved capillary pressure is measured.

2.2.6 Empirical Descriptions for Pressure-Saturation Relation

The empirical approaches try to describe the measured data with a simple mathematical formulation with the aim of interpolating the retention curve between the measured data points. There are several models developed by Brooks and Corey (1964), Brutsaert (1967), Campbell (1974), van Genuchten (1980), Lenhard et al. (1993), etc.. In contrast to the purely empirical models, which could only be applied to a specific soil, these models fit experimental data by using material parameters which reflect the geometric structure of the pore space. Parameters are related to pore size distribution, air entry pressure, etc.. Two of the most commonly used models should be introduced here with special attention to their application of hysteretic problems.

2.2.6.1 The Brooks and Corey Model

According to Brooks and Corey (1964), saturation of a wetting fluid in porous media on a drainage cycle typically decreases with capillary pressure as indicated by the relationship:

$$S_e \equiv \frac{\theta_w - \theta_{w,r}}{\theta_{w,s} - \theta_{w,r}} = \left(\frac{p_e}{p_c}\right)^{\lambda} \quad \text{for} \quad p_c \geq p_e \tag{2.12}$$

where
S_e effective water saturation
θ_w volumetric water content
$\theta_{w,s}$ maximum water content
$\theta_{w,r}$ residual water content
λ pore size distribution index
p_c capillary pressure
p_e air entry pressure

or conversely:

$$p_c = p_e \cdot S_e^{-\frac{1}{\lambda}} \quad \text{for} \quad p_c \geq p_e, \quad \theta_w \geq \theta_{w,r} \tag{2.13}$$

The parameter λ is related to the pore size distribution of the sample. Brooks and Corey found that for a typical porous medium, λ is about 2. Soils with well-developed structure have values of λ less than two and sands normally have values

of λ greater than 2, sometimes larger than 5. A large λ means narrow pore size distribution; small λ is an indicator for a very heterogeneous pore structure.

The physical meaning of the parameters $S_{w,r}$, and p_e is normally overrated. For a homogeneous isotropic porous material, the "residual water content" is defined as the water content which provides the best fit to a straight line for water contents greater than the critical air entry pressure p_e, in a $lnS_{w,e}$ vs. lnp_c plot. Actually, they should be seen as fitting parameters. Corey and Brooks (1999) explained the appropriate applications and limitations of their model as they found it to often be misused.

2.2.6.2 The van Genuchten Model

The van Genuchten (1980) model describes the pressure saturation relation in terms of the matric head

$$h = -\frac{2\sigma_{wa}}{\rho_w g r} \tag{2.14}$$

which is the relation between capillary radius r and the rise h of the water, as:

$$S_e \equiv \frac{\theta_w - \theta_{w,r}}{\theta_{w,s} - \theta_{w,r}} = (1 + (\alpha h)^n)^{-m} \tag{2.15}$$

where

S_e	effective water saturation
θ_w	actual water content
$\theta_{w,s}$	maximum water content
$\theta_{w,r}$	residual water content
h	matric head: $h = -\frac{\psi_m}{\rho_w g}$
n, α, m	fitting parameters

For a closed form of descriptions of hydraulic functions (see Section 2.4.1) it was convenient to couple the parameters m and n by the condition[3]

$$m = 1 - 1/n$$

which leads to

$$S_w(h) = [1 + [\alpha h]^n]^{-1+1/n} \tag{2.16}$$

or inverted:

$$p_c(S_w) = \frac{1}{\alpha}\left(S_w^{-n/[n-1]} - 1\right)^{\frac{1}{n}} \quad \text{for} \quad p_c > 0 \tag{2.17}$$

[3]This approximation has no physical significance and was only done for mathematical convenience since integration of the hydraulic conductivity function became less complicated.

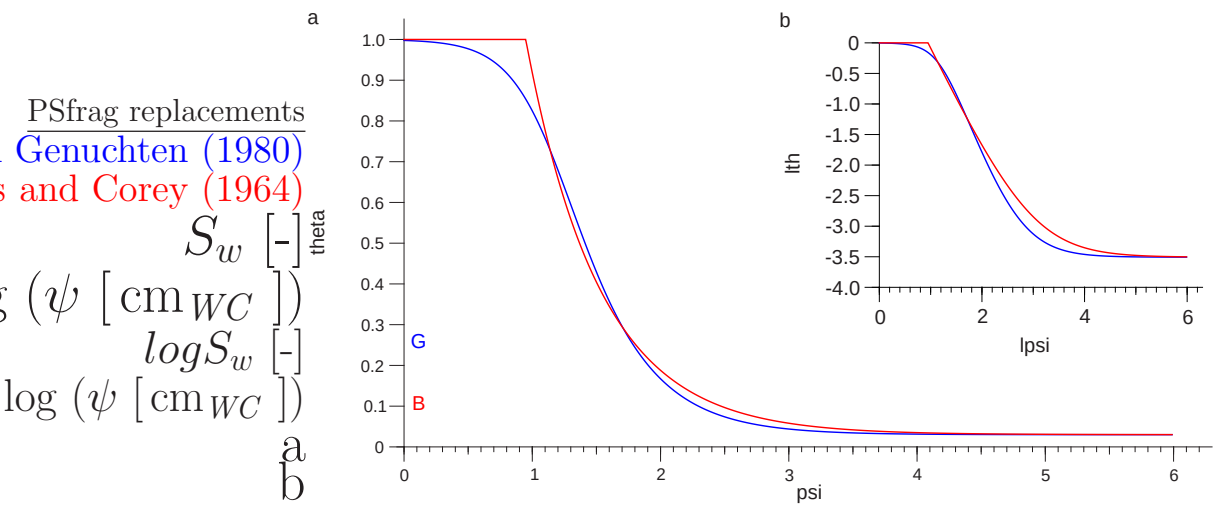

Figure 2.11: Comparison of the two parameterizations of the retention function. The Brooks and Corey relation (red) has a well defined air entry pressure whereas the van Genuchten relation (blue) has a smooth decrease of saturation with increasing potential. (b) is a log-log plot of (a).

where n has to be larger than 1.

In contrast to the Brooks and Corey model, all capillary pressures greater than zero are taken into account even if they are less than p_e. The parameter α corresponds to the displacement pressure while the pore geometry is represented by parameters n and m, which describe the slope of the curve. For the closed formulation, the parameter m is derived from n.

A correspondence between the Brooks and Corey and the van Genuchten models was deduced by Lenhard et al. (1989) (Figure 2.11). They compared the two parameterizations by using the differential fluid saturation capacities, $\partial S_e/\partial p_c$ for $p_c > p_d$ or $p_c > 0$, respectively:

$$\frac{\partial S_e}{\partial p_c} = \frac{\lambda}{p_d} \cdot S_e^{\frac{\lambda+1}{\lambda}} \tag{2.18}$$

and

$$\frac{\partial S_e}{\partial p_c} = \alpha \cdot m \cdot n \cdot \left(S_e^{-1/m} - 1\right) \cdot S_e^{1/m+1} \tag{2.19}$$

The two variables p_d and α are eliminated by insertion of equations (2.13) and (2.17) in (2.18) and (2.19) respectively, which results in:

$$\frac{\partial S_e}{\partial p_c} = \frac{\lambda S_e}{p_c}, \tag{2.20}$$

$$\frac{\partial S_e}{\partial p_c} = \frac{m}{(1-m)p_c} \cdot \left(S_e^{-1/m} - 1\right) \cdot S_e^{1/m+1} \tag{2.21}$$

Both models correspond to each other for $S_e = 0.5$, which results in:

$$\lambda = \frac{m}{1-m}\left(1 - 0.5^{\,1/m}\right) \tag{2.22}$$

Correspondence of entry pressure p_e and α is achieved by:

$$p_e = \frac{S_{\text{emp}}^{1/\lambda}}{\alpha}\left(S_{\text{emp}}^{-1/m} - 1\right)^{1-m} \tag{2.23}$$

with the empirical approach for the saturation of maximum correspondence:

$$S_{\text{emp}} = 0.72 - 0.35e^{-n^4} \tag{2.24}$$

Comparison of the two parameterizations in Figure 2.11, shows the conceptual differences of the models. The Brook and Corey relationship could be deduced if one assumes that the geometry of the pore space occupied by the wetting fluid is fractal, i.e. differing only in scale, at all water contents greater than $\theta_{w,r}$ (Miller and Miller 1956). Additionally the models assume a distinct air entry pressure. This becomes clear in a log-log plot as show in Figure 2.11 (b) where the retention function is represented by a straight line over a specific range beginning at the entry value. Although this model was based on physical assumptions, it had disadvantages in numerical simulations because the discontinuity caused by the entry pressure led to difficulties in the simulation process because of the non-steady derivative at the entry pressure; additionally the function is costly to evaluate. The van Genuchten model deduced the smooth function with the assumption that the pore size distribution started with pores of infinite radius. The idea behind that was the slow development of the capillary fringe, where water, drained from the large openings of the pores resulted in an outflow before the "air entry" pressure had been reached. Although the Brooks and Corey model was better related to physical principles, the van Genuchten model has been established because of its better numerical applicability. The derivative $d\theta/dh$ of this function is continuous and becomes asymptotically zero toward the fine and large pores. A lot of research was done based on the van Genuchten parameterization and almost all refinements in the theoretical field, like non-wetting phase models, hysteresis, etc., were tested with this model.

2.2.6.3 Pressure-Saturation Hysteresis Models

Since the water retention characteristic is of fundamental importance for the soil water behavior, the effect of hysteresis was examined by several authors with different concepts. Adequate parameterizations for the hysteretic pressure-saturation relation shown in Figure 2.10 were subject to different approaches with the aim of

predicting any scanning curve with the knowledge of the main curves. The conceptual models for hysteresis are based on the dependent domain theory which was developed in the 1940's and refined by Parlange (1976) and Mualem (1974). The empirical models were invented by Scott et al. (1983) and further developed by Kool and Parker (1987) and Parker and Lenhard (1987).

Dependent Domain Theory

The dependent domain theory is based on the assumption that the porous medium consists of pores with variable pore size. Behavior of every pore during drainage or imbibition depends on the state of the surrounding pores, i.e. a pore can only be drained if air is available from a neighboring pore. The basic concept of this model and its implications for the different behavior of the pore domains during drainage and imbibition are shown in Figure 2.12. The model distinguishes between two parameters that characterize the system: r_1, the radii of the openings of the pores in a group, and r_2 the radii of the pores within the group. If the capillary head changes from $h(r)$ to $h(r+dr)$ during imbibition all pores having radii $r \leq r_2 \leq r+dr$ are filled. In the drainage branch of the cycle, the head $h(r)$ is reduced to $h(r-dr)$ and the pores in the groups with radii r_1 in the range $r \leq r_1 \leq 1$ having radii $r \leq r_2 \leq r-dr$ are drained.

For predictions of scanning curves Mualem (1984) developed a scaling approach which is calibrated by use of both the main drainage and the main imbibition curve. The influence of the surrounding pores is accounted for by the macroscopic dependent domain factor. This factor describes the relative portion of drainable pores in the actual branch dependent of the saturations at the point where the wetting direction had changed. For predictions of the scanning cycles, the complete history of the system is necessary in calculating saturations (see Figure 2.12, right). Prediction of

rag replacements

a
b
c
0
1
r_1
r_2
drainage
wetting

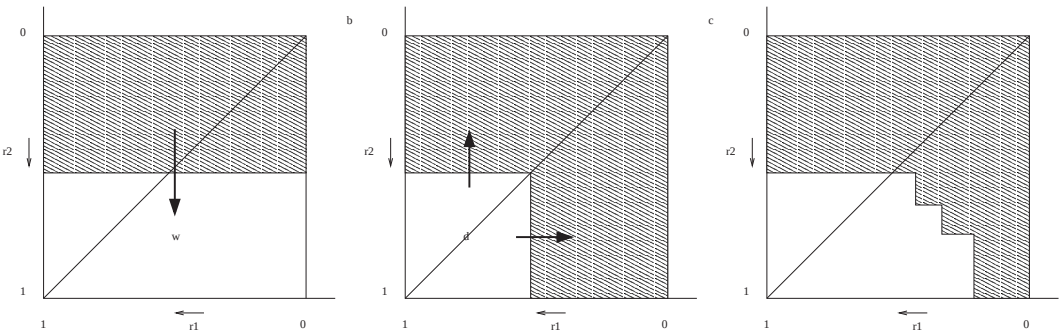

Figure 2.12: Conceptual model of the dependent domain theory for the hysteretic pressure saturation relation. Contour map of the filled pores for (a) the primary wetting and (b) primary drainage branch, (c) wetting after six processes of imbibition and drainage (Mualem 1974).

the imbibition curve is given by:

$$\theta^i(h) = \theta_\Delta + P(\theta_\Delta)\left[\theta_{w,s} - \theta^w(h_\Delta)\right]\left[\theta^w(h) - \theta^w(h_\Delta)\right] \tag{2.25}$$

and for the drainage curve:

$$\theta^d(h) = \theta_\Delta - P(\theta)\left[\theta_{w,s} - \theta^w(h)\right]\left[\theta^w(h_\Delta) - \theta^w(h)\right] \tag{2.26}$$

where the subscript delta indicates a reversal point, and superscript w denotes the main imbibition curve. The domain dependent function $P(\theta)$ is given by:

$$P(\theta) = \frac{\theta_{w,s} - \theta}{\left[\theta_{w,s} - \theta^w(h^+)\right]^2} \tag{2.27}$$

where h^+ is the pressure head at which

$$\theta^d(h^+) = \theta$$

with (2.17) this gives

$$h^+ = \frac{1}{\alpha}\left[(S^d_{w,e})^{-1/m} - 1\right]^{1/n}$$

For the imbibition process, P is a function of the known water content at the reversal point, while for the drainage branch, P is a function of the unknown water content θ and therefore the curve must be obtained iteratively.

Kool and Parker Model

The second type of hysteresis models are based on an empirical description of the connection between main and scanning curves. With the simple model of Scott et al. (1983) the drainage scanning curves are predicted by rescaling the main drainage curve to pass through the residual water content ($\theta_{w,r}$) and the last reversal point from wetting to drying ($S^d_{w,e}(h_\Delta)$), by replacing the saturated water content ($\theta_{w,s}$) by:

$$\theta^*_{w,s} = \frac{\theta_\Delta - \theta_{w,r}[1 - S^d_{w,e}(h_\Delta)]}{S^d_{w,e}(h_\Delta)} \tag{2.28}$$

The imbibition scanning curves are predicted by forcing the curve through the last reversal point form drying to wetting ($S^w_{w,e}(h_\Delta)$) and the saturated water content $\theta_{w,s}$ by the replacement of residual water content:

$$\theta^*_{w,r} = \frac{\theta_\Delta - \theta_{w,s}S^i_{w,e}(h_\Delta)}{1 - S^i_{w,e}(h_\Delta)} \tag{2.29}$$

where $S^d_{w,e}(h_\Delta)$ effective saturation on the main drainage curve at the reversal point pressure head
$S^i_{w,e}(h_\Delta)$ effective saturation on the main imbibition curve at the reversal point pressure head
θ_Δ water content at the reversal point
$\theta_{w,s}$ saturated water content
$\theta_{w,r}$ residual water content
h_Δ matric head at the reversal point

Since this model did not reflect air entrapment during imbibition the scanning cycles are not closed. Kool and Parker (1987) combined this approach with an empirical relation for air phase entrapment where the saturation of a scanning curve is derived by

$$\theta_u = \theta^d_{w,s} - \frac{\theta^d_{w,s} - \theta_\Delta}{1 + R(\theta^d_{w,s} - \theta_\Delta)} \tag{2.30}$$

where

$$R = \frac{1}{\theta^d_{w,s} - \theta^w_{w,s}} - \frac{1}{\theta^d_{w,s} - \theta^d_{w,r}} \tag{2.31}$$

where $\theta^d_{w,s} \geq \theta_u \geq \theta^w_{w,s}$. This empirical equation provides a useful approximation for air entrapment and has the advantage that no additional parameters are introduced. Furthermore, the model was expressed with the van Genuchten parameterization. The whole hysteresis loop could be described by the parameter vector $(\theta_{w,s}, \theta_{w,r}, \alpha^d, n^d)$ for the main drainage curve (MDC) and $(\theta_{w,s}, \theta_r, \alpha^i, n^i)$ for the main imbibition curve (MIC) with the simplification: $\theta^d_{w,r} = \theta^i_{w,r} = \theta_r$ and $\theta^d_{w,s} = \theta^i_{w,s} = \theta_{w,s}$. With the scaling of $\theta_{w,s}$ and $\theta_{w,r}$ the drying scanning curves were obtained by using the parameter vector $(\theta^*_{w,s}, \theta_{w,r}, \alpha^d, n^d)$ and the imbibition scanning curves were obtained by using the parameter vector $(\theta_{w,s}, \theta^*_{w,r}, \alpha^i, n^i)$. With this model, the parameters for drainage and imbibition could be estimated independently.

Kool and Parker (1987) compared their model with the dependent domain model. Simulations of hysteretic retention curves for 8 soils were carried out with both models. The results showed no unacceptable loss in accuracy as long as the soils did not have a narrow pore size distribution. The major advantages of this model are the small number of parameters and the low computational costs for simulations.

2.3 Fluid Flux

Forces on the fluids e.g. due to a pressure gradient cause a motion through the solid matrix if the fluid phase is continuous along the field. Fluid flow can be described at the pore scale by the Navier-Stokes equation and by Darcy's law at the continuum scale. For a saturated medium the only resistivity to the fluid flow is offered by the solid matrix. The so-called saturated conductivity is influenced by the pore geometry and the fluid mobility. Conductivity of an unsaturated porous medium is additionally influenced by the presence of other fluids as they share the same pore space.

Conductivity at the Pore Scale
Figure 2.1 (center) shows the distribution of the phases in a partially saturated porous medium. The presence of two fluids, reduces the available flow paths for each fluid, which influences their transport properties. If air saturation is increased, water is gradually drawn back to smaller pores which is concomitant with increasing tortuosity of the flow paths.

2.3.1 Conductivity at the Continuum Scale

The dependency between a driving pressure gradient and the volumetric water flux in a saturated porous medium was first observed by Darcy (1856) who deduced the empirical relation:

$$\mathbf{j_w} = -\mathsf{K}_{w,sat}\,\nabla p \tag{2.32}$$

with
$\mathbf{j_w}$	volumetric water flux
$\mathsf{K}_{w,sat}$	saturated conductivity [4]
∇p	pressure gradient

For the one-dimensional vertical case it can be simplified to:

$$j_{w,z} = -K_{sat,z}\frac{\partial p}{\partial z}$$

The saturated conductivity is dependant on the fluid and the solid material properties. There is also a fluid independent property, called permeability or intrinsic permeability which is related only to the influence of the porous matrix.

[4] In some textbooks K is called conductivity and k_i permeability. In other nomenclature K is permeability and k_i the intrinsic permeability.

The unique relationship between permeability k_i and saturated hydraulic conductivity $K_{w,sat}$, is described by:

$$K_{w,sat} = k_i \frac{\rho_w \, g}{\eta_w} \tag{2.33}$$

where the subscripts of w are properties related to water and $K_{w,sat}$ has the dimensions of $[\mathrm{ML^{-1}T^{-2}}]$. Using the fluid properties ρ_l and η_l of a different liquid l the conductivity of the fluid can be calculated by this relation[5].

Permeability k_i $[\mathrm{L^2}]$ of the soil can be calculated via Darcy's law from measurement of saturated water flow according to:

$$k_i = -\frac{j_{w,z} \, \rho_w \, g}{\eta_w \, \frac{\partial p}{\partial z}} \tag{2.34}$$

where k_i intrinsic permeability
j_w water flux [6]
ρ_w density of water
g gravitational acceleration
η_w dynamic viscosity of water
$\frac{\partial p}{\partial z}$ pressure gradient [6]

For unsaturated conditions the pore space availability of the water phase changes as its saturation is changed. A simple approach was the extension of Darcy's law by Buckingham (1907):

$$j_w = -K(\theta)\frac{\partial p}{\partial z} \tag{2.35}$$

where the measured unsaturated conductivity $K(\theta)$ includes all influences that have an effect on water flux.

2.3.2 Experimental Methods of Determining Unsaturated Conductivity

The measurement of unsaturated conductivity over a wide range of saturations is essential for the characterization of a porous medium. Solute transport, as well as the extraction of water or oil crucially depend on this property. In laboratory sized samples, the measurement can be done in several ways. Most of the methods use water as an active fluid. Of the large variety of methods available two different

[5] Since gaseous phases do not act as true fluids in porous media special gas flow effects has to be taken into account. See Section 2.3.4

[6] j_w and $\frac{\partial p}{\partial z}$ can be determined by measurement of the falling head (Section 3.3)

approaches will be explained here because they are based on different principles. These can be distinguished into two separate categories, the steady state methods and the transient methods.

Steady State Methods

The steady state methods are based on the evaluation of Darcy's law (equation 2.32). Stationarity in this context means that the volumetric water flux or the applied pressure gradient is kept constant during the experiment. For the measurement of every single point of the K(θ)- or K(ψ)-relation, the specific state of the system (θ, ψ) has to be adjusted and a steady state has to be reached.

For the constant head method, the sample is connected to predefined tensions at two opposite ends by porous plates. Tensiometers placed at different heights in the sample are observing the pressure gradient. At one end water is applied with a constant pressure. If a steady state is reached, the constant flux at the other end is measured and hydraulic conductivity can be evaluated by equation 2.35. For evaluation, the conductivity of the porous plates has to be considered (Klute and Dirksen 1986).

The constant flux method works in such a way that the flux is controlled instead of the pressure head. At one end of the sample, a constant flux is applied by infiltration or evaporation. Tensiometers in the sample observe the evolution of a unit gradient. As a steady state is reached, unsaturated hydraulic conductivity can be evaluated.

Transient Methods

Transient methods are based on the evaluation of temporal evolution of the flux process in the examined sample. Observation of the hydraulic heads is made by several tensiometers and the water content is monitored by time domain reflectrometry (TDR), gamma attenuation, or if an invasive method is chosen by gravimetric measurements.

For the instantaneous profile method, the sample has to be instrumented with the observation tools (tensiometers, TDR, ...) and the initial state has to be determined precisely. The sample is drained from one end and the temporal evolution of tensions and saturation is monitored. Evaluation of the data is done by balancing the temporal evolution of the water content in the sample.

The most promising tools for transient determination of unsaturated hydraulic conductivity are the stimulated out-/in-flow methods. For the most simple case, the flux at one end of the sample is negligible and at the other end a pressure gradient is applied to the water phase. The pressure can be changed in a single reduction (one-step experiment) or in several steps (multistep outflow experiment). The major disadvantage of these methods is the small pressure range of the measurement. Especially for the dry range, additional measurements have to be made, e.g. by evaporation experiments. The multistep outflow method has been used for this study and will be explained in detail in Section 3.1.

2.3.3 Parameterization of Unsaturated Conductivity

Since it is not always easy to perform the necessary experiments to measure unsaturated conductivity it is often more convenient to calculate the $K(\theta)$ relationship from other properties of the medium which are easier to measure. The calculations can also be used to check the experimental results (Brutsaert 1967). The saturation – conductivity relation, $K(\theta)$, has been parameterized by several approaches. An overview on the geometric effects which have an influence on the unsaturated conductivity is given in Figure 2.13. The models developed on this basis can be sorted into two categories, the purely empirical models, and the geometry based models.

2.3.3.1 Purely Empirical Conductivity Models

For the simpler models, the pore space is characterized by a bundle of homogeneous parallel capillaries, each with the same radius. There are two different views of this model configuration. One idea is that the tubes are drained in their centers and water is only at the capillaries walls. The model which describes this problem was analyzed by Averjanov (1950). This model was based on the similarity of Darcy's law and the Hagen-Poiseuille equation:

$$\text{Darcy:} \quad \mathbf{j_w} = -\frac{k_i}{\eta_w}\nabla p \quad ; \quad \text{Hagen-Poisseuille:} \quad \mathbf{j_w} = -\frac{r^2}{8\eta_w}\nabla p \tag{2.36}$$

A comparison of the two equation gives the conductivity of a single tube with radius r which can be extended for a bundle of capillaries:

$$\text{single tube:} \quad k_i = \frac{r^2}{8} \quad ; \quad \text{bundle of capillaries:} \quad k_i = \frac{\phi \cdot \overline{r}^2}{8},$$

where ϕ is the porosity and $\overline{r}$ is the mean radius of the capillaries in the bundle. For an annular flow of the water in the single tube the conductivity was approximated by a power type relationship:

$$k_w(S_{w,e}) = k_i \, S_{w,e}^n \tag{2.37}$$

where the saturation of the annular water at the boundary is given with respect to the air-filled core of the tube (radius r_a)

$$S_{w,e} = 1 - \left(\frac{r_a}{r}\right)^2$$

The other view assumes an effective hydraulic radius of the pores in a granular medium, where pore cross-sections of any geometry can be included. This model

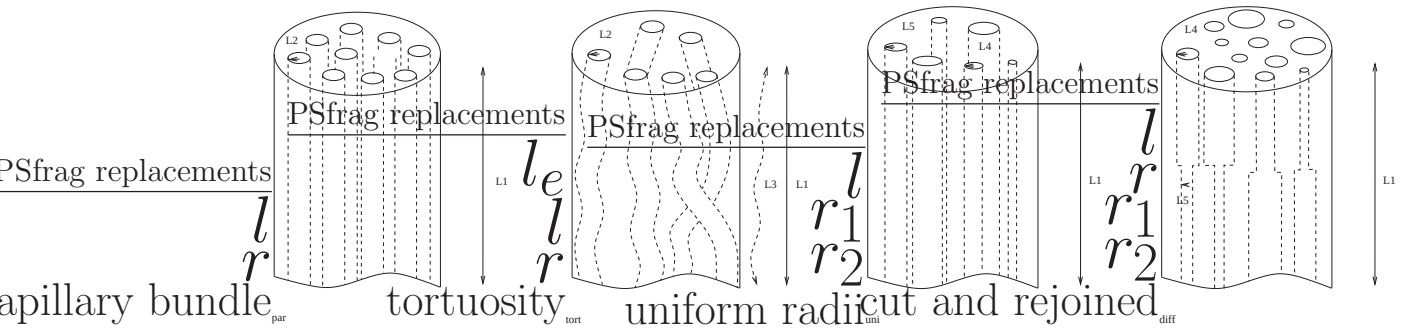

Figure 2.13: Geometric effects influencing permeability

was developed by Kozeny (1927) who introduced the tortuosity parameter τ because the irregularities of the pores had to be accounted for in the model. The tortuosity parameter τ was used as a measure of the geometric shape information. Actually tortuosity represents the influence of the winding of the fluid-filled pores through the matrix and accounts for the change in the topology of the fluid phase as saturation changes. In drainage processes where the water phase is drawn back to the smaller pores, tortuosity increases since the high connectivity of these pores result in longer microscopic path lengths (see Figure 2.1, center, and Figure 2.13). The resulting conductivity function is of the power law type such as equation 2.37 with additional form factors. The value of the exponent n, depends on the effects included in the model. For the capillary tube model of Averjanov, with the assumption of a stagnant air phase was $n = 3.5$, whereas the extension of the Kozeny model produced $n = 3$ for an air phase which moves under the same pressure gradient as water (Brutsaert 2000).

For the two phases air and water tortuosity depends on the actual saturation of the porous medium. At the same value of S_w, tortuosity is typically larger in the soil water than in the soil air phase and the difference becomes more pronounced with increasing surface area and at a low S_w. The water phase transport parameters show a steeper decrease with S_w compared with the air phase parameters, because the water phase is influenced more by tortuosity than the gaseous phase (Moldrup et al. 2001).

Pneumatic conductivity is typically described with an effective non-wetting phase saturation which is complementary to the wetting phase. Examples of these simple polynomial functions are given in Table 2.2. The models do not account for the existence of a discontinuous air phase, either trapped or locally accessible. To describe the dependency on saturation the conductivity of a fluid $k_\alpha(S_\alpha)$ (α: water, air,...) is usually written as the product of the conductivity at a matching point (normally the saturated conductivity $k_{sat,\alpha}$ is used as reference point) and the relative conductivity $k_{r,\alpha}(S_\alpha)$.

Model	$S_{w,e} = (\theta_w - \theta_{w,r})/(\theta_{w,s} - \theta_{w,r})$
Corey[1]	$k_{r,a} = (1 - S_{w,e})^2(1 - S_{w,e}^2)$
Pirson[2]: Imbibition	$k_{r,a} = (1 - S_{w,e})^2$
Pirson: Drainage	$k_{r,a} = (1 - S_{w,e})(1 - S_{w,e}^{1/4} S_w^{1/2})^{1/2}$
Wyllie[3]	$k_{r,a} = (1 - S_{w,e})^3$

Table 2.2: Selected empirical models for relative non-wetting phase conductivity in terms of effective wetting phase saturation (saturations are defined in Figure 2.14). In deriving the effective non-wetting phase expressions, the relationship $S_{a,e} = S_a/S_{a,s} = 1 - S_{w,e}$ was used. Ref.: [1] Corey (1954), [2] Pirson (1958), [3] Wyllie (1962)

The empirical models were developed for the prediction of oil conductivity in water-wet granular rocks. The model of Wyllie (1962) represents the simple power models with an exponent of $n = 3$ which corresponds to the hydraulic Kozeny model. The Corey (1954) model has an additional term reflecting pore connectivity and tortuosity. The model was widely used by petroleum engineers (Honarpour et al. 1986). The model of Pirson (1958) reflects hysteresis and offers a separate description of drainage and imbibition branches of the conductivity-saturation relationship.

2.3.3.2 Geometry Based Conductivity Models

The next step of refinement is to distinguish between portions of pores with different diameters, each with a different conductivity. The pore system is assumed to be equivalent to a bundle of uniform capillary tubes of many different sizes. The distribution of pore sizes is derived from the soil water characteristic $S(h)$, where the matric head h can be related to the effective pore radius r by equation 2.14. The most common parameterizations of hydraulic conductivity functions of this type are the models of Burdine (1953) and Mualem (1976) which are based on network models for pores with different features. The refinement of the model increases the applicability to measured data since influences of pore geometry are better reflected.

For evaluation of non-wetting phase conductivity, several methods have been developed for the different purposes in soil science, like soil aeration, soil remediation by air sparging, extraction of volatile organics, or exploitation of natural gas in the petroleum branch of research. The conceptual framework of the water-air system and its main features are shown in Figure 2.14; the upper part shows the retention curve and the lower part shows the corresponding relative conductivity functions for the wetting and the non-wetting phases. The figure refers to a single branch of the curve which is typically hysteretic (see Section 2.2.4).

The lower part of Figure 2.14 shows the possible mobility domains of the two

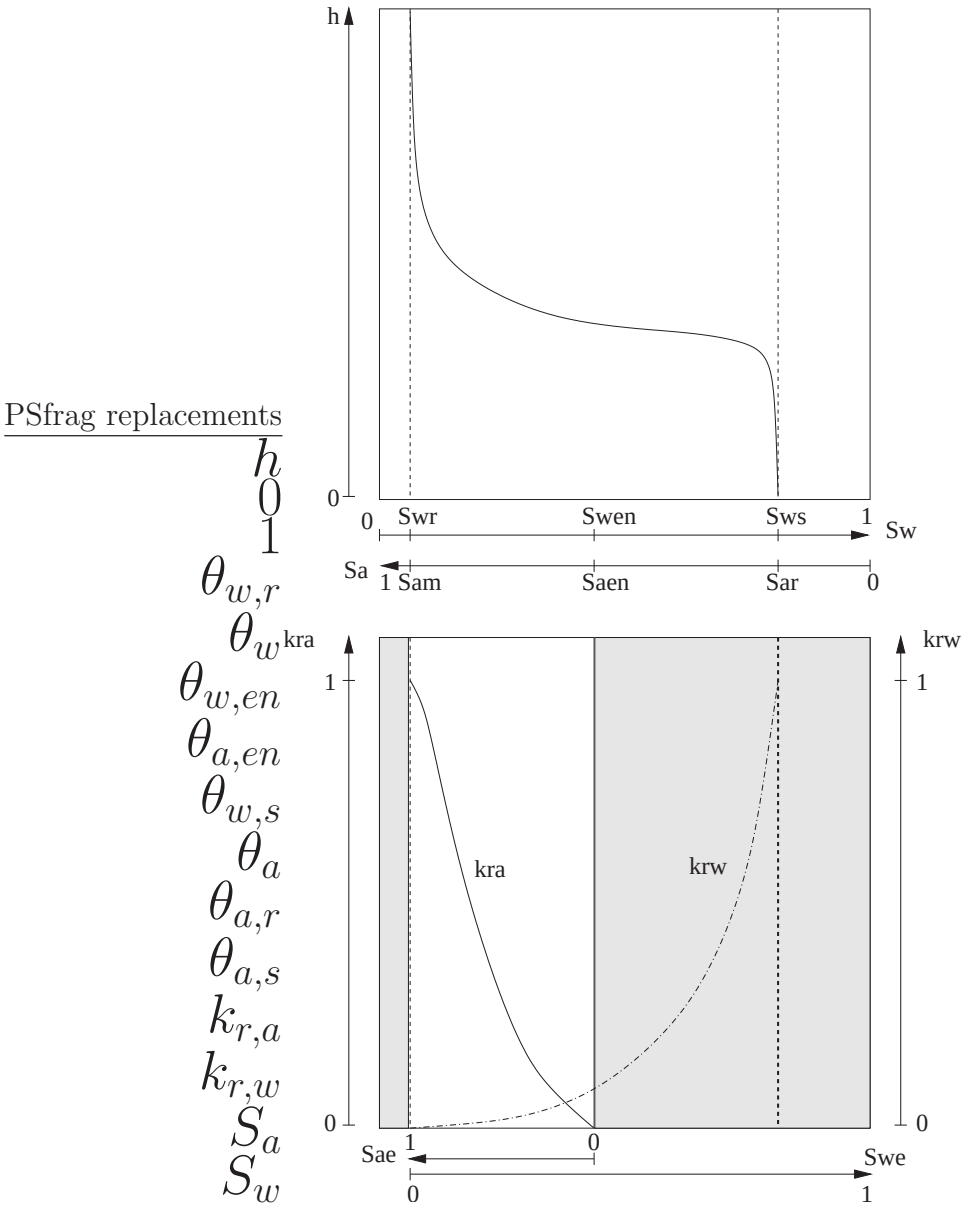

Figure 2.14: Schematic representation of retention curve (top) and relative conductivity functions (bottom) for the wetting (dashed) and the non-wetting (solid line) phases during drainage. In the bottom part the shaded areas indicate saturations at which one of the phases is discontinuous (Dury et al. 1999).

immiscible fluids. The lower limit of volumetric phase content achieved by drainage defines the residual content of this phase (drainage of non-wetting phase is better known as imbibition of wetting phase). The residual contents $\theta_{w,r}$ and $\theta_{a,r}$ are accounting for the part of the fluid which has lost connection to the phase reservoir and therefore is incoherently distributed in the sample. If only Darcian flow is considered, the residual phase content must not be defined rigorously in terms of thermodynamic equilibria since it represents only an operational concept[7] (Luckner et al. 1989). For purposes of consistent notation, full or maximum phase content of one phase is defined complementary to the residual phase content of the other phase as:

$$\theta_{w,s} = 1 - \theta_{a,r} \quad \text{and} \quad \theta_{a,s} = 1 - \theta_{w,r} \tag{2.38}$$

The Burdine Model

The model assumes a bundle of parallel capillaries with varying pore radii perpendicular to the direction of flow and a uniform pore size in the direction of flow. The mean hydraulic radius $\overline{R}_w$ of the wetting phase, is evaluated by integrating the volumetric water content θ_w from 0 to actual saturation by involving all pores beginning with the small ones. Combining Laplace equation (2.7) with the hydraulic radius yields for the wetting fluid:

$$\overline{R}_w^2 = \frac{\sigma_{wa}^2 \cos^2 \gamma}{\theta_w} \int_0^{\theta_w} \frac{d\theta_w}{p_c^2} \tag{2.39}$$

For the non-wetting fluid the integration goes from actual saturation to 1 as air occupies the complementary larger pores:

$$\overline{R}_a^2 = \frac{\sigma_{wa}^2 \cos^2 \gamma}{\theta_{w,s} - \theta_w} \int_{\theta_w}^1 \frac{d\theta_w}{p_c^2} \tag{2.40}$$

Surface tension σ_{wa} and contact angle γ are assumed to be constant.

With the concept of mean radii, conductivity for the wetting phase becomes:

$$k_w(\theta_w) = \frac{\theta_w \overline{R}_w^2}{\tau} \tag{2.41}$$

and for the non-wetting phase:

$$k_a(\theta_{w,s} - \theta_w) = \frac{(\theta_{w,s} - \theta_w)\overline{R}_n^2}{\tau} \tag{2.42}$$

[7] Incoherence only means that the fluid is immobile as a linked phase. Because of trans-phase exchange (e.g. evaporation, condensation, or degassing) and transport as a dissolved phase in the other fluid phase, the incoherently distributed phase in the subsurface can still undergo significant changes.

where k_w and k_a are the conductivities of the wetting and the non-wetting phase at water content θ_w, respectively.

Inserting 2.39 in 2.41 and 2.40 in 2.42 yields in:

$$k_w = \sigma_{wa}^2 \cos^2 \gamma \int_0^{\theta_w} \frac{1}{\tau} \frac{d\theta_w}{p_c^2} \tag{2.43}$$

and for the non-wetting phase:

$$k_a = \sigma_{wa}^2 \cos^2 \gamma \int_{\theta_w}^{1} \frac{1}{\tau} \frac{d\theta_w}{p_c^2} \tag{2.44}$$

The relative hydraulic conductivity is:

$$k_{r,w} = \frac{k_w}{k_0} = \frac{\int_0^{\theta_w} \frac{1}{\tau} \frac{d\theta_w}{p_c^2}}{\int_0^1 \frac{1}{\tau} \frac{d\theta_w}{p_c^2}} \tag{2.45}$$

and relative pneumatic conductivity is:

$$k_{r,a} = \frac{k_a}{k_0} = \frac{\int_{\theta_w}^1 \frac{1}{\tau} \frac{d\theta_w}{p_c^2}}{\int_0^1 \frac{1}{\tau} \frac{d\theta_w}{p_c^2}} \tag{2.46}$$

Tortuosity is still in the integral as it strongly depends on the saturation. Burdine (1953) found an experimental evidence for a linear dependency between τ and θ_w because water follows the more tortuous paths as water content decreases:

$$\tau^2(S_{w,e}) = \tau_s^2 S_{w,e}^{-2} \tag{2.47}$$

which led to:

$$k_{r,w}(\theta_w) = \left[\frac{\theta_w - \theta_{w,r}}{\theta_{w,s} - \theta_{w,r}}\right]^2 \frac{\int_0^{\theta_w} \frac{d\theta_w}{p_c^2}}{\int_0^1 \frac{d\theta_w}{p_c^2}} \tag{2.48}$$

for the wetting phase and for the non-wetting phase

$$k_{r,a}(\theta_w) = \left[1 - \frac{\theta_w - \theta_{w,r}}{\theta_{w,s} - \theta_{w,r}}\right]^2 \frac{\int_{\theta_w}^1 \frac{d\theta_w}{p_c^2}}{\int_0^1 \frac{d\theta_w}{p_c^2}} \tag{2.49}$$

The Mualem Model

A more statistical approach is to represent the pore system by a bundle of capillaries with different but uniform radii, cut them normally to the flow direction and rejoin them again randomly. This model takes the random variations of pore sizes normal

to flow direction and along flow direction into account. The so called statistical pore space models were invented by Childs and Collis-George (1950).

Mualem and Dagan (1978) deduced a model from this approach where the effective radius of the whole system is calculated of a serial sequence of two bundles of parallel capillaries. The geometric mean radius is calculated by:

$$\overline{R}^2 = r_1 \cdot r_2 \tag{2.50}$$

integration over all possible combinations of the two pores yields:

$$\overline{R}^2 = \int_0^{S_{w,e}} \int_0^{S_{w,e}} \frac{d\theta_1}{p_{c,1}} \frac{d\theta_2}{p_{c,2}} \tag{2.51}$$

Since there is no correlation between the two domains, which was the assumption for the random rejoining, the integral can be rewritten as:

$$\overline{R}^2 = \left(\int_0^{S_{w,e}} \frac{d\theta}{p_c} \right)^2 \tag{2.52}$$

with the saturation dependent tortuosity

$$\tau^2(S_{w,e}) = \tau_s^2 S_{w,e}^{-0.5} \tag{2.53}$$

the model is in its general form for the wetting phase:

$$k_{r,w}(\theta_w) = \left[\frac{\theta_w - \theta_{w,r}}{\theta_{w,s} - \theta_{w,r}} \right]^{0.5} \left[\frac{\int_0^{\theta_w} p_c^{-[1+b]} d\theta_w}{\int_0^1 p_c^{-[1+b]} d\theta_w} \right]^2 \tag{2.54}$$

And for the non-wetting phase:

$$k_{r,a}(\theta_w) = \left[1 - \frac{\theta_w - \theta_{w,r}}{\theta_{w,s} - \theta_{w,r}} \right]^{0.5} \left[\frac{\int_{\theta_w}^1 p_c^{-[1+b]} d\theta_w}{\int_0^1 p_c^{-[1+b]} d\theta_w} \right]^2 \tag{2.55}$$

With this model, which is often used with $b = 0$, the $k_a - S_w$ relationship could be predicted with a known $p_c - S_w$ relation (Mualem 1976). With the examination of 45 samples, it has been found that the measured data is fitted best with the exponent 0.5, whereas it has also been proposed by several authors to keep the exponent as a free parameter for more flexibility in the fitting of measured data (e.g. Hoffmann-Riem et al. 1999).

Although the refinement of the models reached a better agreement between predicted and measured conductivities, they are based on assumptions which could not be held true for natural porous media. They are all based on the Young-Laplace equation, where all geometric influences of the pore space are folded into a single parameter. The variations of pore size in flow direction implemented in the Mualem model reflects the natural system better but the assumption of two bundles of capillaries which are connected in series is somewhat arbitrary.

2.3.4 Effects Influencing Air Conductivity

Gas flow in porous media differs from liquid flow because of gas compressibility and pressure dependent conductivity. There is no doubt that the former effect has little consequences on fluid displacements but it is not always possible to ignore this factor. Resistance to air flow can be significant during infiltration when compression of air occurs ahead of a wetting front under border irrigation (Dixon and Linden 1972). For drainage Corey and Brooks (1975) have found that receding water develops pressure surges that can be associated with air entry through restrictions within the soil pore space.

The intrinsic permeability of a porous medium is often measured by means of air or other gases. Klinkenberg (1941) showed that permeabilities measured by means of gases vary with pressure and therefore gas conductivities cannot directly be equated to liquid conductivities. Air passing the porous medium does not act as a true fluid continuum, which means that the fluid velocity is not zero at the solid boundaries like it is for other fluids. Because of this effect air conductivity is always larger than the theoretical values at maximum liquid content. This effect is known as the "gas slippage" or "Klinkenberg" effect (Klinkenberg 1941)[8]. The difference between the slip enhanced conductivity and calculations based on intrinsic permeability is between 20 and 30 percent (Corey 1986).

For fine-textured materials and high gas pressures air conductivity k_a has to be slip corrected by the Klinkenberg method (Klinkenberg 1941):

$$k_a^* = k_a(1 + b/\overline{p}) \tag{2.56}$$

where k_a^* is the slip enhanced conductivity determined at mean absolute pressure $\overline{p} = (p_1 + p_2)/2$, k_a is the theoretical conductivity in absence of the slip, and b is a parameter which depends on the geometry of the gas filled pore space. For simplified models b can be computed from geometric properties, for real soils b must be determined empirically. For variably saturated media, Fulton (1951) reported a more or less linear dependence of k_a^* on $1/\overline{p}$, where studies were made on consolidated media only.

The coherence of the air phase is reflected by the so-called analogy based models. These models account for discontinuity of the non-wetting phase at a high wetting phase saturation. The model of Lenhard and Parker (1987) partitions the non-wetting phase into the free and continuous phase $S_{a,c}$ and trapped or discontinuous phase $S_{a,d}$, i.e., $S_a = S_{a,c} + S_{a,d}$. Other models of this type were developed by Luckner et al. (1989) and Fischer et al. (1996). The latter will be described in detail in Section 2.4.

[8] When water is used to determine the intrinsic permeability it is smaller than the gas-slippage corrected air permeability because of the interaction between water and the soil solids, mainly in clay.

2.3.5 Hysteresis Effects in Conductivity Functions

Capillary-Pressure–Conductivity Hysteresis

The history dependence of the pressure-saturation relation (Figure 2.10), results in different water contents at a specific capillary pressure during drainage and imbibition, therefore hysteresis of the retention function affects also the pressure-conductivity relation. Hydraulic conductivity between two states of equal pressure is hysteretic due to the hysteresis in saturation.

Saturation–Conductivity Hysteresis

Hysteresis in the saturation conductivity relation is neglected by most models because the effect is small and models can then be expressed in closed forms (Nielsen et al. 1986, Kool and Parker 1987).

On the other hand, entrapment of the non-wetting fluid also causes hysteresis in the relative-conductivity–saturation relation. In the imbibition cycle, water fills the small pores first which may enclose air in the larger pores. Water has to flow around these entrapped bubbles and use the smaller pores with low conductivity. The little differences between drainage and imbibition data was pointed out by Topp and Miller (1966). Although the observed hysteresis was no more than two or three times the experimental uncertainty, they found a genuine and systematic effect. Similar effects were observed by Poulovassilis and Tzimas (1975). They were able to explain the

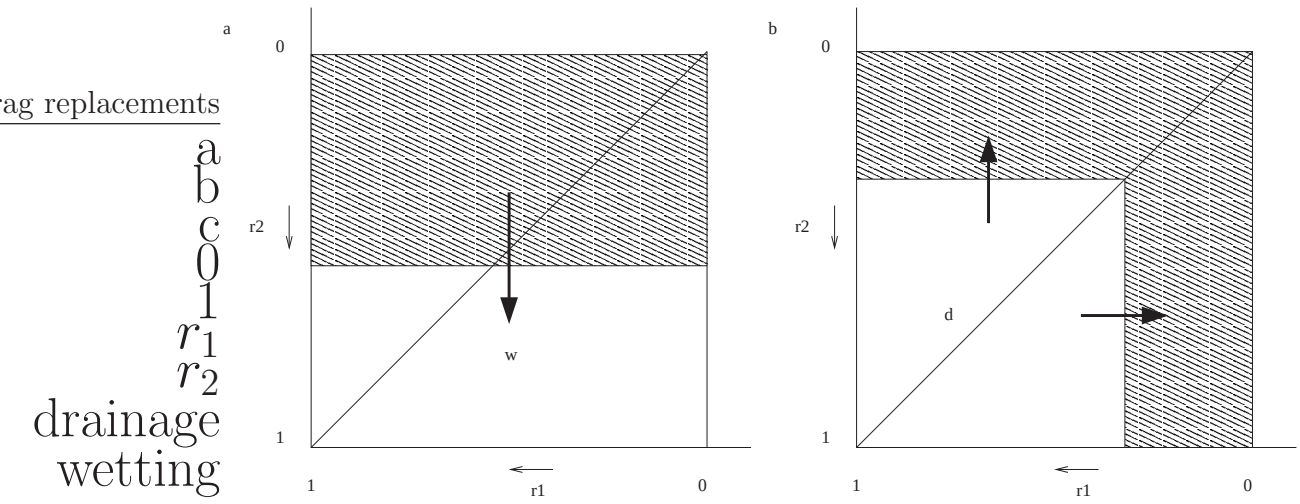

Figure 2.15: Contour map of the filled pores for the main wetting (a) and drainage (b) branch (Mualem 1974). (b) shows the drainage map for the saturation corresponding to (a). Hysteresis of conductivity saturation relation was explained by integration of the different domains for drainage and saturation.

hysteresis effect in their experimental results by the dependent domain theory. The two effective radii of the cut and rejoined capillary bundle (Section 2.3.3.2) have a distinct influence during the drainage-imbibition cycle. For a continuous water phase, all pores corresponding to the applied pressure are filled during the wetting process. During drainage, the pores with radii r_2 are drained if they are in groups with radii r_1, which correspond to the applied pressure. The integration of equation 2.52 was based on independent domains and the radii of both domains contributed the same part to saturation. For reflection of hysteresis the domains have to be integrated separately. The basic principles of this approach are sketched in Figure 2.15.

Lenhard and Parker (1987) have modified the Mualem model and implemented the concept of phase entrapment in the mobile fluid phases in their empirical model. The entrapped immobile air bubbles will result in an obstruction to water flow, while the presence of air bubbles will displace water into larger pores (to reach the same saturation) which will increase conductivity. Their modified $k_r - S_w$ relation is:

$$k_{r,w} = S_{w,e}^{0.5} \left[\frac{\int_0^{S_w^*} \frac{dS_{w,e}}{p_c(S_{w,e})} - \int_0^{S_{a,t}} \frac{dS_{a,t}}{p_c(S_{w,e})}}{\int_0^1 \frac{dS_{w,e}}{p_c(S_{w,e})}} \right]^2 \tag{2.57}$$

where S_w^* is the apparent and $S_{w,e}$ is the effective water phase saturation. $S_{a,t}$ is the entrapped non-wetting phase saturation which can be calculated with knowledge of the water saturation at the reversal point from main drainage branch ${}^{\Delta}S_w$ and the residual air saturation $S_{a,r}$. The linear interpolation method of Parker and Lenhard (1987) described $S_{a,t}$ depending on S_w as:

$$dS_{a,t} = \frac{S_{a,r}}{1 - {}^{\Delta} S_w} dS_{w,e} \tag{2.58}$$

which results in the hydraulic conductivity relation:

$$k_{r,w} = S_{w,e}^{0.5} \left[\frac{\int_0^{S_w^*} \frac{dS_{w,e}}{p_c(S_{w,e})} - \frac{S_{a,r}}{1-{}^{\Delta}S_w} \int_{S_{w,e}}^{S_w^*} \frac{dS_{w,e}}{p_c(S_{w,e})}}{\int_0^1 \frac{dS_{w,e}}{p_c(S_{w,e})}} \right]^2 \tag{2.59}$$

For air conductivity the effective free air saturation is:

$$S_{a,f} = S_a - S_{a,t}$$

then the pneumatic conductivity relation is:

$$k_{r,a} = S_{a,f}^{*0.5} \left[\frac{\int_{S_w^*}^1 \frac{dS_{w,e}}{p_c(S_{w,e})}}{\int_0^1 \frac{dS_{w,e}}{p_c(S_{w,e})}} \right]^2 \tag{2.60}$$

Several studies of air conductivity (and other gas conductivity) functions have considered a drying from complete saturation history followed by a subsequent wetting history (e.g. Honarpour et al. 1986). Most of these studies have obtained lower gas conductivities for wetting than for drying, given the same total saturation; the wetting curve often diverges steadily from the drying curve as the wetting-phase saturation increases. Such hysteretic effects were usually ascribed to gas entrapment (Stonestrom and Rubin 1989b). Previous studies performed by Naar et al. (1972) and Colonna et al. (1972) have seen the opposite effect. In glass bead experiments they found that gas-conductivity was higher for wetting than for drying at the same total gas saturation. For better analysis of conductivity data it is necessary to know the composition of the air volume in a measured sample, i.e., the portion of entrapped air, boundary domains, and continuous air-paths, respectively.

2.4 Parameterizations of Hydraulic and Pneumatic p-k-S–Relations

To obtain a full set of constitutive relations, which describe multiphase processes in unsaturated porous media the conductivity models 2.48 and 2.54 are combined with the pressure saturation relation introduced in Section 2.2. A model which describes the hydraulic properties of a porous medium is a combination of the Mualem approach for conductivity with the van Genuchten parameterization of the retention function. For parameterization of pneumatic properties the geometry based conductivity models of Mualem and Burdine are also used with the van Genuchten retention model. Additionally, the emergence point model includes effects of phase entrapment. Figure 2.16 shows the hydraulic functions (black) and a comparison of the three different parameterizations of pneumatic properties, the VGM, VGB, and the EP model which are explained in the following section.

2.4.1 The van Genuchten-Mualem Model — VGM

Van Genuchten combined the Mualem model (equation 2.54) with his retention model (equation 2.16) and developed a closed parameterization for conductivity (van Genuchten 1980). This is the most commonly used model for the evaluation of hydraulic properties in soil physics and also used in this study.

The parameterized model for the wetting phase is:

$$k_{r,w}(S_w) = S_w^{\tau}\left[1-(1-S_w^{n/[n-1]})^{1-1/n}\right]^2 \tag{2.61}$$

or in the head form:

$$\begin{aligned} k_{r,w}(h) &= [1+[\alpha h]^n]^{\tau[1-1/n]}\cdot \\ &\quad \cdot\left[1-[\alpha h]^{n-1}[1+[\alpha h]^n]^{-1+1/n}\right]^2 \end{aligned} \tag{2.62}$$

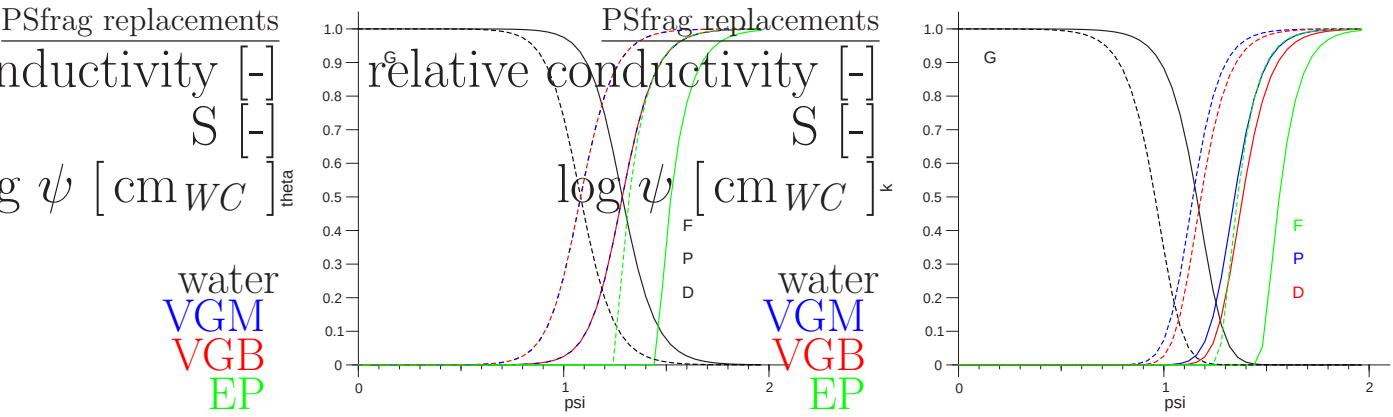

Figure 2.16: Hydraulic and pneumatic functions. Left: Pressure-saturation relation for water and air. The VGM and VGB models are based on the same pressure air saturation relation. For EP model effective continuous air saturation is considering the emergence point saturation. Right: Pressure-conductivity relations. Separate plots for drainage (solid lines) and imbibition (dashed lines).

Kool and Parker (1987) have applied their hysteresis approach (Section 2.2.6.3) to this model in two ways. In order to obtain the most accurate prediction of measured data they have determined a complete set of parameters for both branches of the cycle. The model is referred to as the *Kool and Parker* model. For practical use, it was assumed that the residual water content $\theta_{w,r}$ and the saturated water content $\theta_{w,s}$ have the same values for drainage and imbibition. Additional simplification was achieved by neglecting $k(\theta)$ hysteresis which meant that parameter n was the same for drainage and imbibition. The whole hysteresis loop was then described by the parameter vector $(K_s, \theta_{w,s}, \theta_r, \alpha^d, \alpha^i, n)$. Kool and Parker (1987) compared simulation results of this "constrained" model using six parameters to simulations with the whole set of nine parameters$(K_s, \theta^d_{w,s}, \theta^i_{w,s}, \theta^d_r, \theta^i_r, \alpha^d, \alpha^i, n^d, n^i)$. They concluded that for soils with a wider pore size distribution the reduced number of parameters would not lead to an unacceptable loss in accuracy. This model is referred to as the *constrained Kool and Parker* model.

2.4.2 The van Genuchten-Burdine Model — VGB

For the prediction of unsaturated air conductivity, the Burdine conductivity model can be combined with the van Genuchten retention model. Insertion of equation 2.16 in 2.49 yields an expression for the relative non-wetting conductivity which depends on effective water saturation $S_{w,e}$ and the van Genuchten parameter m

$$k_{r,a} = (1 - S_{w,e})^2 (1 - S_{w,e}^{1/m})^m$$

The second term represents the capillary model, while the first is an empirical factor introduced to account for connectivity and tortuosity of the pores.

The concept behind the geometry based air conductivity models implies that the non-wetting phase is continuous up to the maximum wetting phase saturation $\theta_{w,s}$. Non-wetting phase entrapment is considered to be zero, i.e. $\theta_{a,r} = 0$.

2.4.3 The Emergence-Point Model — EP

The shaded areas in Figure 2.14 show the saturations where the porous medium becomes impermeable to one of the phases because residual saturation is reached. The concept of emergence and extinction points has been established by Stonestrom and Rubin (1989a) and Fischer et al. (1997). The emergence point is the value of water saturation where gas flow becomes detectable during drying and the extinction point is the water saturation where the gas flow becomes unmeasurable during wetting. The range of saturation where both phases are continuous from adjacent ranges and in which the medium is impermeable to one phase is delimited by these points (Luckner et al. 1989). This range is a part of the water characteristic that can be seen as the effective saturation for the wetting phase

$$S_{w,e} = \frac{\theta_w - \theta_{w,ew}}{\theta_{w,s} - \theta_{w,ew}} \tag{2.63}$$

and for the non-wetting phase

$$S_{a,e} = \frac{\theta_a - \theta_{a,ea}}{\theta_{a,s} - \theta_{a,ea}} \tag{2.64}$$

where $\theta_{w,ew}$ and $\theta_{a,ea}$ are the respective phase contents at the emergence point of the wetting and the non-wetting phases, respectively. $\theta_{w,s}$ and $\theta_{a,s}$ are the maximum contents for the both phases. With respect to the wetting phase the difference between the residual phase content and the emergence point has usually been considered negligible and irrelevant (Brooks and Corey 1964, Corey 1986). In that case, $\theta_{w,ew}$, can be substituted by $\theta_{w,r}$ so that $S_{w,e}$ is given by

$$S_{w,e} = \frac{\theta_w - \theta_{w,r}}{\theta_{w,s} - \theta_{w,r}} \tag{2.65}$$

As indicated in Figure 2.14 this cannot be done in the same way with the non-wetting phase because of large discrepancies between the residual non-wetting phase content and the emergence point of the non-wetting phase conductivity (Dury et al. 1998). This effect can be explained by changes in air-filled porosity at saturations with no air continuity through the sample. The additional air volume increases the air domains which are in contact with only one of its boundaries (White et al. 1972).

This makes a differentiation of the air compartments necessary. Total air content is the sum of trapped air which is not accessible from the boundaries, locally accessible air with no contribution to conductivity and continuously distributed domains which are accessible for air flow measurement. To evaluate experimental air-flow data this sum of three air compartments has to be considered for the saturation conductivity relation. As one can imagine, the boundary effect becomes more important for large laboratory columns where the local accessible air can dominate the volumetric air content (Dury 1997). If the emergence point is reached, the air conductivity k_a is nonzero and increases with saturation of the air phase. Dependence on saturation $k_a(S_a)$ is the product of the conductivity $k_{mp} = k_n(S_{mp})$ at a reference or matching point S_{mp} and a relative conductivity $k_{rn}(S_a)$. The matching point is the maximum saturation of the phase which is measured as the residual saturation of the water phase: $S_{mp} = S_{a,s}$. The relative non-wetting phase conductivity is given as

$$k_{r,a}(S_a) = \frac{k_a(S_a)}{k_a(S_{a,s})} \tag{2.66}$$

As seen in Figure 2.14, $k_{r,a}$ goes from zero, at a phase saturation below or equal to the respective emergence point, to one, at the matching point (Luckner et al. 1989).

2.5 Dynamic Water Transport

For isotropic media, the flux equations (equation 2.32) for the two observed fluids are:

$$j_w = -K_{w,sat}\,\frac{\partial p_w}{\partial z} \quad \text{and} \quad j_a = -K_{a,sat}\,\frac{\partial p_a}{\partial z} \tag{2.67}$$

Assuming constant density of the fluids, the material balance equations are obtained by considering a reference volume of bulk medium, including solid matrix as well as a representative portion of each of the two fluids. The resulting material balance equations are:

$$\phi\frac{\partial S_\alpha}{\partial t} = -\frac{\partial j_\alpha}{\partial z} \quad \text{with} \quad \alpha = \text{water; air} \tag{2.68}$$

The equations of the two phase flow are obtained by the substitution of the flux equations (2.67) with the expression for permeability (2.33) into the phase conservation equations (2.68):

$$\phi\frac{\partial S_w}{\partial t} = -\frac{\partial}{\partial z}\left[\frac{k_w}{\eta_w}\left(\frac{\partial p_w}{\partial z} + \rho_w \cdot g\right)\right] \tag{2.69}$$

and

$$\phi \frac{\partial S_a}{\partial t} = -\frac{\partial}{\partial z}\left[\frac{k_a}{\eta_a}\left(\frac{\partial p_a}{\partial z} + \rho_a \cdot g\right)\right], \tag{2.70}$$

where the correction for "gas slippage" has to be accounted for if necessary (Section 2.3.4).

This system of equations is coupled by the conditions (2.6)

$$p_c = p_a - p_w$$

and (2.4)

$$S_w + S_a = 1 \quad \text{where} \quad S_w = f(p_c).$$

If one fluid displaces the other the problem is analyzed by solving equations 2.69 - 2.70 simultaneously, with appropriate initial and boundary conditions.

In hydrological applications the involved air phase exhibits under natural conditions very small pressure gradients. The air viscosity is two orders of magnitude smaller than the water phase viscosity[9]. In this case the air phase viscosity may be neglected. Furthermore, the density of air is orders of magnitude smaller than the density of water. As a consequence, it may be justified to employ a passive air phase assumption where the air pressure is considered constant. This reduces the mathematical description of the problem by one equation, i.e. the water-air flow can be expressed with one single equation. The resulting one-dimensional Richards (1931) equation is usually written as:

$$C_w(\psi_m)\frac{\partial \psi_m}{\partial t} = \frac{\partial}{\partial z}\left[K(\psi_m)\frac{\partial \psi_m}{\partial z} - K(\psi_m)\right] \tag{2.71}$$

where the function

$$C_w(\psi_m) = \frac{d\theta}{d\psi_m}$$

is the specific soil water capacity, and ψ_m is the matric potential.

[9]Material properties for standard conditions (T_0=20 °C, p_0=101.3kPa) (Lide and Frederikse 1996)

fluid	density [kg/m^3]	dyn. viscosity [Pa·s]
water	998.2	$1.002 \cdot 10^{-3}$
air	1.25	$1.8 \cdot 10^{-5}$

3 Material and Methods

Direct determination of soil hydraulic properties in steady state experiments is very time consuming. The pressure saturation measurement can take a long time until a steady state is reached, especially in the drier range of the measurement where the hydraulic conductivity is low. To measure unsaturated conductivity at different pressures it is necessary to establish a constant pressure and flux within the sample, which is also a difficult task.

A suitable method of determining hydraulic properties, is the dynamic measurement of pressure induced water outflow, with high temporal resolution, in combination with inverse modeling of the underlying transient flow processes. The concept of the multistep outflow approach which was used for this study is described in Section 3.1. The experimental setup and the measurement procedure which provides necessary information about cumulative outflow of water, tensiometer potential, and air conductivity is described in Section 3.2. The preparation of the samples and settings of the technical equipment for a combined measurement of water and air dynamics is described in Sections 3.3 and 3.4, respectively.

Estimation of hydraulic properties with the inverse modeling tool `eshpim` is described in Section 3.5. The method for the evaluation of measured air conductivity data is introduced in Section 3.6.

3.1 Multistep Outflow Method

Measurement of transient outflow data and the inverse approach of solving the one-dimensional Richards equation numerically began in the 1980's. Kool et al. (1985) made onestep outflow experiments and compared their parameter estimations with steady state measurements. This method required additional independent measurements of soil water content data (van Dam et al. 1992) or matric head data (Toorman et al. 1992) in the optimization procedure to reduce problems of uniqueness. These problems were circumvented with the multistep outflow method invented by van Dam et al. (1994). Pressure had been changed in several small steps and the response of the system in stages provided sufficient information in the multistep outflow data, for a unique estimate of hydraulic functions. In the following several improvements were made with the multistep outflow method including automated

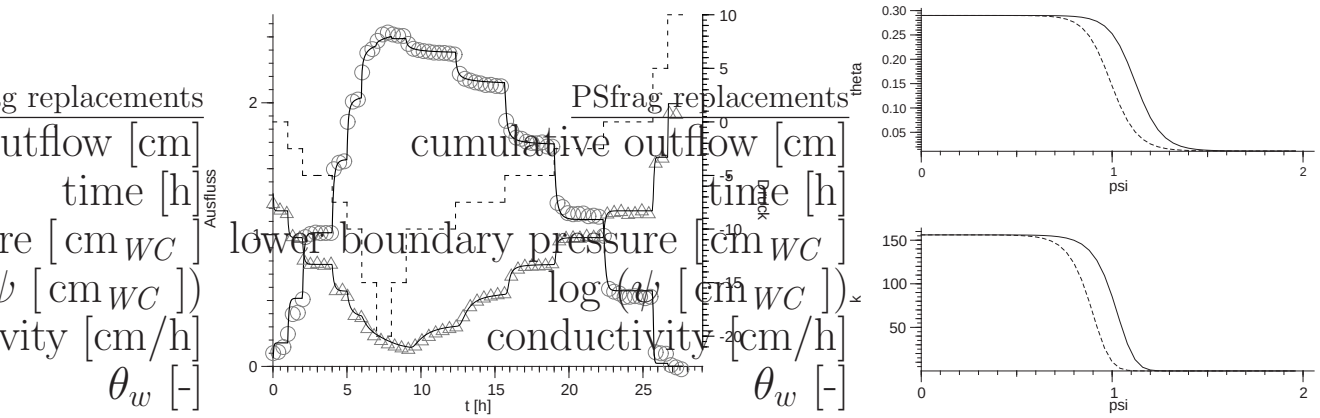

Figure 3.1: Left: Multistep outflow measurement curve. Lower boundary pressure (dashed, right axes), cumulative outflow, and tensiometer measurements (symbols) together with respective simulation results (solid lines). Right: Hysteretic hydraulic functions as evaluated by inverse simulation from the drainage (solid lines) and the imbibition (dashed) branches of the outflow curve. Top: Pressure saturation relation. Bottom: Conductivity pressure relation.

matric head measurement, or additional moisture measurement by TDR, or gamma attenuation, which increased the uniqueness of the parameter values (Hopmans et al. 2003). The combination of cumulative outflow data with tensiometric data in the objective function improved the method by producing more accurate estimations of the hydraulic functions for a wide range of soil textures. The problem with this method lies in the description of underlying process models. The unsaturated conductivity functions can only be estimated with a satisfactory validity if the retention model is able to describe the relation (Durner et al. 1999).

Figure 3.1 (left) shows an example of a typical multistep outflow experiment. The examined sample was a coarse-textured sand column with a height of 10 cm. Starting from full water saturation, the water phase pressure was decreased in stages as shown in the figure by the dashed line. The symbols ($\circ$: cumulative outflow, $\triangle$: tensiometric potential) show the response of the system on the change of lower boundary pressure where the outflow was measured in cm^3/cm^2. Information about air entry pressure was provided by the beginning of outflow. The slope of the $\theta(\psi)$ distribution was provided by the height of the outflow steps in corelation to the applied pressures. The height of the distinct pressure steps played a crucial role for the estimation of the retention characteristic. Hydraulic conductivity could be estimated from the shape of the outflow steps and the difference between saturated and residual water content could be estimated from the maximum value of cumulative outflow.

Results of the evaluation of hydraulic parameters by one-dimensional inverse simulation are shown in the same figure with the solid lines representing outflow curve and tensiometric potentials, respectively. Hysteretic retention and conductivity curves on which the simulation was based is shown in the right part of Figure 3.1.

3.2 Experimental Setup for Multiphase Measurements

The apparatus presented in Figure 3.2 consists of three major units, a control unit and two separate units for the measurement of water flow and air dynamics. The control unit is represented in the figure by a computer and vacuum containers. The computer is used for logging and storing pressure sensor data and for switching of the magnetic valves. The vacuum containers provide the low pressures, necessary for the experimentation. The multistep outflow measurement device is shown on the left hand side of the figure while the air-flow measurement device is presented on the right hand side. The sample holder is located in the upper central region of the figure.

3.2.1 Mulitstep Outflow Measurement Device

The multistep outflow part of the experimental setup was based on the classical arrangement of the sample and the measurement device. The column with a maximum diameter of 168 mm was placed vertically on a porous plate. System disturbances which induce transient out-/inflow were applied via water phase pressure at the lower boundary of the sample. The custom method for the lower boundary connection, applying a thin nylon membrane with a high air entry value and low resistance to the water phase could not be used here. For additional examination of air-flow behavior in the hydraulic and pneumatic measurements, the fluid phases had to be separated. Therefore, a segmented porous sintered glass plate was used which is described in detail in Section 3.2.3. For the hydraulic measurement, the hydrophilic sintered glass part of this plate was used as interface between the sample and measurement devices. The glass had an air entry pressure much lower than the measurement range during the experiments, i.e. it had been water saturated during the whole experiment.

The left part of Figure 3.2 shows the device for the determination of hydraulic properties (water-flow). The lower boundary pressure was mixed in a pressure barrel by switching the valves V_1 which was connected to a -500 hPa vacuum reservoir and V_2 which was opened to atmosphere. The lower boundary pressure was monitored by the pressure sensor PS_1 and the software adjusted the pressure by switching the corresponding valve.

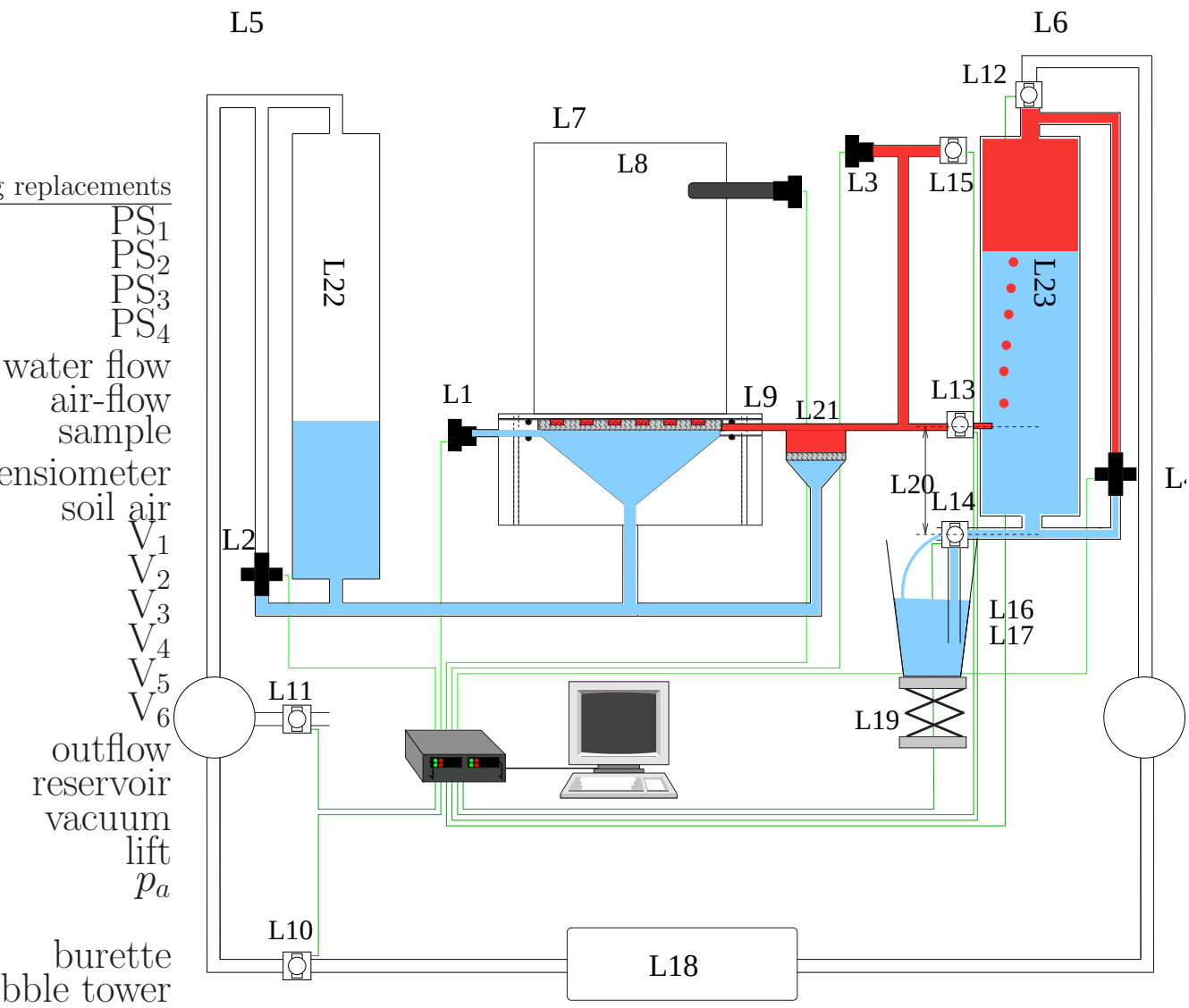

Figure 3.2: Setup for simultaneous measurement of water and air dynamics. The sample (center) is mounted on a phase separator (see Figure 3.4). Water flow (left) is measured by the multistep outflow method. Water pressure at lower boundary is controlled by magnetic valves V_1 and V_2 with feedback from pressure sensor PS_1. Cumulative outflow is collected in a burette and monitored by sensor PS_2. Air-flow measurement (right) is conducted by collecting the cumulative outflow in a Mariotte bubble tower. Air pressure is controlled by height of outlet which is adjusted by the lift, the applied pressure is measured by sensor PS_3. Cumulative air volume is measured by sensor PS_4. Valves V_3-V_5 are used to refill the bubble tower. V_6 is for drainage of the air grid within the separator plate.

For the experiment, the water pressure was changed in single steps at the lower boundary and the corresponding cumulative outflow was collected in the burette where the water table was monitored by the differential pressure sensor PS_2 and logged with high temporal resolution by the computer.

3.2.2 Mini-Tensiometers

To improve the parameter estimation with the inverse procedure, the tensiometer potential was measured during the multistep outflow measurements. With this method the speed of the spreading pressure front and the actual capillary pressure at a specific position could be measured. As some of the materials were rigid, it was not possible to use custom tensiometers, which have to be placed inside the samples. The special external tensiometer designed for measurement with rigid media is sketched in Figure 3.3. This instrument consists of a slice of sintered glass, thickness 4 mm, with a high air entry value ($> 150\,\mathrm{cm}_{WC}$). Conductivity of this material is 0.4 cm/h. The membrane has a rigid plastic tube casing. The tip had to be as flat as the surface of the sample on which it was placed, for maximum contact. Contact area could be improved by some contact material (fine sand, gaze, ...) and an additional rubber casing prevented the tensiometers from drying up during a measurement. For external use, the tensiometer was adjusted properly at the column surface and tightened in a chuck to maximize hydraulic contact.

With the setting used the pressure sensor measured capillary pressure as the difference between water pressure and atmospheric air pressure outside the column. For internal use of tensiometers in the sand packings it had to be taken into account that air pressure of entrapped air might be higher than atmospheric air pressure and the tensiometer might only measure water pressure and not capillary pressure.

3.2.3 Air-Flow Measurement Device

Current methods of multistep outflow analysis are based on the basic assumptions that gas and water flow in the porous medium can be decoupled as the governing Richards equation (2.69), on which the inversion is based, includes the hypothesis that the gas phase in soil is always at atmospheric pressure (Section 2.5). Since the air phase viscosity is much larger than water phase viscosity, $\eta_a > \eta_w$[1], air should be at atmospheric pressure throughout the unsaturated medium.

As mentioned above, the aim of the device designed for this study was a simultaneous measurement of hydraulic and pneumatic properties of the laboratory sized soil columns. To detect a continuous air phase through the sample, a vertical setting of air-flow measurement was chosen. Direction of air-flow was top-down where air was extracted at the lower boundary which reduced phase interactions to a minimum.

[1]For the material parameters at standard conditions see footnote on page 44

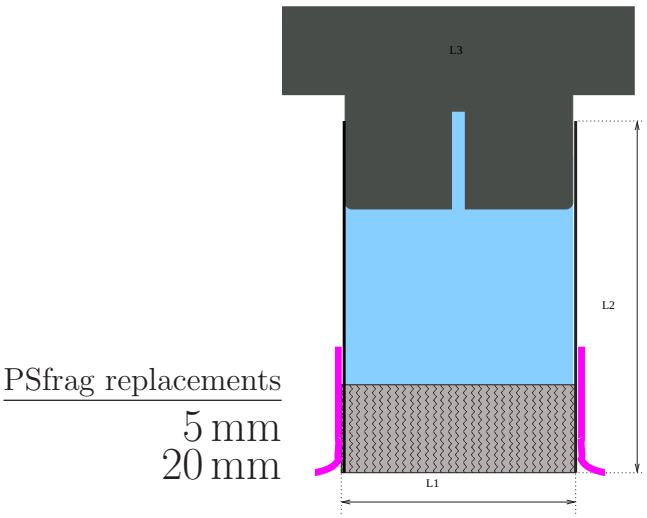

Figure 3.3: External tensiometer designed for use with rigid porous media. The porous sintered glass plate (light grey) connects to the pressure transducer via a firm plastic tube. The rubber band (magenta) is used for sealing.

With the additional information about air continuity and air conductivity along the z-axis the saturation range at which Richards equation is valid for the entire column could be ascertained.

Phase Separation

For simultaneous measurement of hydraulic and pneumatic properties of the porous medium in a single experiment there was a need to separate the involved phases (solid, water, and gas). For this purpose a phase separator for the lower boundary was designed which allowed the control of the boundary conditions for air- and water-pressure and provided an interface for further devices to measure air- and water-flow (Figure 3.4). The vertical arrangement of the sample had the disadvantage that the whole weight of the sample was loaded at the separating interface. As mechanical stability was required on the one hand and conductivity of the plate had to be maximized on the other, a sintered glass plate of 10 mm thickness was constructed. This plate was supported by an underlying PVC grid which was part of the plate holder[2].

For the separation of fluids, wetting properties and air entry pressures of different porous materials were utilized. The sintered glass with an air entry pressure of $-500\,\mathrm{cm}_{WC}$ was the hydrophilic part (small contact angle). Water percolating

[2]First test with thinner plates and a different grid geometry always caused the plate to crack when a column was placed on top and additional to this a pressure was applied. See also Appendix A.2

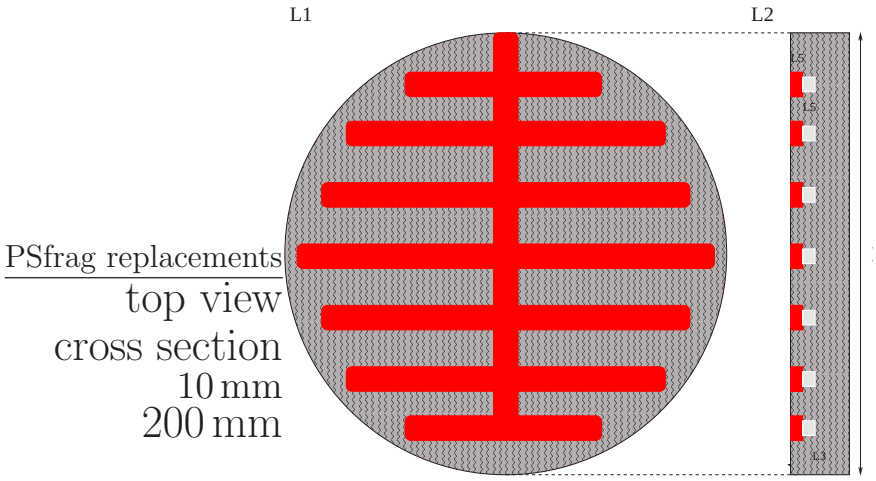

Figure 3.4: Porous plate to separate air and water at the lower boundary: hydrophilic sintered glass plate (grey), hydrophobic sintered HDPE (red), and air channel (light grey) to facilitate air-flow.

	sintered glass	HDPE
pore diameters [μm]	5-8	500-1000
contact angle [°]	<10	160
porosity [%]	48	52
conductivity [cm/h]	18	>500

Table 3.1: Physical properties of the two materials used for separation of the fluids at the lower boundary.

through this plate was collected in a funnel and passed to the burette where it was gathered cumulatively. As a path for extraction of soil air, 3 mm deep channels were milled into the glass plate and covered with a 1.5 mm layer of sintered hyper-dense polyethylene (HDPE), a hydrophobic material (large contact angle) with pores $> 500\,\mu m$. The 1.5 mm channel below the HDPE-grid was an air conduit which avoided distance effects within the plate, and improved air conductivity inside the device. The physical properties of the two materials used for phase separation are summarized in Table 3.1.

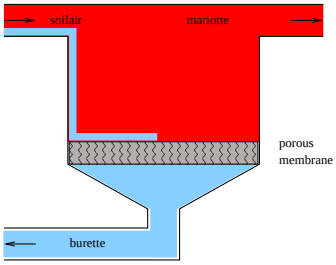

Figure 3.5: Additional separator

A major hurdle with the separation of the phases was the flow of water through the air channels caused by thin films or spontaneous movement of small drops. Since it was not possible to avoid a minimal flow of water through the air outlet of the

sample holder an additional water separator (Figure 3.5) was installed directly at the air outlet of the sample holder. The chamber with the air in- and outlet at the upper end had a porous membrane, 3 mm thick, at the bottom which was in contact with the water collecting burette. Water pressure in this separator was the same as the pressure applied to the sample. Any water leaving the sample at the air outlet was added to the cumulative outflow burette by this construction.

Measurement of Air Volume

The determination of air conductivity in laboratory experiments required a highly precise and flexible instrument for the observation of flow rates. Flow chambers or soap film permeameters are typically used for this purpose, as they offered recommended precision (e.g. Wu et al. (1998), Moldrup et al. (1998), Corey (1986)), but since these are not automatically operated, a necessity for the experiments which lasted for many weeks, they were of no practical use.

The most adequate instrument which met all requirements was the Mariotte bubble tower. With this instrument, flow measurement of high resolution in time and volume could be made. The air pressure, adjusted by a lift (Figure 3.2, right), could continuously be measured by pressure sensor PS_3. Also by this method, a very small and permanent air pressure difference of 0 - 5 hPa could be applied with a precision of ± 0.05 hPa. The simple concept along with the static settings of the bubble tower made it a very robust instrument for air volume counting. Resolution of the measured volume was influenced by both the response time of the sensor and the width of the used air outlet which shapes the bubbles to a specific discrete volume. The outlet diameter of 5 mm, was the best compromise between both the intrinsic conductivity of the instrument and resolution of measurement.

The air influx collected in the bubble tower where the height of the water table was monitored via differential pressure sensor PS_4. Although this technique was limited by the volume of water in the tower it was the most flexible method for air conductivity measurements. The burette could collect about 900 cm^3 of air. After this amount had passed through the soil column the burette had to be refilled. The valves V_3 - V_5 were switched and the vacuum sucked the water back into the tower. The refill interruption took about 5 minutes, and did not affect the air-flow measurement. If necessary, a second tower could be installed and they could both be used in an alternating mode without interruption.

If the gravitational component of the driving force is negligible compared to the force resulting from the applied pressure gradient, then the one-dimensional isothermal flow of air can ideally be described by the extended Darcy equation for gases

$$j_a = \frac{k_a}{\eta_a} \frac{dp_a}{dz} \tag{3.1}$$

where j_a is the volumetric flux, η_a is viscosity, dp_a/dz is the pressure gradient in

PSfrag replacements
water-flow
time
ative outflow [cm]
bc_{air}
bubble tower [cm]
bc_{air} [hPa]
bc_{water}
bc_{water} [cm_{WC}]
ow (bubble tower)
nductivity [cm/h]

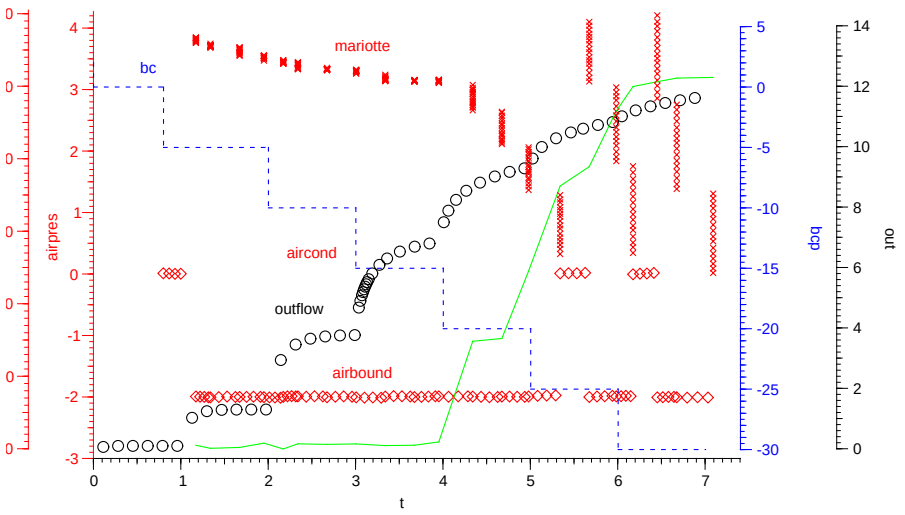

Figure 3.6: Example of an air-flow measurement. Blue: Lower boundary pressure (water). ○: Cumulative outflow of water. Red: ×: Measured height in Mariotte bubble tower; ◇: Lower boundary pressure (air). Solid line: Effective air conductivity.

z-direction, and k_a is air permeability. Because of the laminar flow, a correction for the compressibility of the gas is not required.

A correction due to the Klinkenberg Effect (Section 2.3.4) was not necessary for this study because the pore diameters were large enough and the applied air pressure gradients were small. Several experiments, with various air pressures gradients applied to coarse and fine-textured columns, found linear dependence between pressure and volume, i.e. k_i was constant and there was no influence of gas slippage which corresponded to the results of a study by Wu et al. (1998).

Figure 3.6 shows an example of a combined multistep outflow and air conductivity measurement. Hydraulics are represented by the blue dashed line which is the lower boundary pressure applied to the water phase[3] and the black circles which denote the cumulative outflow[4]. Pneumatic measurements are represented by the lower boundary pressure applied to the air phase[5] (red diamonds), the air volume cumulated in the bubble tower[6] (red crosses), and the solid green line gives the effective air conductivity calculated with equation 3.1.

The air-flow measurement started at a water pressure less than $0\,cm_{WC}$[7]. The

[3] measured with pressure sensor PS_1 (see Figure 3.2)
[4] measured with differential pressure sensor PS_2 (see Figure 3.2)
[5] measured with pressure sensor PS_3 (see Figure 3.2)
[6] measured with differential pressure sensor PS_4 (see Figure 3.2)
[7] With the vertical arrangement of the setup and the separator at the lower boundary it is not possible to measure air-flow at water pressures higher than $0\,cm_{WC}$ because the air grid is

air grid was drained by opening valve V_6 for 5 minutes (Figure 3.2). The water which was collected in the burette was not added to the cumulative outflow to avoid misinterpretation of hydraulic data. For air-flow measurement valve V_4 was opened. Lower boundary air pressure was kept stable during the whole period of measurement. Interruptions in the lower boundary air pressure occurred if the bubble tower had to be refilled (after 5.5 and 6.5 hours).

With the experimental setup described above, it was possible to measure an integrated air-flow through the sample. To get air-conductivity relations which were corrected for all influences of vertical saturation gradients due to gravity effects this measurement had to be evaluated by concerning these effects. The method of data analysis is described in Section 3.6.

3.3 Preparation of the Samples

For the measurement of multiphase properties it was absolutely essential to have a well prepared sample. Any open voids between the sample and the measurement device can have unpleasant consequences. In the case of hydraulic measurement gaps could lead to capillary barriers during imbibition which could have an impact on the estimation of hydraulic conductivity. In the case of the measurement of pneumatic properties, air-flow leaks along the boundaries prepared a kind of shortcut, which increased air conductivity. Air inclusions in the primary drainage cycle could also lead to measurement errors.

Sealing

Boundary effects were reduced by the sealing of the samples with special care for all possible gaps at each boundary. Several wrapping and sealing techniques were tested on the rigid porous media. Latex casings had the advantage of being able to follow the shape of the columns. However, for fully saturated samples the elastic membrane gave way to the pressure and additional water was found inside the casing but outside the sample. This effect led to errors in maximum water saturation. Silicone gaskets influenced the surface of the glass beads. Wettability of a column wrapped in silicone was reduced at the boundaries. A similar effect was reported by Corey (1986), where an extremely small contamination with silicone-based lubricant for stopcocks, prevented the formation of stable soap films in a flow meter and was extremely difficult to remove. Best results were achieved for the rigid materials with shrinking PVC tubes, a product normally used in the electronic field. A tube was slipped over each sample and heated until shrunken to the minimum size. The warm tube adapted to the shape of the sample surface and the gaps were closed.

Installation of the wrapped sample in the sample holder also required water- and air-tight boundaries. For this purpose the rigid columns were first sealed in

saturated with water then.

the sample holder then evacuated in the desiccator and finally mounted on the separator plate. Effects of initial air inclusions and boundary gaps were removed by this procedure.

Sealing problems did not occur with the sand packings as they were compiled directly in the sample holder. The flexible sand fitted the sample holders geometry and boundary gaps were possible only within the grain size of the respective sand.

Saturation

For examination of primary drainage curves all measurements had to start in a fully water saturated state. The method of slow capillary rise led to insufficient results as there was still entrapped air in the samples. For the rigid samples, capillary rise led to 90 % water saturation only. The remaining air was removed by saturation in a desiccator. With this method air was totally removed from the sample. Different durations and pressures were tested and best results were achieved when samples were kept for 24 hours in the desiccator at a pressure of $-500\,\mathrm{cm}_{WC}$.

This type of saturation did not work for the nonrigid sand. In every experiment the dry sand was poured into the water-filled sample holder, which led to full saturation. As the sand took the shape of the sample holder, and since neither swelling nor shrinking occurred, no extra sealing was necessary.

Hydraulic Contact

The main disadvantage of rigid materials was the hydraulic contact at the interface between the sample and the measurement device. Although the sample bases and the porous separator plate were grind flat, installation of the samples in the holder would lead to small vertical rotations which would cause gaps at the interface in the range of some hundred micrometers. These gaps made data analysis impossible because conductivity of the whole system was disturbed, especially in the imbibition part of the measurement. The problem was solved by adding a thin cotton mesh as an immersion layer. The elastic mesh was able to close gaps and allowed water and air to pass in their distinct compartments of the separator plate. The influence on the hydraulic and pneumatic conductivity was taken into account as saturated conductivity of the separator plate was measured with the mesh installed.

Tensiometers were also connected to the sample via cotton meshes when they were used in the external mode. For internal use of tensiometers in the sand packings it was necessary to avoid gaps between the instrument and the sample. These types of gaps could lead to a loss of hydraulic contact between the instrument and the sample and therefore distort air conductivity measurements by offering air channels. After installing the tensiometer water was poured into the area around the instrument which made the sand flow through the gaps and close them.

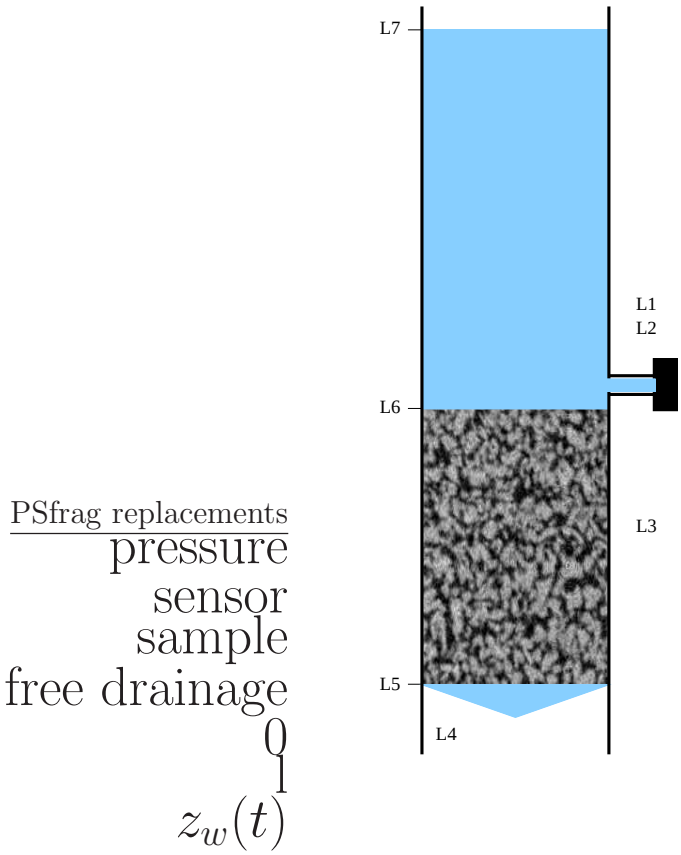

Figure 3.7: Falling head permeameter for the determination of saturated hydraulic conductivity (Klute and Dirksen 1986).

Saturated Conductivity

For modeling of the experimental results, saturated hydraulic conductivity of the separator plate had to be included in simulations. $K_{w,sat}^{plate}$ was measured with the "falling head method" (Figure 3.7, Klute and Dirksen 1986). The plate was ponded with water and during free drainage the water-level $z_w(t)$ was monitored by a pressure sensor. With this information the saturated conductivity of the plate could be calculated using Darcy's equation:

$$K_{w,sat}^{plate} = -\,l \cdot t \cdot \log \frac{z_w(t)}{z_0} \tag{3.2}$$

with the initial height of the water table z_0, thickness of the plate l, and duration of drainage t. The measured values which were used for simulations of measured data are listed in Table 3.1.

The measurement of saturated hydraulic conductivity of the separator plate was repeated after every experiment, because small particles could have been eroded

in the sample and settled down on the plate during the measurement. With the materials used no change in saturated conductivity of the plate was observed.

The falling head method was also applied to measure the saturated conductivity of the examined samples. The rigid columns were placed in a tube and ponded with water, the sand packings were measured together with the separator plate. Conductivity of the plate and the sample were separated by

$$K_{sat}^{sample} = \frac{l_{sample}}{\frac{l_{sample}+l_{plate}}{K^{total}} - \frac{l_{plate}}{K_{sat}^{plate}}} \tag{3.3}$$

Temperature and Humidity

Measurement of hydraulic and pneumatic properties depended on the temperature and humidity of the surrounding area. Influences were kept small by a climatic locker where these parameters could be held in stable values. Because of interferences between the locker's electronics and the measurement electronics the locker was used to establish a homogeneous humidity (almost 100 % rel. humidity) at room temperature (varied between 23 - 26 °C) and was shut off afterwards. While the experiments were running it worked as insulation. The premoistened air prevented drying of the samples during air-flow measurement.

3.4 Experimental Settings

Calibration of Pressure Sensors

All pressure sensors involved in the experiments were calibrated every time they were used (for technical details of the sensors see Appendix A.1). Linearity between the applied pressure and the digital output signal was constant over a long period of time ($>$ 1/2 year) but the offset could change within a few weeks. Because of this effect, calibration was done before and after every measurement. In theory, the drift of the offset could be corrected if there was measured data parallel to the drifted; otherwise the experiment would have to be repeated. All pressure sensors worked with an absolute precision of $0.1\,\mathrm{cm}_{WC}$.

Software Handling

Realization of the simultaneous multistep outflow and air-flow measurement and evaluation of the measured data required several software tools. To make the handling of all used software easier, they were merged in an easy to use front-end. This graphical user interface (GUI) was developed in LabView (Instruments 2001) which is a graphical programming language that offers special features for user dialogs, data processing, and online data visualization. With this GUI, all input file editing which is necessary for the software and which controls the experiment can be prepared stepwise:

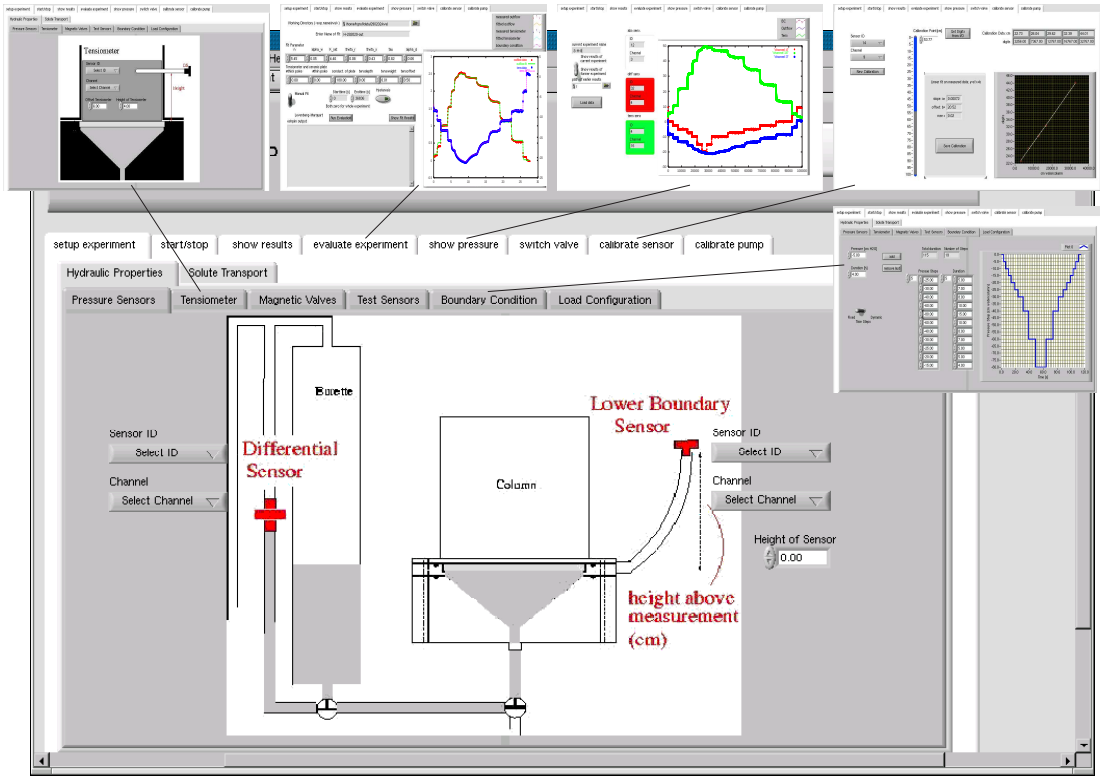

Figure 3.8: Graphical user interface for setup, control and evaluation of multistep outflow experiments. The tab structure allows only a small insight to all available features.

- calibration of all sensors used (absolute/differential)
- administration of available sensors
- controlling of sensors and magnetic valves
- boundary condition settings for the multistep outflow and air-flow measurement
- logging and online visualization of pressure sensor data
- evaluation of hydraulic parameters with the `eshpim` program
- visualization of fitting results and hydraulic functions

Figure 3.8 shows a part of the GUI which is arranged in a tab structure[8]. With this panel configuration, termination, supervision, and evaluation of the experiment could be done in an intuitive convenient way while the specific tools were working in the background.

Boundary Conditions

A typical transient water flow experiment started with the water-saturated column. Pressure at its lower end was reduced in a series of steps to some minimal value, then increased again through a series of steps to its starting value. The experiment was controlled and monitored by a computer with a highly temporal resolution, i.e. all pressures were recorded every ten to sixty seconds. The typical duration of a multistep outflow experiment was about 40 - 60 hours for the main drainage and imbibition curves.

The additional air-flow measurement had to be started at a lower boundary water pressure $< 0\,\mathrm{cm}_{WC}$. After the drainage of the grid, the two phases could be separated at the lower boundary and the flow of each fluid could be measured in the designated parts of the apparatus.

Application of an air pressure gradient could have lead to the redistribution of water during the air conductivity measurements. Large air pressure gradients could also have burst some of the water films blocking pores to gas movement (Ball et al. 1981) and the Reynolds number could have become large enough for laminar flow to begin changing to turbulent flow, where Darcy's law no longer holds. The effect should have been minimized by using only air pressure differences up to 5 hPa. But instead, a test of several measurement modes showed that the best results were achieved with a selective mode at specific points correlating to the water outflow curve. To reduce any kind of influence on the hydraulic measurement, air conductivity was measured at the beginning of a hydraulic pressure step after the fast rise of the outflow curve, and depending on duration, at several additional times during the redistribution phase of the step. If the phases were separated properly, both measurements should not have influenced each other[9].

In the rewetting phase the air-flow measurement was stopped at a lower boundary pressure of $0\,\mathrm{cm}_{WC}$ which prevented a rise of the water-table higher than the separator plate.

[8] The whole GUI was organized into three levels, general settings, experiment type settings and experimental settings. All three levels had different panels where specific features could be set. The different panels could be accessed by the tabs of the panels.

[9] Any disturbances of the hydraulic data would have shown an inadequate separation and would have made the measurement worthless.

3.5 Estimation of Hydraulic Parameters

The inverse modeling approach estimates soil hydraulic properties from transient experiments, giving much more flexibility in experimental boundary conditions than required for steady state methods. Scanning of hydraulic state variables, θ and ψ, can be done continuously over a wide range of pressures. With this approach both the soil water retention and the unsaturated conductivity function can be estimated from a single transient experiment. The governing equation for this process which is used for simulations is the Richards equation. Evaluation of the dynamic water flow experiments was done with the inverse simulation code `eshpim` (**e**stimation of **s**oil **h**ydraulic **p**roperties by **i**nverse **m**odeling), which was developed by Zurmühl (1996). Using the lower boundary conditions, the cumulative outflow data and the tensiometer potential, hydraulic parameters were determined by a combination of solving Richards equation (equation 2.69) numerically (direct problem) and by a method for solving the minimization problem for the parameters used (equation 2.15). A brief summary of the parameter estimation of `eshpim` is given in the following section.

Direct Problem

Simulations of the direct problem were based on the one-dimensional Richards equation in the mixed form (Celia et al. 1990):

$$\frac{\partial \theta}{\partial t} = \frac{\partial}{\partial z}\left(K(\theta)\frac{\partial \psi}{\partial z} - K(\theta)\right) \tag{3.4}$$

where θ is the volumetric water content, t is time, z is depth, $K(\theta)$ is hydraulic conductivity and ψ is the matric head. For hydraulic functions the van Genuchten – Mualem approach with their respective parameterizations were used.

Additionally initial and boundary conditions as used in the experiment had to be specified. Finite differences simulations were done for n discrete nodes of spacial discretization and a fully implicit method for temporal discretization.

Inverse Problem

The parameter set was improved iteratively until the deviation between measured and calculated values was minimal. The target function which had to be minimized by the least squares method is:

$$\chi^2(\boldsymbol{\eta}) = 1/2\,[\mathbf{y} - \mathbf{f}(\mathbf{x}, \boldsymbol{\eta})]^T\,\mathbf{W}\,[\mathbf{y} - \mathbf{f}(\mathbf{x}, \boldsymbol{\eta})] \tag{3.5}$$

with

	$\boldsymbol{\eta}$	parameter vector, $\boldsymbol{\eta} = (\eta_1, \eta_2, \ldots, \eta_o)^T$, ($T$: transposed)
	o	number of parameters
	$\chi^2(\boldsymbol{\eta})$	sum of least squares
	$\mathbf{y}$	vector of measured values y_i, $i = 1, \ldots, l$;$\mathbf{y} = (y_1, y_2, \ldots, y_l)$
	$\mathbf{f}(\mathbf{x}, \boldsymbol{\eta})$	calculated values

$\mathbf{x}$	$l \times k$-matrix with k independent variables (time, space) and l values
$\mathbf{W}$	$l \times l$-matrix with weighing factors

Kool et al. (1985) developed a method for the use of more data sources with specific weighing factors. With this approach all measured data (outflow, tensiometer potential, saturations, ...) could be used for optimization.

To solve the problem, `eshpim` used the Levenberg-Marquardt algorithm. Equation 3.5 was minimized by finding the zero point of the derivative related to η. This resulted in one equation for each parameter η_i. As the parameterization used was nonlinear, which lead to a nonlinear function in η, the system of equations was solved iteratively until a minimum was reached.

Mulitmodal Pore Systems

For structured soils, the water retention function is not always represented well by a unimodal model, if pore size distribution has additional maxima in the range of large pores. Several concepts of data evaluation have been developed during the last years which were able to describe multimodal pore systems (Ross and Smetten 1993, Durner 1994, Zurmühl and Durner 1998). The model implemented in the `eshpim` code is the one developed by Durner (1994) which describes the multimodal retention curves by a superposition of several van Genuchten curves:

$$S(\psi_m) = \frac{\theta - \theta_{w,r}}{\theta_{w,s} - \theta_{w,r}} = \sum_{i=1}^{k} w_i \left(1 + (\alpha_i \psi_m)^{n_i}\right)^{m_i} \quad \text{for} \quad \psi < 0 \tag{3.6}$$

with	k	number of different modes
	w_i	weight of single modes with $0 < w_i < 1$ and $\sum w_i = 1$

This type of multimodality assumes that the different pore systems are distributed homogeneously over the whole sample. This means that they have to be in contact with both the air and the water reservoir to show a simultaneous response. In the `eshpim` code a bimodal model is implemented which allows to distinguish between two different maxima in the pore-size characteristic.

Hysteresis Model

The hysteresis model implemented in `eshpim` was the constrained Kool and Parker (1987) model (Section 2.4.1). The model was based on main drainage and imbibition curve with known parameters. If wetting direction was changed from drainage to imbibition, θ_r of the drainage curve was changed to get a closed loop of drainage and imbibition retention curves. Since hysteresis in the $K(\theta)$-relation is insignificant for most problems (Topp 1969) it was neglected by `eshpim`. This constrained type

of the Kool and Parker model resulted in a single parameter α_2 for the imbibition branch which includes all hysteresis effects.

For fine grained homogeneous materials, the described hysteresis model was not sufficient. To get more flexibility in the hydraulic functions for both branches of the multistep outflow experiment, fitting of data was split into two separate parts. For this purpose hysteresis in the $K(\theta)$-relation was assumed. This model has been introduced as the Kool and Parker model in Section 2.4.1. The outflow branch was fitted with a complete set of parameters to an optimum agreement. For this set of parameters, tension and water contents were simulated for the reversal point where the lower boundary pressure changed from drainage to imbibition. These simulation results were used as initial conditions for the simulations of the imbibition curve. As the columns response to the change from drainage to imbibition was delayed, measured data could not be used for fitting until the change was carried out. Estimation of hydraulic properties were done with a full set of parameters for the second branch of the multistep outflow curve which led to a better correspondence between measurements and simulations.

Statistical Characteristics

During the parameter optimization procedure, statistical characteristics for fitted parameters were calculated. The correlation of parameters was evaluated by the correlation matrix:

$$c_{ij} = b_{ij}(b_{ii}b_{jj})^{-0.5} \tag{3.7}$$

with
- b_{ij} elements of matrix $\mathbf{B} = (\mathbf{J}_w^T\mathbf{J}_w)^{-1}$
- $\mathbf{J}_w$ $\mathbf{SJ}$
- $\mathbf{J}$ Jacobian matrix
- $\mathbf{S}$ Cholesky splitting of matrix $\mathbf{W}$

where high correlation of two parameters meant that there was not enough measured data for independent evaluation of both parameters or there was a physical correlation which was not taken into consideration by the underlying model.

Additionally the confidence intervals for all parameters were calculated by:

$$\eta_j - b_{jj}^{0.5}s^2t_{1-\alpha/2}(n-p) \leq \hat{\eta}_j \leq \eta_j + b_{jj}^{0.5}s^2t_{1-\alpha/2}(n-p) \tag{3.8}$$

with
- η_j calculated parameter value
- $\hat{\eta}_j$ 'apparent' parameter value
- $t_{1-a/2}(n-p)$ value of t distribution for confidence number $1-\alpha$ with $n-p$ degrees of freedom
- $s^2 = \frac{\mathbf{r}_w^T\mathbf{r}_w}{n-p}$ variance in error

As the correlation matrix and the confidence intervals were found by linear regression methods they did not really reflect the true values for the nonlinear system. The confidence interval should have been seen as a confidence region. All statistic results were only valid if the calculated parameter vector was the 'true' minimum (for more details about the `eshpim` parameter estimation program see Zurmühl 1994, Zurmühl 1996).

3.6 Calculation of Air Conductivity

The calculation of air conductivity based on the measurement which was introduced in this chapter had to consider the fact of a water saturation gradient within the sample due to the transient conditions of the experiment and due to gravity effects during the stationary periods of the experiment. Measured data, which reflected an integral response of the entire system had to be compared to locally and temporally discretisized simulations. With simulated local properties, global properties could be calculated and compared with measured data.

Simulation of Water Dynamics

Evaluation of measured air permeability data required knowledge of the part of pore space available for the gaseous phase. Simulation of water dynamics therefore resulted in a vertical discrete distribution of water content within the sample. Hydraulic functions evaluated by inverse modeling were used for one dimensional simulations and the direct problem was solved as described in Section 3.5. Spatial resolution of the sample height was 0.05 - 0.2 mm. Temporal resolution followed closely the times of measured data recorded with the multistep outflow experiments. A result of this modeling was the temporal evolution of vertical profiles of local water saturations (Figure 3.9 center).

Simulation of Air Conductivity

The simulated water saturation profiles were used to calculate effective pneumatic conductivity over the whole height of the columns. For the three models introduced in Section 2.3.4, effective air saturation and the resulting air conductivity were calculated for a discrete one-dimensional sample. Air conductivity of the entire column was calculated with:

$$\frac{1}{k_{a,c}} = \frac{H}{\sum_n \frac{h^*}{k_{a,n}}} \tag{3.9}$$

where $k_{a,c}$ effective air conductivity of the column
H height of the column
h^* height of an element
$k_{a,n}$ effective air conductivity of element n
n number of elements

Modeling of local pneumatic properties was based on the effective hydraulic parameters estimated from the multistep outflow experiments. For heterogeneous samples pneumatic properties were calculated based on the material properties of the homogeneous components used for assembling. For simulations of the structured samples the bimodal approach was used as proposed by Zurmühl and Durner (1998).

The pneumatic conductivity models VGM, VGB, and EP introduced in Section 2.4 were chosen as they are based on three different concepts for the pore space which was available for air phase transport. The van Genuchten-Burdine model (VGB), was based on the parallel capillary approach with the empirical shape parameter, is supposed to reflect the geometry of the hydraulic but not the pneumatic flow (Dury et al. 1999). Therefore this model was expected to underestimate the pneumatic conductivity. The van Genuchten-Mualem model (VGM), with the concept of cut and rejoined pores reflected the effects of geometry better since the combination of different pore radii in series result in an effective conductivity depending on the ratios of radii and lengths. For both models, the nonwetting phase conductivity was predicted from an effective air saturation which was the pore space complementary to the effective wetting phase saturation. For the emergence point model (EP) the air content was rescaled by equation (2.64) to reflect the effective mobile air saturation. The additional free parameter of the EP model, the emergence point water saturation, was fitted for the homogeneous materials to measured data. For heterogeneous samples all values evaluated from the homogeneous materials were used for simulations.

For an overview of underlying measured data, all resulted data of water dynamic simulations and modeling of pneumatic properties were plotted together (Figure 3.9). The top figure shows the hydraulic data measured in the multistep outflow experiment as symbols and the simulation results for hydraulic functions based on the estimated parameters as solid lines. The central part shows the temporal evolution of water saturation in a vertical profile of the sample. Nodes with saturation higher than emergence point saturation are edged in black. The lower part of the figure shows the air conductivity as measured during the multistep outflow experiment as symbols and the simulated values for the specific water saturations with the VGM, VGB, and EP models, respectively. All plots are connected using the same time axis.

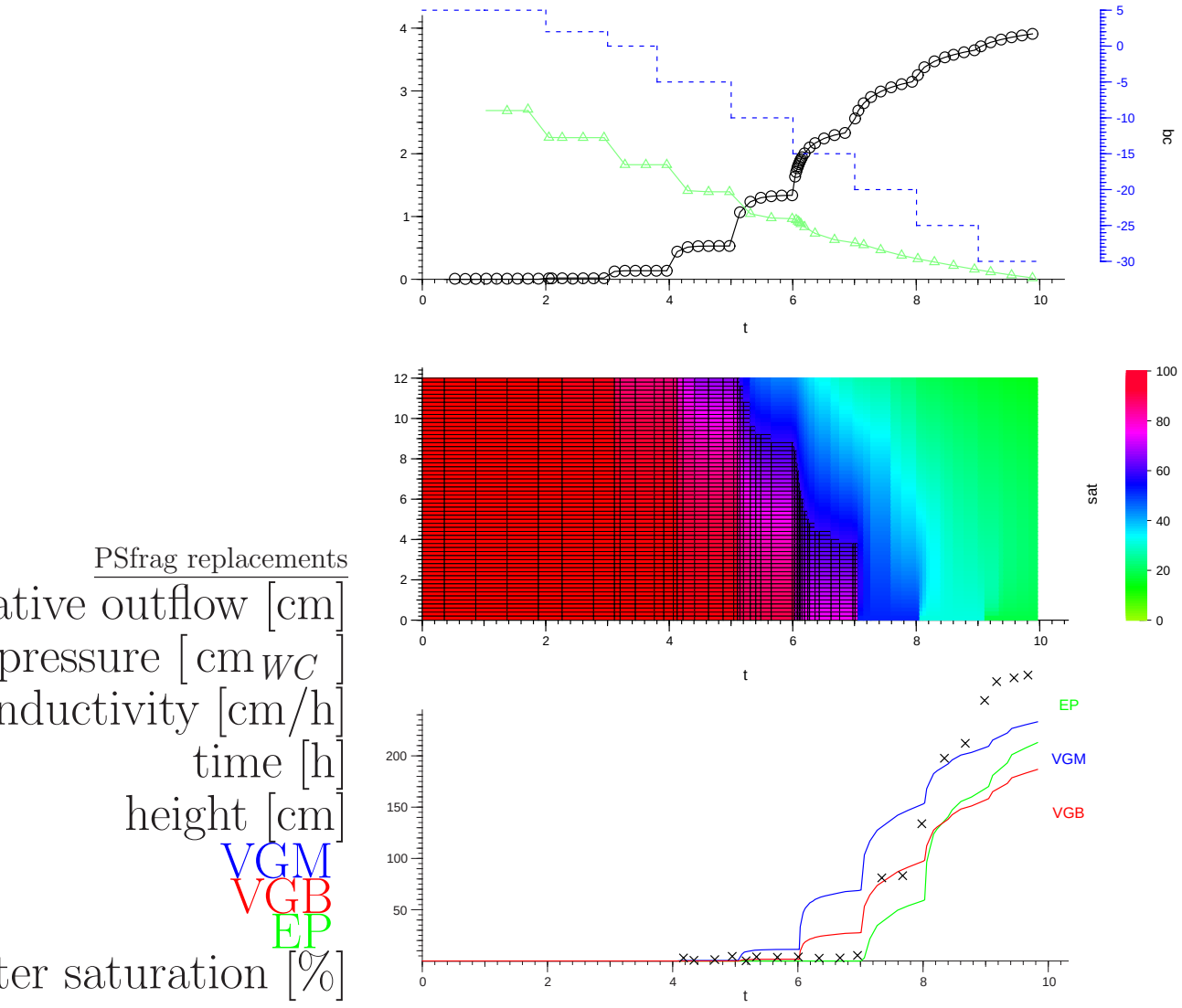

Figure 3.9: Example of data evaluation of combined multistep outflow and air-flow measurement. Top: Experimental data from multistep outflow experiment as symbols (dashed line: lower boundary pressure, ○: outflow, △: tensiometer) and results of inverse simulation as solid lines. Center: Temporal evolution of the water saturation of a vertical profile in the sample which is discretized in 60 nodes. The nodes with a black frame have a saturation greater than the emergence point saturation. Bottom: Simulations of the pneumatic conductivity by the VGM, VGB, and EP models, based on the water saturation shown above. All three plots use the same time axis which makes a comparison of results possible.

4 Experimental Investigations with Artificial Porous Media

A major hurdle when looking into fluid flow through soil, is to keep the pore space stable for a prolonged time. In natural soils this is particularly difficult for high water saturations because clay minerals cause soil swelling and the typically high water fluxes lead to internal erosion. During drainage, the soil shrinks and the air-

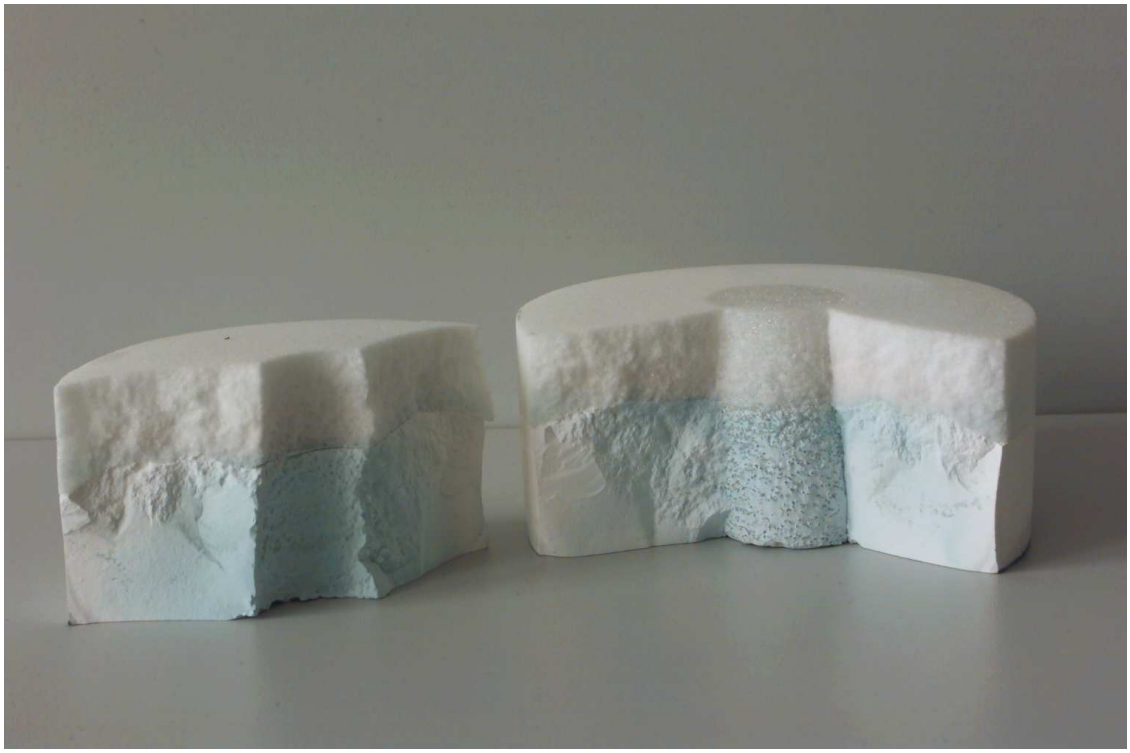

Figure 4.1: Structured porous medium made of sintered glass granules. The sample consists of two annular layers where the bottom layer is fine textured and the top layer has an intermediate pore size. The core in the center is coarse textured. The color is from an experiment with a Brilliant Blue dye tracer which was transported by capillary rise.

flow measurement is obstructed by the by-passing of air at the sample boundaries. In addition, there is always the problem of microbiological growth and associated clogging of soil pores in natural soils (Caputo 2000), which can be prevented by the usage of chemicals such as $AgNO_3$, mercuric chloride, thymol, and other poisons. These solutes though, influence the fluid properties and also have to be taken into account when analyzing the measured data.

Since these processes cannot be suppressed sufficiently in soils, the problems were circumvented altogether by working with columns made of sintered glass: they were rigid by construction, the same sample could be examined several times as structure and texture were constant, and possible precipitates could be removed effectively[1] to have always a homogeneous influence of surface properties (Ustohal et al. 1998). The smooth surface of the glass beads reduced microscale effects which was in agreement with experiments carried out by Dullien et al. (1988).

4.1 Homogeneous Sintered Glass Columns

The investigated columns were made of sintered boron silicate glass by *ROBU Glasfiltergeräte GmbH, Germany*[2]. The chemical composition and some physical properties can be found in Appendix B. The sample size of the cylindrical columns was limited to a maximum height of 120 mm, and a diameter of 50 - 55 mm for technical reasons as during the sintering process all material had to be heated up to melting temperature to allow sintering in the center, while preventing clotting of the glass granules at the boundaries.

The manufacturer provides several pore size classes with almost uniform grain size, which results in a narrow pore size distribution. For construction of heterogeneous structures glass granules of the P16, P100, and P250 classes were for technical reason used as they do not mix before sintering[3].

The study of the influence of the structure of a sample required knowledge of the individual elements building the structure. Although it is possible to get structure information by x-ray tomography of a sample (Vogel et al. 2002) the opposite way was chosen for this study and the structure was sampled from materials with known hydraulic properties. For this purpose, a set of homogeneous columns were prepared and their specific hydraulic properties were examined. Technical data of the columns is shown in Table 4.1.

The porosity measurement was done gravimetrically. The samples were first oven-

[1] After a longer period of no measurement, the saturated conductivity of the columns was lower than measured for the new columns. After cleaning the samples with acetone and hydrochloric acid the original conductivity was measured again.

[2] www.robu.com

[3] The nomenclature is provided by ISO 4793 and refers to the nominal pore diameter.

[4] provided by the manufacturer

sample (dimensions)	porosity [%]	K_{sat} $[cm/h]$	pore diameters $[\mu m]$[4]
P16 (h=*8.9 cm*, $\oslash$=*4.5 cm*)	48±8	0.44	8 - 16
P100 (h=*9.8 cm*, $\oslash$=*5.5 cm*)	43±2	1.8	40 - 100
P250 (h=*9.6 cm*, $\oslash$=*5.5 cm*)	44±4	7.2	160 - 250

Table 4.1: Material properties of the sintered glass columns. Methods used for analyzing are described in text.

dried for 24 hours[5] at a temperature of 150 °C, weighed and afterwards saturated in a desiccator for 24 hours at a pressure of -500 hPa to ensure no residual air in the columns[6]. The errors in porosity values were mainly caused by the volume measurement as the columns had no ideal cylindric shape.

Saturated conductivity, K_{sat}, was measured with the falling head method (Section 3.3). The samples saturated in the desiccator were sealed water- and air-tight at the sides of the cylinders while the bases left open. Additional sealing in the permeameter prohibited any by-passing at the boundaries.

While the porosity was almost the same for the three materials, the hydraulic conductivity increased from P16 to the P250 material due to the increasing pore size.

As pore scale processes were analyzed in a companion study (Schulz 2003), pore scale topology of the glass media was examined by scanning a small subsample of 1 cm^3 by X-ray tomography with a resolution of (15 µm)^3 per voxel. Results for the P100 and P250 media are shown in Figure 4.2. The scanned materials were homogeneous and the measured pore radii met the specifications provided by the manufacturer. The pore structure apparently consisted of pore bodies (large black areas in Figure 4.2) connected by smaller necks. This might have had a strong impact on the pressure saturation relation and especially on hysteresis phenomena as discussed in Section 2.2.4. A closer investigation of the pore geometry of the sintered glass material and its effect on hydraulic properties can be found in Schulz (2003).

A tomographic scan of the whole columns showed an internal porosity gradient in the P250 column, which was due to the sintering technique. At the upper and lower ends of the column porosity was 0.37 where in the center part a value of 0.48 was measured. This effect did not occur in the other columns.

With x-ray tomography it was not possible to scan the texture of the P16 material. This material was fully saturated in all experiments carried out and therefore explicit information about pore geometry or unsaturated hydraulic properties were not relevant for this class.

[5]Drying for another 72 hours had led to no further reduction of weight.

[6]For extraction of air it was better to increase the applied pressure difference than to keep it longer in the desiccator.

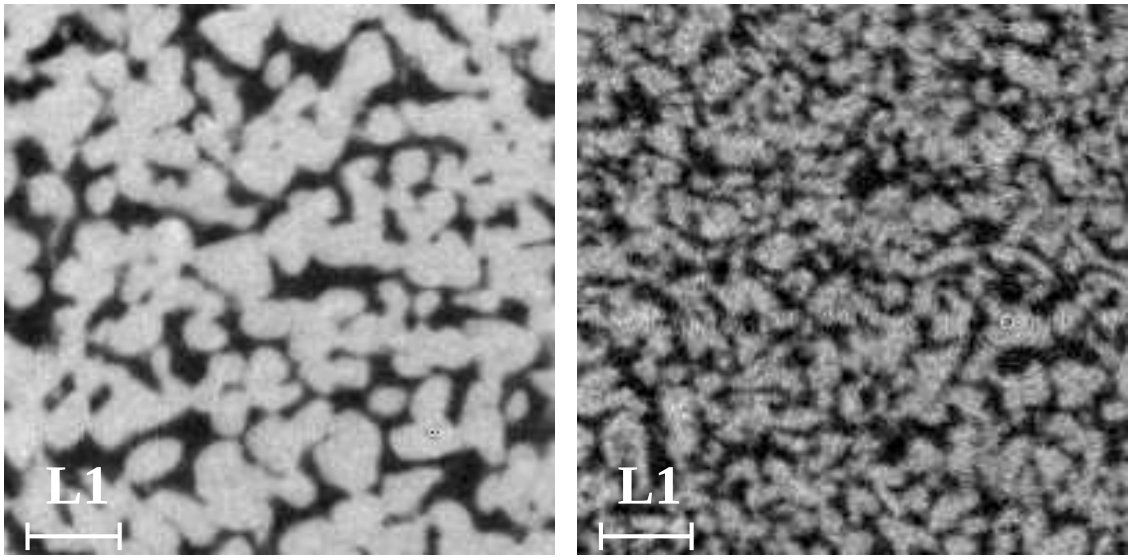

Figure 4.2: X-ray tomograms of the sintered glass media in grey-scale picture (solid: white, void: black). Left: P250 pore size class with pore diameters of 160-250 µm. Right: P100 pore size class with pore diameters of 40-100 µm.

The multistep outflow experiments and evaluation of hydraulic properties which were carried out for two of the homogeneous media, P100 and P250 are presented in the following section. An averaging approach for a composition of a heterogeneous sample consisting of the three materials is shown in Section 4.2. For the heterogeneous sample the simultaneous airflow measurement was also applied.

4.1.1 Homogeneous Glass Column – P250

The multistep outflow experiment for the determination of hydraulic properties of the P250 glass medium was repeated several times during the experimental stage of the setup. Since this experiments were done with different boundary conditions they could be optimized for this sample to improve parameter evaluation.

The column which was wrapped in a PVC tube at the side boundaries was saturated in a desiccator for every single measurement. With the aim of measuring primary drainage curves, they all had to start at full water saturation. As the column drained freely, it was additionally wrapped in a latex casing for the transport from the desiccator to the sample holder. After installing the sample in the water filled sample holder the latex case was removed. Although this procedure was time consuming (and sometimes quite wet) air inclusions in the installed sample were reduced to a minimum. The effect of entrapped air became visible when hydraulic conductivity was reduced noticeably.

The lower boundary pressure scheme which was applied to this sample is shown in Figure 4.3 as a blue dashed line. Due to the large pores and the small width of the pore size distribution the steps started at $8\,\mathrm{cm}_{WC}$ with increments of $-2\,\mathrm{cm}_{WC}$ for each step. Several measurements with this column showed that the sample was almost drained at pressures less than $-10\,\mathrm{cm}_{WC}$, therefore imbibition started at a lower boundary pressure of $-12\,\mathrm{cm}_{WC}$ after a four hour redistribution phase. Duration of imbibition steps was set to eight hours for redistribution in the sample because of the low hydraulic conductivity in the dry range. With this, duration equilibrium was almost reached for the single steps.

The tensiometer developed for the rigid media (Section 3.2.2) was placed at the center of the top of the column. Improvement of hydraulic contact was achieved by use of a layer of gaze and a chuck which fixed the instrument.

Reproducibility of measurements was examined when the experiment was repeated several times. With the described sample preparation procedure initial saturation was assumed constant for all experiments. Experiments with different boundary conditions led to comparable results in the hydraulic functions. For larger steps, compared to the pore size distribution of the medium, the estimations of hydraulic parameters were comparable between separate experiments, a result which was already reported (e.g. Hollenbeck and Jensen 1999). Additionally the measurement was done in a separate setup where only multistep outflow experiments could be carried out. The results of this measurement corresponded to the measurements in the new setup.

Experimental Results

The results of the multistep outflow measurement carried out with the P250 sample at the new setup are shown in Figure 4.3. The outflow curve ($\circ$) showed an air entry point at a lower boundary pressure of $2\,\mathrm{cm}_{WC}$. Subsequent steps had almost the same height, as the water table was drawn through the column until the lower boundary pressure was at $-6\,\mathrm{cm}_{WC}$. At $-12\,\mathrm{cm}_{WC}$ the sample was drained to a residual water content of 12 %. Further reduction of pressure gained no significant increase of water content as measured in separate experiments.

The rewetting of the sample started after a four hour redistribution phase. Since the hydraulic conductivity was low at this saturation, there was no equilibrium within the sample. Therefore the first imbibition steps showed a further increase of outflow until the wetting direction had changed from drainage to imbibition throughout the whole column. Imbibition showed significant hysteresis in the pressure saturation relation, since the water content was almost at its minimum value until a lower boundary pressure of $-4\,\mathrm{cm}_{WC}$ was applied. The sample was imbibed in four steps of almost equal heights which can be interpreted as the advancing wetting front in the column.

After measurement of a complete out- and inflow cycle an air content of 5 % enclosed in the column was measured by weighing the sample before and after re-

saturation in a desiccator.

Hysteresis effects could be explained by the geometry of the pore space (Figure 4.2, left), which apparently corresponded to larger pore bodies connected through narrow necks. The latter, were critical during drainage while the former, were critical during imbibition (Figure 2.7).

Hydraulic Properties

For the evaluation of hydraulic properties the `eshpim` fitting code was preconditioned with all data available from separate experiments. For the rigid medium saturated water content was set to measured porosity. Measured saturated conductivity was set as an initial value and the fitting routine was allowed to adjust this parameter within one order of magnitude up and down. For α_d, α_w, and n, the initial values were evaluated from a static pressure saturation measurement and the initial value of parameter τ was set to 0.5. The hysteresis effect was considered by the *constrained Kool and Parker* model. Results of the inverse parameter estimation are listed in Table 4.2 together with their respective confidence intervals. The calculated

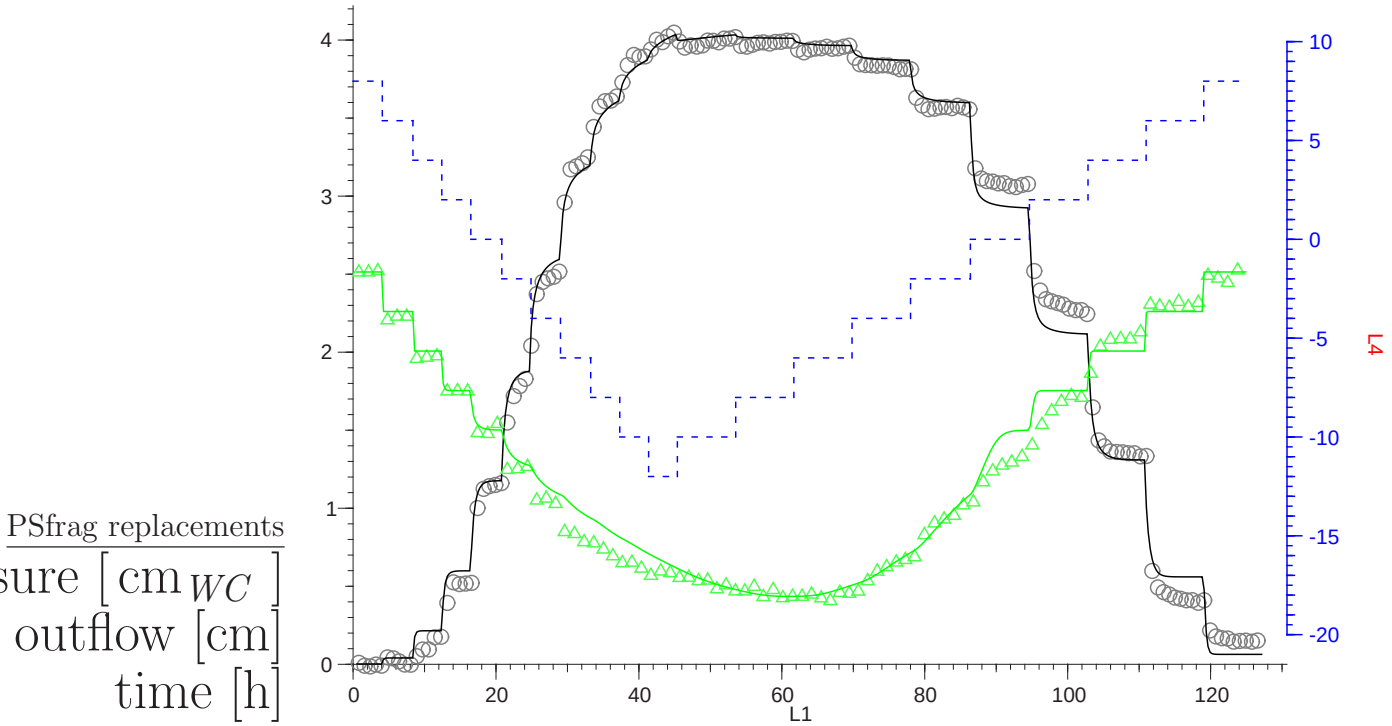

Figure 4.3: Measurement and simulations of hysteretic outflow curve of P250 glass column. Lower boundary pressure (dashed), cumulative outflow (black), and tensiometer potential (green), as measured (symbols) and fitted (solid lines).

covariance matrix did not show any significant correlation between any parameters for this fit.

The simulated outflow curve is shown in Figure 4.3 (solid black line). Irregularities between simulation and measured data in the pressure ranges where the wetting front moves through the column, reflect the porosity gradient in the column which was measured by x-ray tomography. Since simulation had to be done with homogeneous porosity this variation could not be taken into account. Discrepancies between measured tensiometer data and the simulated potential at the upper end of the column was also a result of the porosity gradient within the P250 sample. Since the difference in porosity was a result of the sintering procedure, the pore size distribution changed at the upper end towards smaller pores. As a result, hydraulic conductivity was higher in this part of the sample than estimated by the model which was based on a homogeneous porosity.

The water dynamics at the reversal point was reflected well by the simulation. The outflow curve was decreasing first, because the lower part of the sample was imbibed and then the curve was rising again when that part of the sample was drained where pressure was still lower than the actual pressure.

The resulting hydraulic functions for the P250 column are shown in Figure 4.4 (green lines). The pressure saturation relation (left) and the pressure conductivity relation (right) were calculated with the parameters estimated from the transient experiment for the drainage and imbibition branches of the multistep outflow curve. The steep slope of the pressure saturation relation reflects the narrow pore size distribution of the sintered glass material. Note that the material properties shown in the figure do not reflect the sample height (as they should be independent), i.e. the hydrostatic pressure assigned to the sample height has to be added before the results are compared to measured data.

sample	P250
parameter	
α_d $[cm^{-1}]$	0.429±0.011
n	3.63±0.14
K_{sat} $[cm/h]$	8.8±0.2
θ_s	0.44
θ_r	0.01±0.01
τ	0.61±0.14
α_w $[cm^{-1}]$	0.142±0.002

Table 4.2: Van Genuchten parameters for homogeneous P250 glass sample as estimated with `eshpim` and their respective 95 % confidence interval. The value of θ_s was fixed for simulations to the measured value.

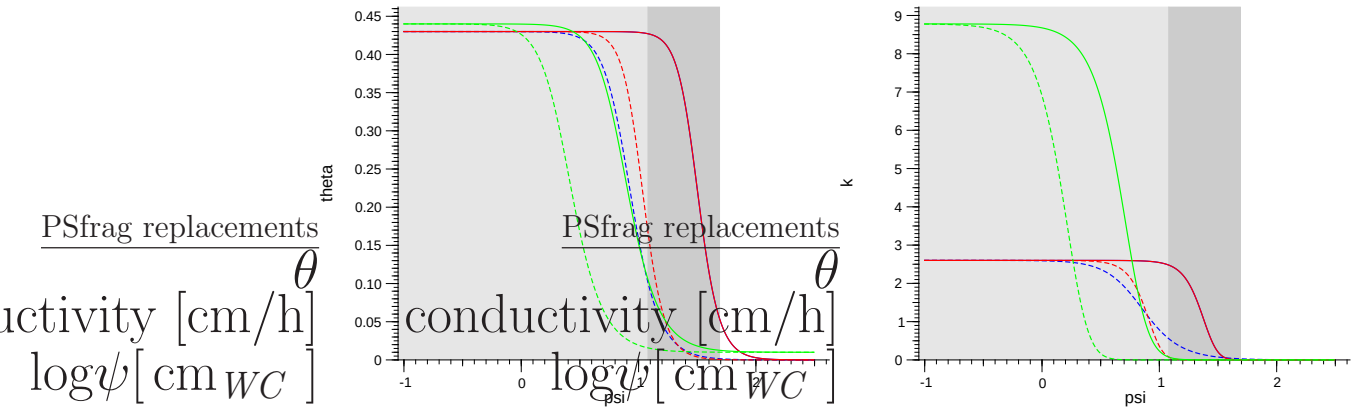

Figure 4.4: Hysteretic hydraulic functions of two homogeneous glass columns P250 (green) and P100 (red) estimated with the *constrained Kool and Parker* model, for both drainage (solid curve) and imbibition (dashed) branches. Separate fit of imbibition branch of the P100 glass (blue). Left: Pressure saturation curve. Right: Pressure conductivity curve. The shaded areas show the range of measurement for the P250 sand (light grey) and P100 (additional dark grey).

4.1.2 Homogeneous Glass Column – P100

The preparation of the P100 sample was almost the same as for the P250 column. The sample was wrapped in a PVC tube and saturated in a desiccator. For this column the problem of free drainage during installation did not occur due to its smaller pores. Lower boundary conditions for the measurement are shown in Figure 4.5. Starting at $1\,\mathrm{cm}_{WC}$, drainage was carried out to a maximum pressure of $-49\,\mathrm{cm}_{WC}$ with a variable duration of steps due to the changing hydraulic conductivity. Although the inverse parameter estimation did not require steady states, the uncertainty of the parameters was decreased when the shape of the outflow curve contained both parts of the system response, the fast rise in the beginning of a new pressure step and the slow redistribution. For imbibition, the heights of the pressure steps were the same, and duration was chosen with respect to the changing hydraulic conductivity.

The external tensiometer was placed in the center on top of the column and fixed with the chuck.

Experimental Results

The measured outflow curve and tensiometer pressure data is shown in Figure 4.5 (symbols). Drainage started at a water potential of $-10\,\mathrm{cm}_{WC}$ which corresponds to the theoretical air entry pressure based on the pore size which was measured in the tomograph. The single outflow steps did not reach equilibrium like in the P250

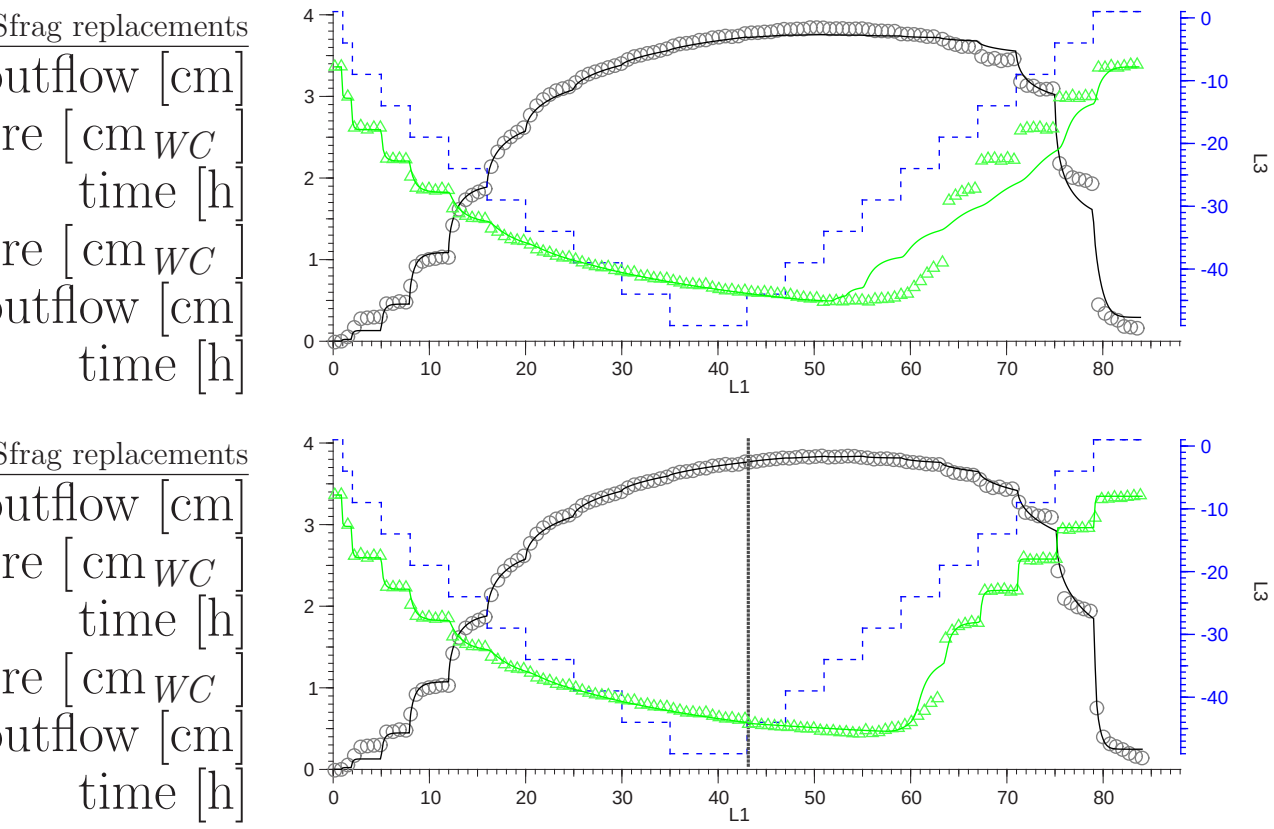

Figure 4.5: Measurement and simulations of the hysteretic outflow curve of the P100 glass column. Lower boundary pressure (dashed), cumulative outflow (○), and tensiometer potential (△), as measured (symbols) and fitted (solid lines). Simulations of the primary drainage and imbibition curves with *constrained Kool and Parker* hysteresis approach (top) and separate sets of parameters for each branch of the curve (bottom).

material. At a pressure of $-49\,\mathrm{cm}_{WC}$ drainage was stopped. After a 4 hour redistribution phase, residual water in the column was 7 %[7]. Due to the low hydraulic conductivity in the dry range the reversal from drainage to imbibition developed very slowly in the column. The cumulative outflow was increasing slightly for another ten hours and the tensiometer pressure was also not responding to the higher pressures. When water was flowing back into the column the tensiometer pressure showed a jump when hydraulic conductivity increased again. The retention relation showed strong hysteresis as the minimum water content was kept to a lower boundary pressure of $-24\,\mathrm{cm}_{WC}$. The main part of resaturation was done during

[7]Since the experiments were repeated several times, it was possible to interrupt the cycles and measure water content between drainage and imbibition.

the last two pressure steps. At the end of the experiment a residual air content of 4 % was measured gravimetrically before and after resaturation of the column in a desiccator. Possibly this amount of air could have been further decreased when the last step would have been lasted longer.

Hydraulic Properties

Parameter estimation for this measurement was done with two different approaches. The fitting results are shown in Figure 4.5 (top) for the *constrained Kool and Parker* model and (bottom) for the *Kool and Parker* model with a full set of parameters for both branches.

Evaluation of the measurement was first done with the *constrained* model which was provided by `eshpim`. To achieve the best agreement of the fit and measured data, the outflow curve was fitted solely and the parameters were fixed. Except of the five hours in the beginning of the experiment where the system did not meet the requirements for the Richards equation this fit described measured data well. The entire cycle was then fitted with the the second α as free parameter for imbibition. The constrained model failed in description of the system during rewetting. Neither the outflow nor the tensiometer data could be fitted by this approach. The results for this parameter estimation are listed in Table 4.3 and the simulations based on this set of parameters are shown in Figure 4.5 (top).

To get more flexibility in the hydraulic functions for both branches of the multistep outflow experiment the fitting of data was split into two separate parts. The outflow branch was fitted with a complete set of parameters to an optimum agreement. Estimation of hydraulic properties was done with a full set of parameters for the imbibition branch of the multistep outflow curve. Simulation results for this

	Kool and Parker (1987)	separate branches	
parameter		drainage	imbibition
α_d $[cm^{-1}]$	0.033	0.033±0.001	
n	5.18	5.18±0.04	4.03±0.09
K_{sat} $[cm/h]$	2.6	2.6±0.1	2.6
θ_s	0.43	0.43	0.43
θ_r	0.00*	0.00 *	0.00 *
τ	0.89	0.89±0.05	−1.96±0.28
α_w	0.097±0.001		0.129±0.001

Table 4.3: Van Genuchten parameters for homogeneous P100 glass sample as estimated with `eshpim` and their respective 95 % confidence intervals. Hysteresis was considered by the *constrained Kool and Parker* model and by separate simulation of each branch of the measured curve. The value of θ_s was fixed for simulations. * Parameter reached limit.

technique are presented in Figure 4.5 (bottom). The thin grey line separates both branches used for fitting. With this method the slow redistribution after reversal from drainage to imbibition was simulated well for the outflow and the tensiometer. The major deviation from measured tensiometer data was the prediction of the jump in the hydraulic conductivity at the tensiometer position after 61 hours which was measured two hours later in the experiment when the next pressure step was started. This deviation could be the result a boundary effect in simulations since the tensiometer was placed at the top of the sample. The outflow curve was also better fitted by this model due to the additional degrees of freedom. The residual air content was slightly overestimated which could be reduced for an experiment which ends at zero potential at the upper boundary to reach starting conditions. Parameters which resulted from this fit are listed in Table 4.3 (right).

Figure 4.4 shows the hydraulic functions for the P100 material. The *constrained Kool and Parker* model is represented by the red lines. The imbibition curves (red, dashed) are parallel to drainage (red, solid) as they were based on the same van Genuchten n parameter. The steep slope of the retention function reflects the narrow pore size distribution of the material which was measured by x-ray tomography. The result of the separate simulation of both branches is the additional imbibition curve (blue, dashed) which has a slope different from the corresponding drainage curve (red, solid). The difference in the slope of this curves, i.e. the different n_d and n_i parameters, could take the different behavior in the drainage and imbibition process into consideration (Section 2.2.6.3). A problem which is suppressed by the constraint is the crossing of the curves which could not be explained on physical principles for the main drainage and imbibition branches (Kool and Parker 1987, Schultze 1998), but this effect did not occur with this material.

4.2 Structured Column

For examination of column scale heterogeneity effects, a fourth column was composed made of the three homogeneous materials, introduced in the previous section. The major part consisted of P100 material where two lenses were embedded. The P250 and P16 materials were used for building the lenses (Figure 4.6, Table 4.1). The lenses were 5 mm flat slices with the same diameter as the whole column. To make a permanent flow in the P100 material possible, a part of the slice was cut-off as shown in the figure. The volume of each lens was 8 % of the sample volume which made the effects of each lens visible without dominating the processes in the column. One reason for this kind of structure was its effect on residual fluid saturations, where the volume had to be large enough to distinguish between structure and texture effects. The lense should offer a compartment for residual water during drainage and the coarse lense should contain the residual air in the imbibition branch of the experiments. For this purpose the column was flattened at both ends and could

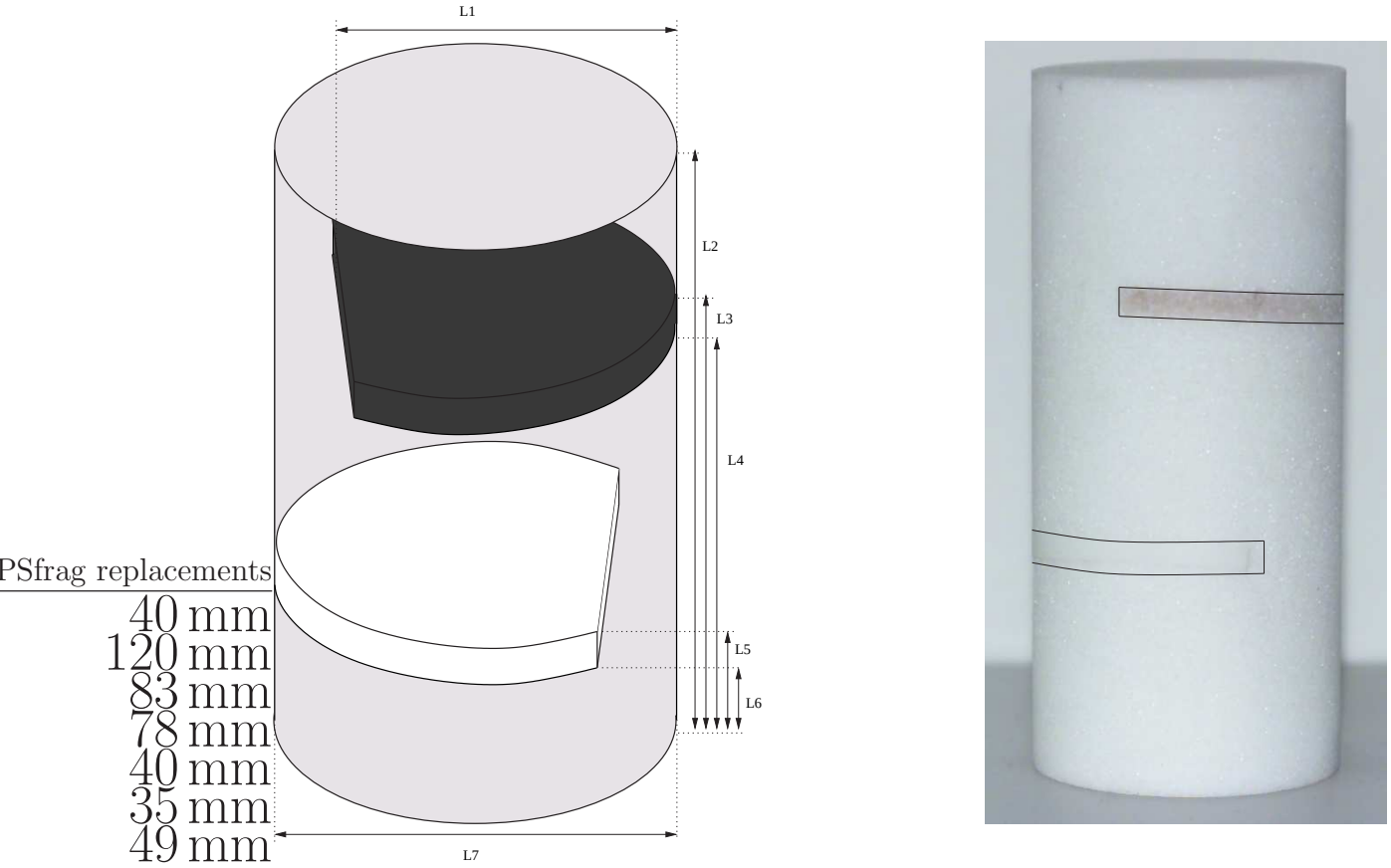

Figure 4.6: Structured sintered glass column. The sample consists of the three materials: P100 (light grey) with two lenses of P250 (black) and P15(white), which are 8 % of the sample volume each.

have been installed with the coarse lens up and with the coarse lens down. Another aspect referred to different flow regimes caused by varying saturations which has an enormous impact on solute transport processes. A comparison of two characteristic cases is presented in Appendix B.3.

For simultaneous measurement of hydraulic and pneumatic properties, the sample was installed with the coarse lens up. The applied lower boundary pressures were similar to the pressures used for the P100 experiment but steps were varied in length as the local equilibrium states were not required. The steps in the beginning of the experiment where the hydraulic conductivity was high lasted for one hour only, whereas the length of the steps was increased in the drier range. The duration of the experiment was optimized with the prior knowledge of the system response provided by the P100 experiment. For resaturation where a low hydraulic conductivity was expected in the beginning the first imbibition steps lasted only two hours but the

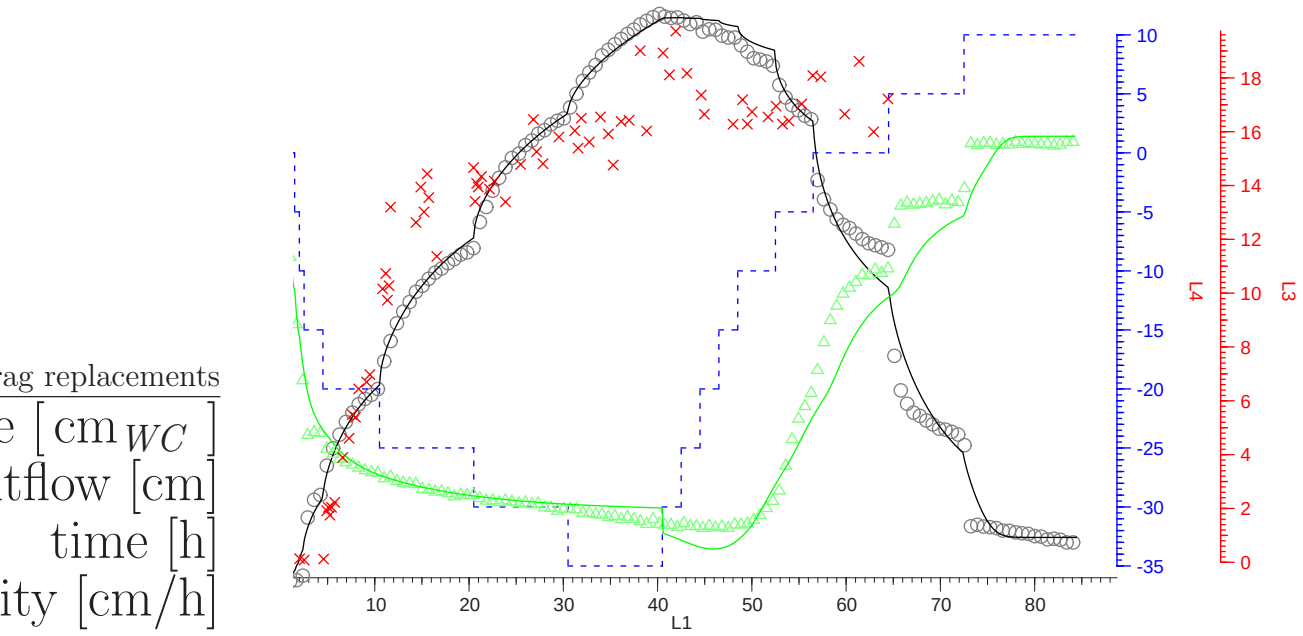

Figure 4.7: Measurement and simulations of hysteretic outflow curve of structured glass column. Lower boundary pressure (dashed), cumulative outflow (○) tensiometer potential (△), and air conductivity (red). Simulation results for outflow and tensiometer curves represented as solid lines in the respective color. The pressure jump of the simulated tensiometer pressure was due to the inconsistency in the parameterization for the two branches.

later steps were held for eight to ten hours. Air-flow measurement was carried out when lower boundary pressure in the water phase was equal to and less than $0\,\mathrm{cm}_{WC}$. The whole pressure scheme applied to this sample is shown in Figure 4.7 as blue dashed line.

Experimental Results

The experimental results for the combined multistep outflow and air-flow measurement are shown in Figure 4.7. The air entry was at a lower boundary pressure of $-10\,\mathrm{cm}_{WC}$ as expected for the P100 material. As a major difference from the P100 material the hydraulic conductivity was lower for this sample, which could be attributed to the hydraulic conductivity of the P16 lens (Table 4.1). The system responded very slowly to the applied pressure changes. The tensiometer did not follow the lower boundary pressures when the $-25\,\mathrm{cm}_{WC}$ step was applied after 10 hours. Although the steps lasted for 10 hours steady states were not nearly reached. After the reversal to imbibition water was flowing back into the column immediately. The retention relation showed hysteresis between the drainage and imbibition branches.

At a lower boundary pressure of $10\,\mathrm{cm}_{WC}$ in the last imbibition step, there was about 9 % of residual air in the sample. This amount of air was assumed to be entrapped in the coarse lense during imbibition. Consequently, hysteresis was observed at two different scales: structural hysteresis as a result of the macroscopic lenses, and textural hysteresis due to the geometry of the pores of the different materials. The air was then removed slightly by continuous air paths from the lens to the atmosphere. The experiment was stopped too early to get the final residual air content. For the measured state the residual air saturation was 6 % which was measured gravimetrically before and after saturation in the desiccator.

At a pressure of $-20\,\mathrm{cm}_{WC}$ air became continuous and the air-flow measurement started. The corresponding water content was 20 %. Air conductivity increased during drainage following the stepwise reduction of water content in the column. At a water content of 8 % the pores which were relevant for air-flow were drained and a further reduction of water content resulted only in a slight increase of air conductivity. The pore water which was drained in the following steps came from small tortuous pores which had little impact on the integral air permeability. In the imbibition branch the maximum air conductivity was held. Extinction of air conductivity could not be measured in this setting as the respective saturation was reached at water potential higher than zero where air conductivity could not be measured anymore.

Hydraulic Properties

For the type of heterogeneity investigated in this experiment it was evident that the structure of the sample played a specific role for the effective hydraulic and pneumatic properties at a larger scale and that simple averaging of properties of homogeneous materials could not be possible.

The simulation of water dynamics of the structured column was based on the prior knowledge of the hydraulic properties of the homogeneous materials. The simulation results presented in Figure 4.7 were a result of a separate fitting of both branches. Since the applied pressure was too low for drainage of the P16 lense, the bimodal van Genuchten model was used for simulations. The material properties, i.e. the α's and n's of the homogeneous materials P100 and P250 were fixed and initial values of the other parameters were set as they were measured in separate experiments. The parameters resulted from the best fit are listed in Table 4.4.

Because of the horizontal structure of the sample, it did not offer best conditions for a bimodal fit. The simulations with a fixed weight of the two materials resulted in an early outflow which was not observed. In the outflow branch the coarse textured material was assumed to be in contact with the air reservoir and therefore drained when the air entry pressure of this material was reached. This problem was reduced when the weight of the two modes was also fitted. The best fitting results were achieved with a weight of 3 % for the volume of the coarse textured material. The saturated hydraulic conductivity, which was also fitted, reached a value comparable

parameter	drainage	imbibition
α_1 $[cm^{-1}]$	0.033	0.129
n_1	5.18	4.03
α_2 $[cm^{-1}]$	0.142	0.429
n_2	3.63	3.63
wi	0.97±0.01	80*
K_{sat} $[cm/h]$	0.33±0.01	0.33
θ_s	0.43	0.43
θ_r	0.00*	0.00*
τ	−0.14±0.06	−1.61±0.13

Table 4.4: Bimodal van Genuchten parameters for heterogeneous glass sample. Material properties of the homogeneous materials were used to simulate heterogeneous structure. Free parameters as estimated with `eshpim` and their respective 95 % confidence intervals. * Parameter reached limit.

to that measured for the P16 material. This was also a result of the horizontal structure where the fine textured lens delimited the conductivity of the sample. With this set of estimated parameters the outflow curve and the tensiometer curve could be fitted with a good agreement.

For simulation of this experiment, the approach of separate fitting of both branches in combination with the bimodal model failed for the imbibition branch. On the one hand, there was the influence of the non-steady state at the reversal point. The change of parameters was done for the whole column and that part of the sample which was still in the drainage process would have required the respective parameters until the reversal was carried out. This led to errors in the saturation distribution in the beginning of the simulations, which were affecting the whole imbibition branch. On the other hand, the horizontal sample structure also had a crucial impact on the simulations of the rewetting branch. Because there was no direct connection to the air reservoir, there was some entrapped air in the coarse lens which was removed very slowly. This type of back emptying was also observed by Mortensen et al. (2001), who explained the slow processes by a flow through single channels, which could not be wetted since the airflow blocked the water. The fitting of the curve resulted in a weight for the coarse material which increased to the upper limit of 20 %. This value could not be related to any measured data and therefore seems to be useless. The estimated parameters are listed in Table 4.4. The hydraulic functions shown in Figure 4.8 show only the drainage branch of the simulations. The bimodal hydraulic functions reflect the two maxima in pore size distribution, as assumed by the model. Compared to the homogeneous P100 column, the impact of the coarse P250 material on the bimodal conductivity function was a decrease in the range from zero to $-15\,\mathrm{cm}_{WC}$ by 25 %.

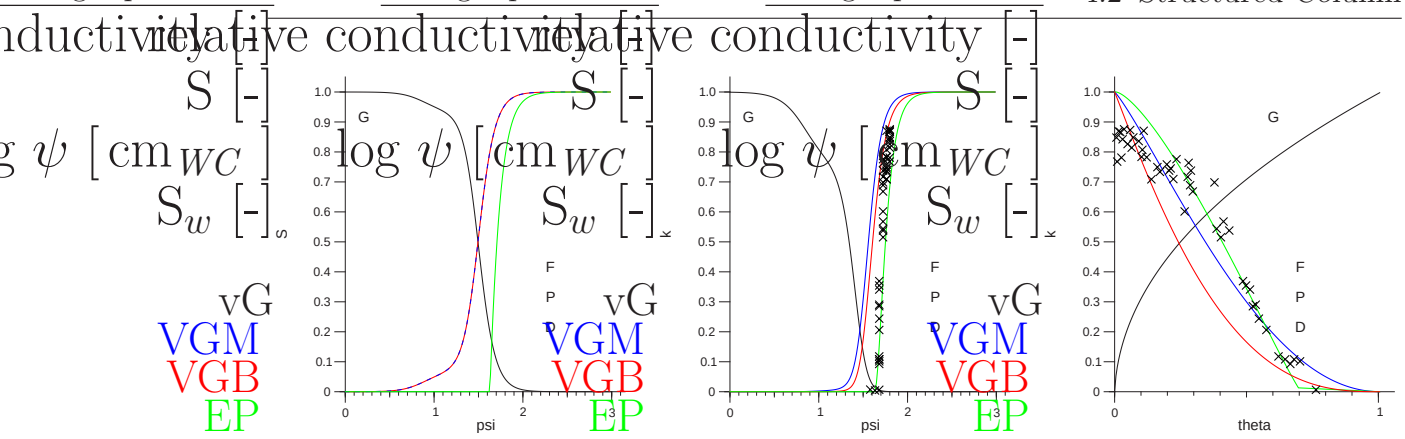

Figure 4.8: Bimodal hydraulic and pneumatic functions for outflow branch of the heterogeneous glass column. Pressure saturation relation for water and air (left) and corresponding pressure conductivity (center) and saturation conductivity relations (right).

Pneumatic Properties

Based on the simulations of the water dynamics for the drainage branch of this experiment, the pneumatic properties were evaluated like introduced in Section 3.6. The temporal evolution of a saturation profile was calculated assuming homogeneous distribution of the two materials involved in drainage. The sample height was resolved in 73 nodes, where the lower six represented the separator plate. Simulated water saturations reflecting the multistep outflow experiment are shown in Figure 4.9 (center) for the nodes within the sample.

Air conductivity was calculated for the discrete nodes of the simulation according to the VGB, VGM, and EP models. For the simulations only hydraulic parameters were used. A comparison of the simulated and measured conductivities is shown in the lower part of Figure 4.9. The VGB and VGM models did not fit measured data very well. Both models assumed that effective air saturation was the pore space complementary to the water saturation (Figure 4.8, left). Beginning with drainage, a nonzero air conductivity was calculated for this models, which was not observed in experimental data. The difference in the rise of air conductivity reflected the different terms for pore size and tortuosity in the conductivity relations (Section 2.3.3). In the VGM model tortuosity is better reflected but the transition from hydraulic to pneumatic properties was still not possible. For the EP model airflow through the sample did not start until the emergence point water content of $\theta_{m,ep} = 12\,\%$ was reached in the single nodes of the simulation. This value was fitted in the simulations to achieve best agreement to measured data. Nodes, where saturation was higher than this emergence point saturation, are marked with a black frame in Figure 4.9 (center). As measured data showed the effect of a spontaneous starting air conductivity, this type of model was most suitable. The stepwise rise of

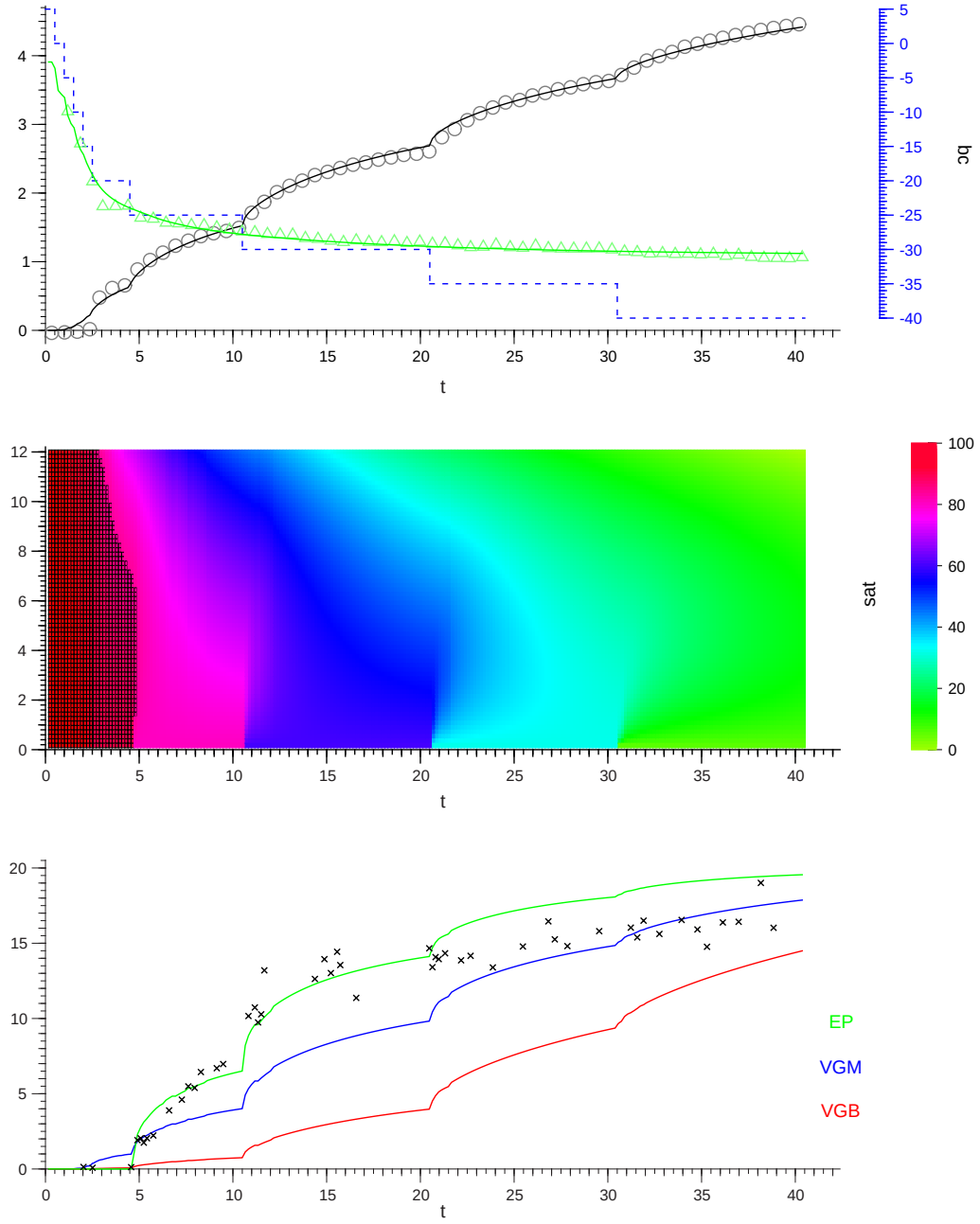

g replacements
flow [cm]
[cm $_{WC}$]
y [cm/h]
time [h]
ight [cm]
VGM
VGB
EP
ation [%]

Figure 4.9: Simulation of air conductivity in structured glass column. Top: Measurement and simulations of hydraulics (outflow branch). Center: Temporal development of saturation in a vertical profile of the sample, based on the P100 material. Bottom: Air conductivity calculated for three air conductivity models. Nodes with saturation more than emergence point saturation are framed black.

air conductivity was predicted well by the model, until the measured data reached its maximum after 21 hours. The overestimation of maximum air conductivity could be attributed to an effect caused by the structure of the sample. The one-dimensional model did not account for the fine P16 lens, which kept saturated during the entire experiment. This lense reduced the cross sectional area which was available for airflow. Continuous air paths could be established only in the P100 material with the small cross sectional area within this layer of the sample.

Figure 4.8 shows the comparison of the hydraulic and pneumatic functions for the used models. The VGM and VGB models were based on an air saturation complementary to water saturation, whereas the EP model showed a sharp rise in the retention function when the emergence point saturation was reached (Figure 4.8, left). In the comparison of the conductivity models with measured data the steep slope of the data could not be predicted by any model in the pressure conductivity relation (center). This could be caused by the discrete water pressure steps which were applied. The saturation conductivity relation was also predicted best by the EP model (right). Both the VGB and VGM models underestimated the air conductivity over a wide range of saturation. The tortuosity exponent gave these curves their specific shape which is different from the shape of the EP model prediction with the tortuosity factor estimated form hydraulic data.

4.3 Discussion

The experiments with homogeneous and heterogeneous sintered glass columns have shown that the multistep outflow technique could be combined with an additional instrument for the determination of pneumatic properties. The measurement of homogeneous samples with the combined setup, resulted in hydraulic properties which were the same as measured in a parallel setup for multistep outflow measurements only.

The influence of structure became visible in the heterogeneous sample. Although the bimodal model should reflect the materials involved in the experiment, it was not possible to predict the whole drainage imbibition cycle. The superposition of the homogeneous hydraulic functions required a direct connection of all compartments to the air and water reservoirs which was not given due to the horizontally layered structure. This seemed to be strongly required especially for the sintered glass materials with the narrow pore size distributions.

As it was possible to simulate the water dynamics for the drainage branch of the multistep outflow experiment, it was possible to simulate the air conductivity with the VGM, VGB, and EP models. A comparison of measured data and simulation results showed a better agreement with the EP model. A rescaling of the effective saturation seemed to be mandatory for the predictions of air conductivity since the simple assumption of an effective air saturation which is complementary to the water

saturation was insufficient.

The rigid sintered glass media had a major advantage during the stage of the development of the experimental device. Experiments were repeated several times always with the same sample. Deviations of experimental results which could not be explained in a physical context, were detected as measurement artifacts and led to improvement of the setup. On the other hand, the rigid material had a major disadvantage at the interface between sample and separator plate. The problem of gaps which made hydraulic contact worse demanded an extremely careful installation of the samples in the sample holder.

5 Two Phase Flow Measurement with repacked Sand Columns

As a second class of materials, sieved repacked sands were examined. With the aim of investigating several structures in the sand, sets of homogenous sands were analyzed in homogeneous packings. With the known properties of the homogeneous materials structured repacked columns were for experimental examination and numerical simulations realized to focus on specific effects caused by the texture of the components and the structure of the samples.

5.1 Characterization of Homogeneous Sands

The base materials for the sand packings were of coarse and fine sand referred to as S-I and S-II, respectively. The sand, sieved and washed, was at spherical shape, as it had originally come from a river. The two grain size classes of the sands and the dimensions of the homogeneous samples are listed in Table 5.1.

Assuming the homogeneity of the sand of separate samples, saturated conductivity was measured with the falling head method in an extra sample of the respective material. Porosity also was calculated via bulk density measurement in separate samples.

sample (dimensions)	porosity [%]	K_{sat} $[cm/h]$	grain size $[\mu m]$
S I (h=*10.0 cm*, $\oslash$=*18.0 cm*)	32±5	200.0	630 - 1250
S II (h=*6.3 cm*, $\oslash$=*16.8 cm*)	38±5	25.0	250 - 630

Table 5.1: Material properties of the homogeneous sand columns. Methods used for analysis are described in text.

5.1.1 Coarse Sand – S-I

Hydraulic properties of the coarse sand S-I were determined in a 28 hour multistep outflow experiment. The lower boundary pressure was selected with respect to the

large pores. The initially saturated column was drained in seven steps with pressures of 0.0, −2.5, −5.0, −7.5, −10.0, −15.0, −20.0 cm $_{WC}$ with the aim of getting almost identical amounts of water in the outflow of each step. The duration of each single step was one hour except the −5.0 cm $_{WC}$ step which lasted for two hours. After a one hour redistribution phase at the end of drainage, the column was resaturated. The duration of each step was increased to 3.3 hours. The applied imbibition pressure steps were identical to the drainage scheme with two additional steps at the end of saturation where pressure was increased to +5.0 cm $_{WC}$ and +10.0 cm $_{WC}$ steps for one hour each, to reach starting conditions.

An internal tensiometer was placed at a height of 8 cm above the lower boundary. This instrument was a 5 cm long ceramic tube, which was in contact with the sample over its whole length, and was not of the type introduced in Section 3.2.2.

Experimental Results

The resulting outflow curve is shown in Figure 5.1. The air entry pressure of this material was reached with the first pressure step. The small step in the outflow curve at 0.5 hours was due to a small irregularity at the lower boundary pressure. The magnetic valve which controlled the pressure had been closed too late and the

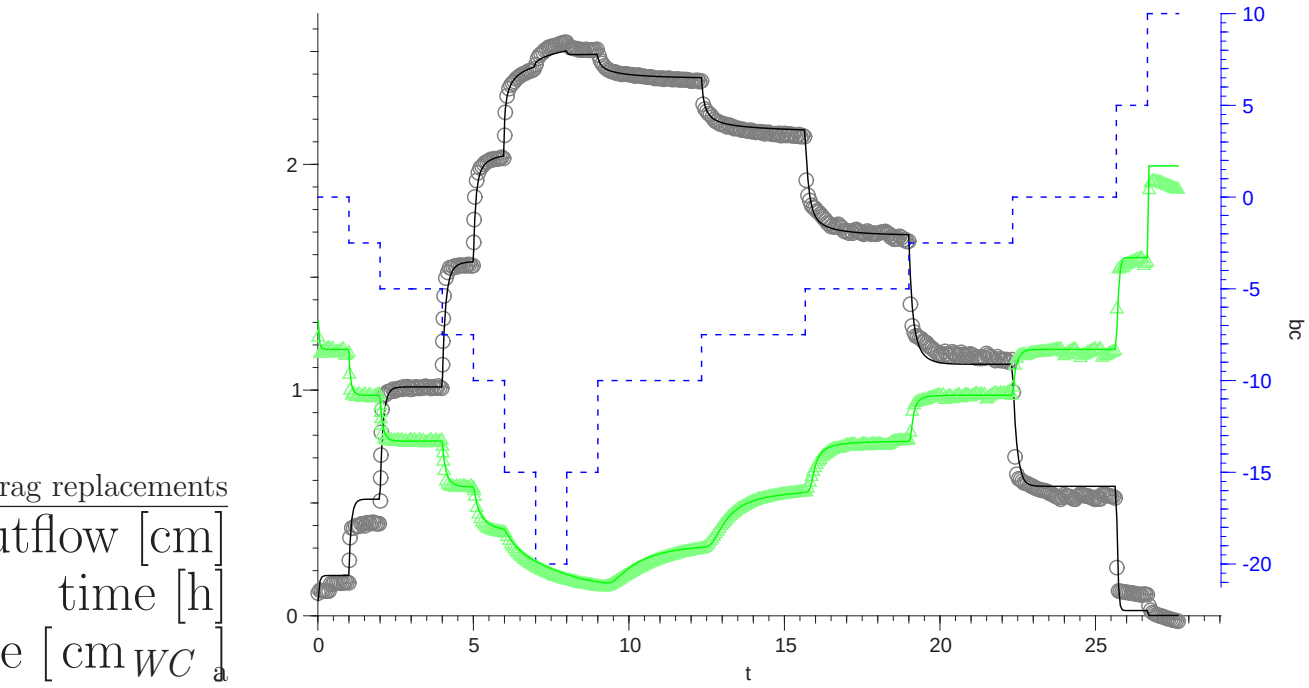

Figure 5.1: Measurement and simulations of hysteretic outflow curve of sand S-I. Lower boundary pressure (dashed), cumulative outflow (black), and tensiometer potential (green), as measured (symbols) and fitted (solid lines).

pressure was $-1\,\mathrm{cm}_{WC}$ for 30 seconds which was enough to drain a specific amount of water from the sample. Due to hysteresis, the water did not flow back to the column when the pressure returned to $0\,\mathrm{cm}_{WC}$ again. The sample had been almost desaturated after the last drainage step. The imbibition branch of the curve showed significant hysteresis in the retention relation since saturation at the $-10.0\,\mathrm{cm}_{WC}$ step was almost the same as at the $-15.0\,\mathrm{cm}_{WC}$ step of drainage. At the pressure of $+10.0\,\mathrm{cm}_{WC}$ the column was completely saturated with water, i.e. there had been no residual air in the sample.

Hydraulic Properties

Figure 5.1 also shows the results of simulated curves for the outflow and tensiometer potential, fitted with the *constrained Kool and Parker* model implemented in `eshpim`. All information about material parameters which were measured separately was used for preconditioning the parameter estimation. The saturated water content had been fixed to the measured value and the initial value used for saturated conductivity was that measured with the falling head method while the fitting routine was allowed to adjust this parameter within one order of magnitude up and down. Initial values of the other parameters were varied for several simulations within physically usefully ranges. Estimated parameters are listed in Table 5.2 together with their 95 % confidence interval. The parameters were estimated with different starting conditions to reduce the possibility of hitting a local minimum for the parameter optimization. All simulations led to results which were similar within their confidence intervals and a global minimum for parameter identification was assumed. Statistical analysis resulted in no significant correlation of parameters.

The model was not able to predict the cumulative outflow of the first two drainage steps. Especially in the wet range and for the homogeneous material with the narrow

sample	S-I
parameter	
α_d $[cm^{-1}]$	0.105±0.001
n	6.76±0.09
K_{sat} $[cm/h]$	156.1±9.0
θ_s	0.28
θ_r	0.011±0.001
τ	0.998±0.052
α_w	0.078±0.001

Table 5.2: Van Genuchten parameters for homogeneous S-I sand sample as estimated with `eshpim` and their respective 95 % confidence interval. The value of θ_s was fixed for simulations to the measured value.

pore size range the van Genuchten model could not reproduce the sharp air entry with the resulting abrupt rise of the cumulative outflow curve (Vogel et al. 2001). Although the tensiometer simulations fitted the measured data well, measured outflow was less than the model prediction. Beginning with the third step measured data was fitted well by the model. At maximum pressure, the model predicts outflow which is less than measured. This was also a result of model errors in the dry range.

During imbibition, dynamic effects were observed beginning with the $-8\,\mathrm{cm}_{WC}$ step to the end of the experiment. When a new pressure step had begun there was a fast decrease of the outflow curve followed by a slow almost linear period. This linear part was due to reduced conductivity by entrapped air. During the following redistribution, air was removed from the sample and the dynamics could be described by the simulations which fitted the measured data again.

Hydraulic functions for the fitted van Genuchten parameters are shown in Figure 5.2 (green lines) for both branches of the hysteretic curve.

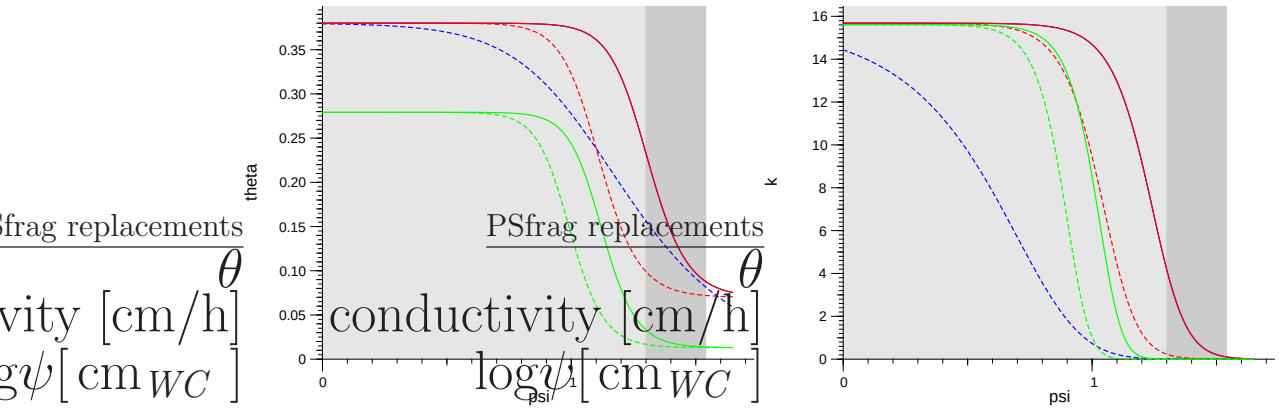

Figure 5.2: Hysteretic hydraulic functions of two homogeneous sands S-I (green) and S-II estimated with the *constrained Kool and Parker* model (red), for both drainage (solid curve) and imbibition (dashed) branches. Separate fit of the imbibition branch of S-II sand (blue). Left: Pressure saturation curve. Right: Pressure conductivity curve. For better comparison the hydraulic conductivity of S-I sand is scaled down by a factor of 10 ($K_{sat} = 156.10\,cm/h$). The shaded areas show the range of measurement for the S-I sand (light grey) and S-II (additional dark grey).

5.1.2 Fine Sand – S-II

With the homogeneous S-II sand the effects of hysteresis on the hydraulic and simultaneously on the pneumatic properties in a multistep outflow experiment were

analyzed. The measurement was started at full water saturation. The tensiometer was placed in the middle of the sample 1.5 cm above the lower boundary. Air-flow measurements were carried out at four positions on each outflow step, the first point at the outflow phase of the step, the second and third during redistribution and the fourth point of measurement was carried out before switching to the next pressure step. After the primary drainage and imbibition cycle two additional scanning cycles were measured to investigate hysteresis effects on the water phase and on the gaseous phase where the emergence and extinction point saturation could also show hysteresis effects.

Experimental Results

The lower boundary condition, measured tensiometer potential, cumulative outflow curve and air conductivity measurements are shown in Figure 5.3. The first cycle had a duration of 152 hours, followed by the first scanning loop from 152-217 hours and

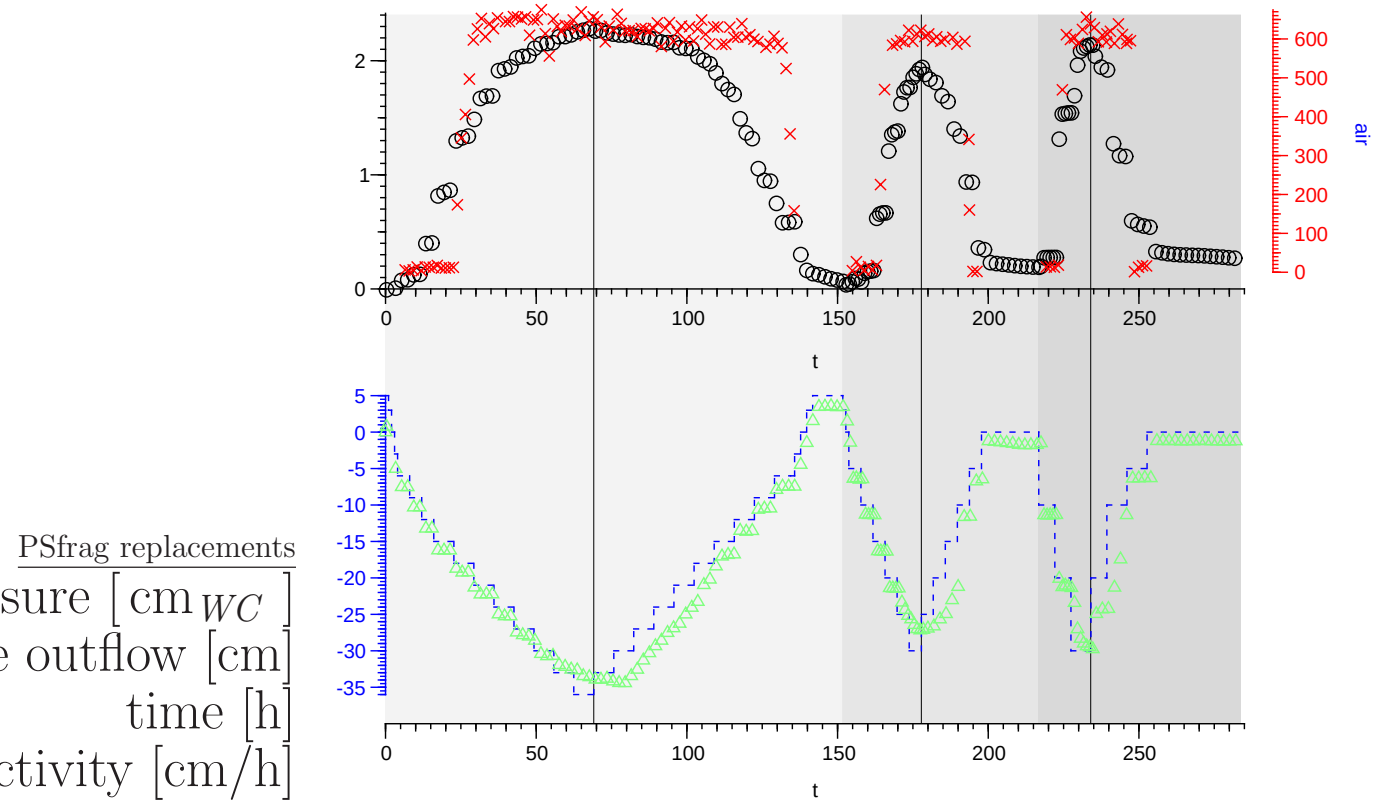

Figure 5.3: Multistep outflow with simultaneous air-flow measurement for sand S-II. Top: Cumulative outflow (grey) and air conductivity (red). Bottom: Predefined lower boundary pressure (blue, dashed) and measured tensiometer potential (green).

a second scanning cycle 217-282 hours. The outflow curve shows pressure saturation hysteresis for the imbibition branch which had been enlarged during the scanning cycles. Residual air content at the end of each cycle had also slightly increased due to the fact that initial pressure was not reached.

For all three cycles there was a clear emergence and extinction of air permeability. Air-flow began when the gaseous phase was continuous along the sample at a water content of 16 % which was the integral value for the sample without consideration of the internal saturation gradient due to the sample height. The macroscopic extinction point in the primary imbibition curve was measured at a water content of 28 % measured in a separate experiment which was started at full air saturation. The scanning cycles reproduced the respective saturation where the emergence point water content varied between 16-26 % and the extinction point water content was between 22-30 %.

Because of the vertical arrangement of sample and separator there was always the effect of a saturation gradient within the column due to gravity. For this reason the measured saturations had to be seen as effective saturations over the full height (6.3 cm) of the sample. A detailed analysis of air conductivity will follow later in this Section.

Hydraulic properties

Estimation of the hydraulic properties of the S-II sand had been made with the same preconditions used for the homogeneous S-I sand. The saturated water content was fixed to the measured value and and saturated conductivity was fitted within one order of magnitude up and down the measured value. Figure 5.4 (top) shows the simulation results for the primary drainage/imbibition cycle using the *constrained*

	constrained	separate branches	
parameter		drainage	imbibition
α_d $[cm^{-1}]$	0.052±0.001	0.055±0.001	
n	5.88	5.88±0.13	3.01±0.19
K_{sat} $[cm/h]$	15.7	15.7±5.2	15.7
θ_s	0.38	0.38	0.38
θ_r	0.01±0.01	0.07±0.01	0.03±0.01
τ	0.79	0.79±0.18	2.12±0.10
α_w	0.081±0.002		0.082±0.001

Table 5.3: Van Genuchten parameters for homogeneous S-II sample as estimated with `eshpim` and their respective 95 % confidence intervals. Hysteresis was considered by the *constrained Kool and Parker* model and by separate simulation of each branch of the measured curve. The value of θ_s was fixed for simulations.

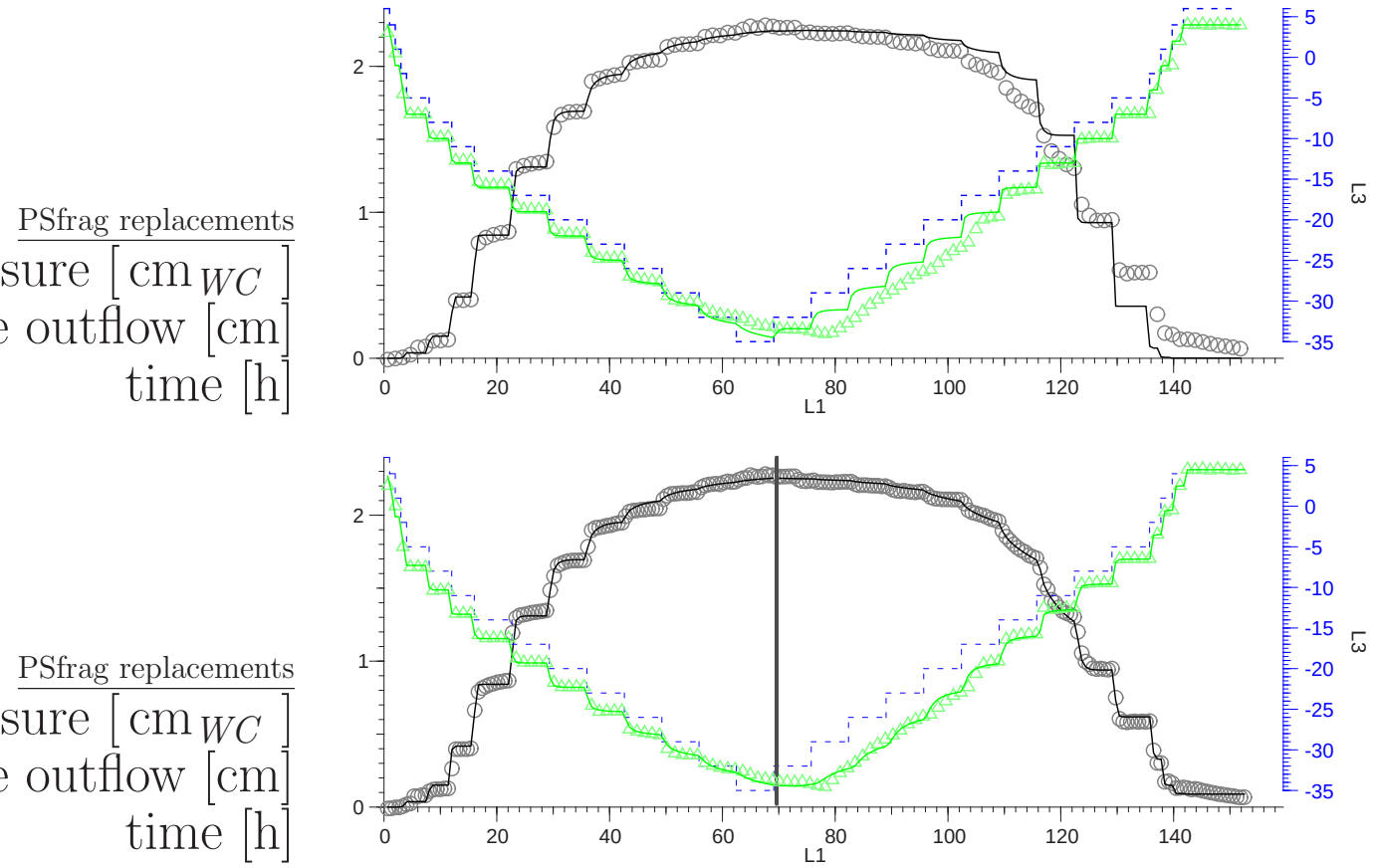

Figure 5.4: Simulations of the primary drainage and imbibition curves with *constrained Kool and Parker* hysteresis approach (top) and separate sets of parameters for each branch of the curve (bottom).

Kool and Parker approach for hysteresis. As it was not possible to fit the entire curve, a fit of the outflow branch was the basis of the simulation shown in the figure. Outflow parameters were fixed and the α for imbibition was fitted to maximum agreement.

For this material, the more flexible functions of both branches were necessary with respect to the evaluation of the scanning cycles. The result for the separate evaluation of both branches of the first cycle is shown in Figure 5.4 (bottom). With this model the experiment could be described well. The outflow curve and the tensiometer pressures were predicted by the simulations in good agreement with the measured data. The van Genuchten parameters resulting from this simulations are listed in Table 5.3. The resulting hydraulic functions are also shown in Figure 5.2 (constrained: red lines, separate fitting: blue lines).

Pneumatic Properties

The measurement of pneumatic conductivity was compared with the three air conductivity models discussed in Section 2.3.4. Figure 5.5 (left) shows the saturations of the two phases as they were used for the prediction models. The water retention curve (black) is shown in the figure as to visualize the dependence of air saturation. The VGM and VGB models were based on the same air saturation curves, where air occupies the pore space complementary to water. For the EP model, effective air saturation had been zero till air continuity was reached at the emergence point saturation which was reached at a lower boundary pressure of $-15\,\mathrm{cm}_{WC}$. Resultant pressure conductivity relations for the three models are presented in Figure 5.5 (center). Because of the additional degree of freedom of the EP model, it fitted measured data best but the slope of the measured curve was much steeper than the model predicts which might have been caused by the discrete pressure steps. Hysteresis of air conductivity was reflected by all three models. Deviations became more obvious in the linear saturation conductivity relation (right). The air conductivity data showed strong hysteresis, which was predicted only slightly by the models. The best fit was achieved for the EP model with a rescaling of both, the emergence point water saturation, which replaces the maximum saturation in the VGM model, and the residual saturation. The dotted lines in the figure show a simulation of air conductivity with $S_{w,e} = 0.8$ and $S_{w,r} = 0.7$ for the drainage and $S_{w,e} = 0.5$ and $S_{w,r} = 0.4$ for the imbibition branch. With the replacement of the residual water saturation the effect of a constant maximum air conductivity,

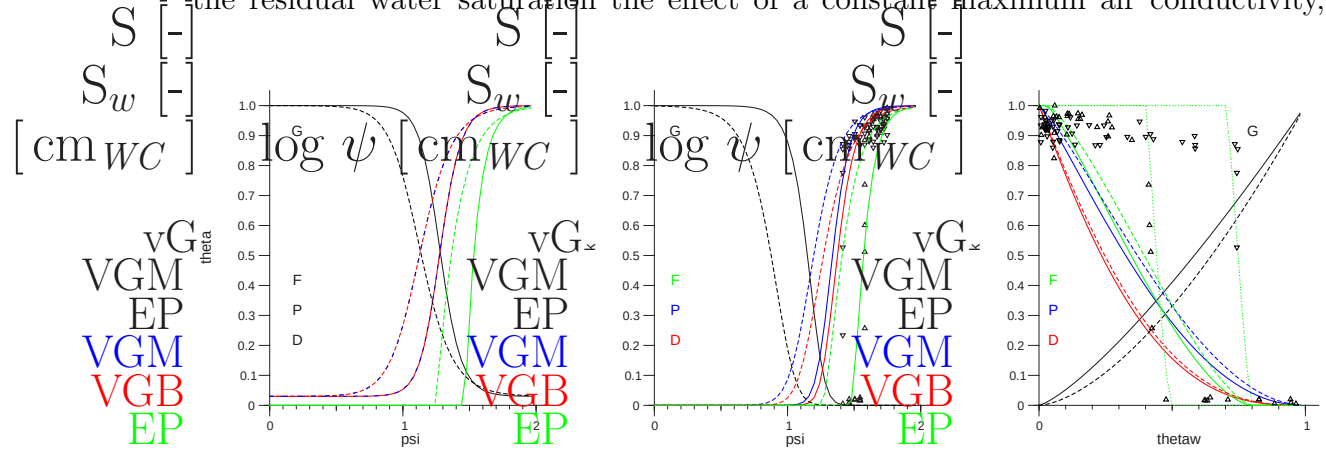

Figure 5.5: Hysteretic pressure saturation relation (left), pressure-conductivity (center) and saturation-conductivity functions (right) for water and air. The VGM and VGB models are based on the same pressure air saturation relation. The EP model calculates an effective air saturation which depends on the emergence point saturation. Experimental data measured in sample S-II with drainage (△) and imbibition (▽) branch of the primary drainage curve.

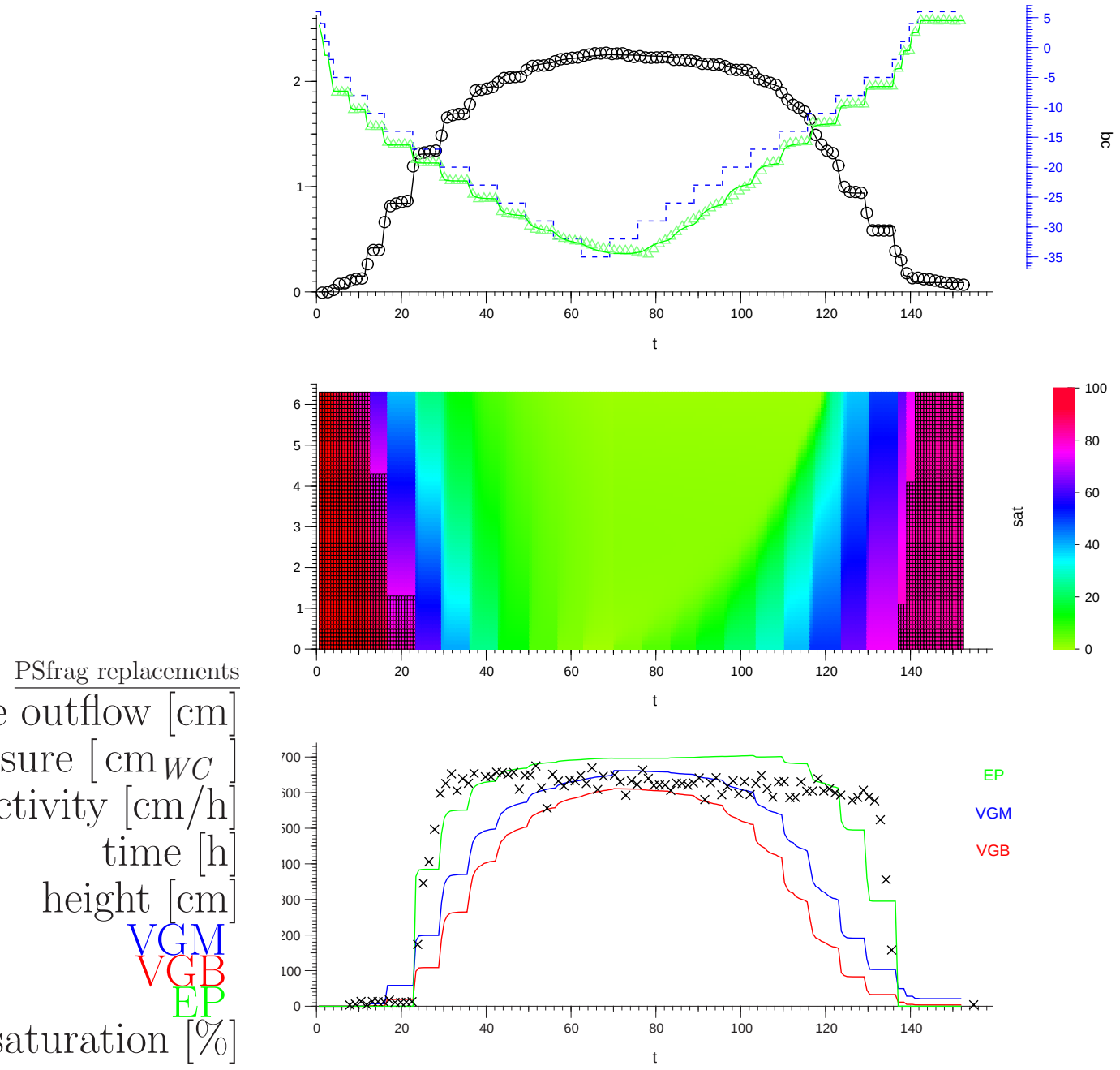

Figure 5.6: Simulation of air conductivity in S-II sand column. Top: Measurement and simulations of hydraulics. Center: Temporal development of saturation in a vertical profile of the sample. Bottom: Air conductivity calculated for three air conductivity models. Nodes with saturation more than emergence point saturation are framed black.

measured in the experiment, could be considered in the macroscopic view of these simulations.

The effect of a vertical saturation gradient due to the influence of gravity was taken into account when using the discrete evaluation method for air conductivity introduced in Section 3.6. Development of saturation in a one-dimensional vertical section of the sand column is shown in Figure 5.6 (center). All model predictions were based on the hydraulic properties evaluated from the multistep outflow experiment. The VGM and VGB models were not able to describe the data as they used a continuous smooth saturation function, which was complementary to water saturation. The EP model, which was calculated with the rescaled effective continuous air saturation had best described the measurement due to its additional degree of freedom. Emergence point water saturation was set to 0.80 for this simulation which was an absolute water content of 30 %. Effective air saturation during drainage was represented well by the model, therefore the rise of air conductivity could be described. Loss of air continuity in the imbibition branch had been much faster than predicted by all models. Although the EP model was able to describe the end of air-flow through the column, the detailed course of the decreasing air conductivity curve had not been described. In Figure 5.6 the nodes with water saturation higher than emergence point saturation are framed in black. One framed node in the profile means that there was no possibility for air to pass the column, i.e. air conductivity had not been measured.

Hysteresis in Hydraulic and Pneumatic Properties Observed in the Additional Scanning Cycles

The simulation of water dynamics was done for the scanning cycles in the same way as for the first cycle. The two drainage and imbibition cycles were simulated with the *constrained Kool and Parker* model. With this model it was not possible

parameter	first D	first I	second D	second I
$\alpha_d[cm^{-1}]$	0.049±0.000	0.075±0.001	0.048±0.001	0.081±0.001
n	5.55±0.17	3.72±0.23	5.15±0.38	3.23±0.20
K_{sat} $[cm/h]$	15.7	15.7	15.7	15.7
θ_s	0.38	0.38	0.38	0.38
θ_r	0.01±0.01	0.01±0.01	0.01±0.01	0.01±0.01
τ	0.84±0.26	0.15±0.54	1.07±0.28	0.95±0.34

Table 5.4: Van Genuchten parameters for the scanning cycles in homogeneous S-II sample as estimated with `eshpim` and their respective 95 % confidence intervals. Each branch of the curve had been evaluated by separate simulations of the measured curve. The value of θ_s was fixed for simulations. * Parameter reached limit. D: drainage, I: Imbibition

to fit the measured data. The simulations by sections, where each simulation was started with the initial pressure and saturation distribution simulated in the former branch resulted in better agreement between measurement and fit. For the estimations the initial parameters had been chosen with the prior knowledge of the main branches. The saturated hydraulic conductivity was fixed to the value estimated by the primary drainage branch and saturated water content was fixed to the measured porosity.

Based on this preconditions, the scanning cycles were analyzed with a complete set of parameters for each branch of the curve. The fitted parameters are listed in Table 5.4 while the resulting hydraulic functions are shown in Figure 5.7. The additional drainage branches resulted in retention curves similar to the primary curve. Since the sample was almost resaturated after the first drainage/imbibition cycle, the parameters should not differ significantly. In the additional imbibition branches there were only slight differences in the estimated parameters. The different pressure schemes applied during the scanning cycles had nearly no influence on the parameter estimation. The resulting parameters estimated for the second scanning cycle were within the margin of the errors of parameters for the first scanning cycle although they differed in the number of pressure steps.

The increase of air entrapment after the cycles did not affect the air conductivity measurement. The emergence point water content which was 16 % in the first cycle, depended on the applied lower boundary water pressures and the resulting outflow of water. In the first scanning cycle the measured value was 15 % and in the second 25 % which was due to the large pressure step after 216 hours. The extinction point water saturation also depended on the lower boundary pressure scheme. In the primary cycle a water content of 28 % was measured, which was 23 % in the first and 30 % in the second scanning cycle due to the respective responses to the boundary condition.

The measured air conductivity - saturation relation did not differ significantly in the three cycles, which made a detailed analysis of the scanning cycles not necessary. The maximum value was the same for all cycles and corresponded to the value measured in the oven dry sand.

The analysis of hysteretic air flow behavior during the scanning cycles would have required lower boundary conditions where the impact on both phases had been considered. For hydraulic purposes the steps should have varied in height and length and for comparison of pneumatic measurements the lower boundary pressure scheme should have been the same. A compromise could have been made by different pressure schemes which should have been repeated to see the effects on both phases.

PSfrag replacements

PSfrag replacements

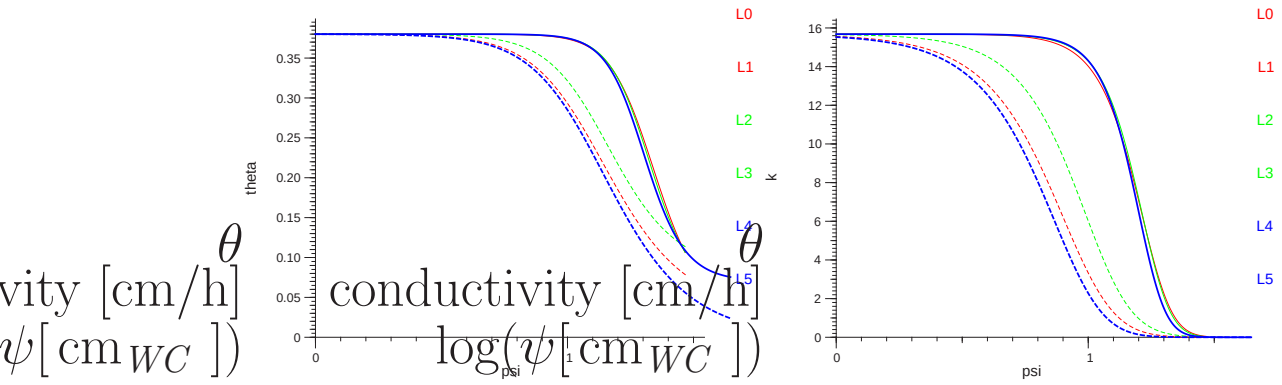

Figure 5.7: Hysteresis in the hydraulic functions of the homogeneous sand S-II measured in a primary (blue) and two additional scanning cycles (first: green, second: red). Data evaluation was done by separate fitting of single branches (drainage: solid lines, imbibition: dashed). Left: Pressure saturation curve. Right: Pressure conductivity curve.

5.2 Structured Sand Columns

Besides the influence of texture on the hydraulic and pneumatic properties there is also an impact of large scale heterogeneities made by the objects building up a porous sample. For examination of the influence of structure within the samples two different sand packings were realized. The influence of "preferential air paths" was tested with the vertically structured column S-H-I which is sketched in Figure 5.8. The horizontally structured column S-H-II was designed to show the effect of "large scale air entrapment". A sketch of this column is given in Figure 5.11.

For examination of the primary drainage curves, a measurement was always began with saturated columns. For this purpose the single structure elements had to be saturated first and then merged to their resulting structure. This was done by saturating the elements consisting of the S-I sand then cooling them down quickly to a temperature less than $-20\,℃$ with dry ice. The fixed elements were shaped and placed in the water saturated S-II sand which had successively been built around the structure elements to ensure full water saturation in the entire column. After setting up the structure the sample was left for 24 hours for thawing and thermal equilibration. Sinking effects due to thawing of the sample were not detected.

sample (dimensions)	porosity [%]	K_{sat} [cm/h]	Ingredients (S-I; S-II)
S-H-I(h=8.0 cm, ⌀=16.8 cm)	38±5	120	97 %; 3 %
S-H-II(h=6.3 cm, ⌀=16.8 cm)	39±5	20	84 %; 16 %

Table 5.5: Material properties of the heterogeneous sand columns.

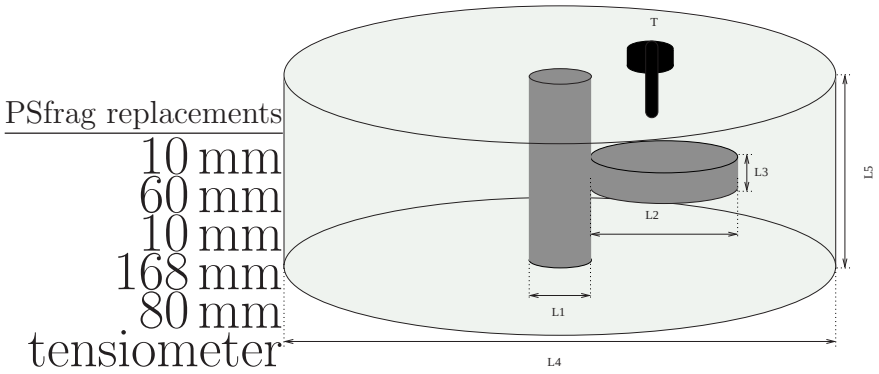

Figure 5.8: Packed sand with predefined structure – S-H-I. The major part (97 Vol. %) consists of sand S-II (light grey) with a "preferential air path" and an inclusion consisting of sand S-I (dark grey). The tensiometer is placed above the S-I sand lens.

5.2.1 Vertically Structured Sand Packing – S-H-I

With the method of vertical air-flow measurement the influence of continuous structure elements in vertical direction could be observed in heterogeneous samples. For this purpose, the structured column, S-H-I, was built which consisted mainly of the S-II sand (97 %) with a vertical cylinder (1 cm in diameter) consisting of the S-I sand, which is placed in the center of the column. An additional S-I lens was placed at one side of the column for the additional effects of a "macroscopic dead end". The large coarse textured core should simulate the effect of macropores which are often found in natural soil. The tensiometer was placed one centimeter below the upper boundary above the coarse lens. Geometric details are shown in Figure 5.8.

Considering the material properties of the homogeneous sands the boundary conditions for this experiment were chosen with the aim of draining the core immediately. The lens should be drained next and then the S-II sand should be drained. The applied pressure scheme is shown in Figure 5.9.

Experimental Results

The results of the multistep outflow measurement are shown in Figure 5.9. Air entry pressure had been reached within the first pressure step of $-5\,\mathrm{cm}_{WC}$ as expected for the S-I sand. In the second and third drainage step outflow was very slow although tension at the tensiometer followed the lower boundary pressure immediately. This effect was caused by the dead end position of the coarse lens, which was drained through the S-II sand because the core was already drained. At a lower boundary pressure of $-45\,\mathrm{cm}_{WC}$ the sample was almost dry. The saturation of the reversal point was kept at its maximum value until the lower boundary pressure had become $-15\,\mathrm{cm}_{WC}$. At the end of the measurement there was about 10 % of residual air in

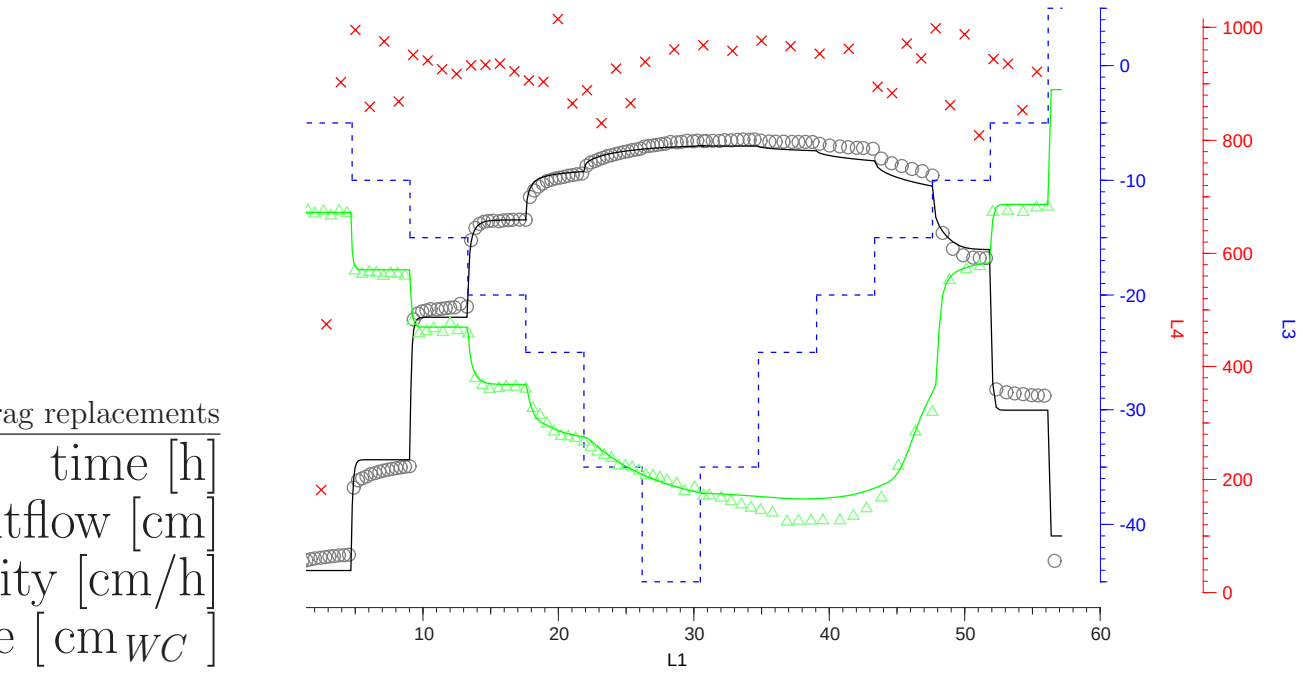

Figure 5.9: Multistep outflow measurement results for structured sand S-H-I. Outflow curve (symbols), lower boundary pressure (blue, dashed), tensiometer potential (green), and air conductivity (red) measurements. The solid lines represent fitted simulation results for outflow and tensiometer curves.

the sample, which could be related to textural effects and additionally to the coarse textured structure elements, especially the dead end lens which was enclosed during the last imbibition step.

With drainage of the vertical cylinder, a continuous air path through the column had been opened and air conductivity increased to its maximum value within one hour in the redistribution phase of the $-5\,\mathrm{cm}_{WC}$ pressure step. The maximum value was kept during the whole experiment. The extinction of air conductivity could not be measured, because the air-flow measurement had to be stopped at a lower boundary pressure of $\pm 0\,\mathrm{cm}_{WC}$ to ensure phase separation. At this pressure the coarse textured S-I sand had not yet been saturated, i.e. only a closed water table would have stopped vertical air-flow through the sample.

Hydraulic properties

For this kind of pathologic structure evaluation needed a combination of separate fitting of both branches of the measurement and the more flexible mulitmodal hydraulic functions. Because of the vertical structure the system had been ideally conditioned for a bimodal model, as two materials were involved, they were vertically arranged,

and both were directly connected to the water and air reservoirs.

The fitting routine in `eshpim` only allowed the adjustment of saturated conductivity, residual water content and tortuosity. The other parameters were fixed to the values estimated for the homogeneous materials. The parameters for the entire primary drainage/imbibition cycle resulting from this evaluation are shown in Table 5.6. The fitted outflow and tensiometer potential curve is also presented in Figure 5.9 (solid lines). The simulation results showed good correspondence to the measurement in the outflow curve because this setting of the column offered the best conditions for the use of this type of simulation. In the imbibition branch of the simulated curve correspondence to measured data was still good. Residual air had been overestimated by the model but this was a result of the specific sample geometry. The S-I sand cylinder in the middle of the sample offered a central air conduit. Air from the S-II sand could be removed efficiently via this path over the whole height of the column until it was saturated in the last pressure step. In this context a good fitting result always have to consider the fact that the α's and n's were fixed to values estimated from separate experiments.

Pneumatic Properties

For this type of structure, the concepts of air conductivity models discussed in Section 2.3.4 did not work. Figure 5.10 shows the application of the models with the same preconditions used for the S-II sand column (Section 5.1.2) as solid and dashed lines for drainage and imbibition, respectively. Water saturation was represented by the bimodal hydraulic functions with the 97 % weight for the S-II sand. Air

parameter	drainage	imbibition
α_1 $[cm^{-1}]$	0.052	0.082
n_1	5.88	3.15
α_2 $[cm^{-1}]$	0.078	0.142
n_2	6.76	6.76
weight 1:2	0.97	0.97
K_{sat} $[cm/h]$	118.5±0.6	118.5
θ_s	0.38	0.38
θ_r	0.09±0.01	0.05±0.01
τ	0.70±0.15	1.92±0.02

Table 5.6: Van Genuchten parameters of heterogeneous S-H-I sample as estimated with `eshpim` and their respective 95 % confidence intervals. Two involved materials were taken into account by bimodal hydraulic functions. Hysteresis was considered by separate simulation of drainage and imbibition branch of the measured curve. The value of θ_s, and the weight of the two modes of hydraulic functions were fixed for simulations.

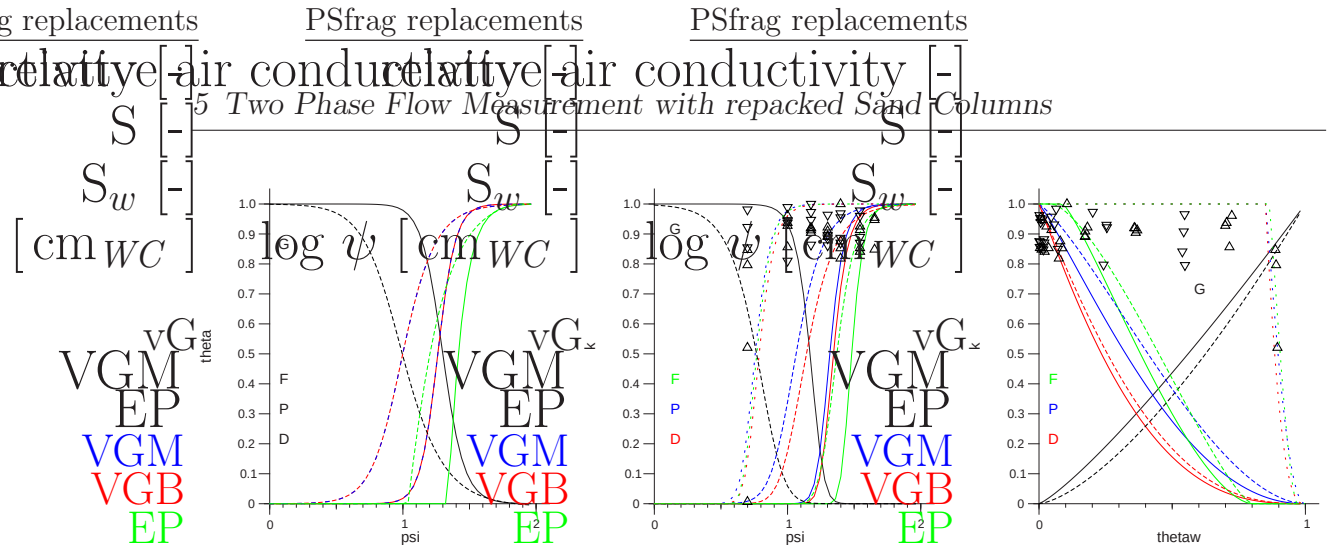

Figure 5.10: Comparison of different air conductivity models and data measured in heterogeneous column S-H-I. Pressure saturation relation for water and air (left). The hysteretic pressure air-conductivity (center) and saturation air-conductivity (right) functions measured in sample S-II with drainage (measured: △, modeled: solid) and imbibition (measured: ▽, modeled: dashed) branch of the primary drainage curve. Bimodal modeling was compared to an unimodal model based on the S-I sand (dotted).

conductivity had been calculated with the effective saturations and the bimodal functions for the three models. The models had predicted a slow increase of air conductivity which was in contrast with measured data.

The direct evaluation of the measured macroscopic data was improved, when the sample was divided in two distinct pore systems. The S-II sand which had almost no influence on the air conductivity measurement and the S-I sand which could have been seen as a macropore system. Since the air-flow kept its maximum value during the whole imbibition branch this type of evaluation was carried out for the drainage branch only. The effect of the preferential air path was considered by simulation of pneumatic conductivity based on the material properties and the portion of the S-I sand. When air conductivity was calculated only for this part of the sample the simulations fitted measured data better. The results for the drainage branch are shown in Figure 5.10 as dotted lines for the three air conductivity models. The slope of the curve could not be predicted by the models. The steeper increase of measured air conductivity might be a result of the integral measurement values of lower boundary pressure and saturation which were taken for data evaluation. For the $k_a(\psi)$ data-points every step was reflected by one distinct water phase pressure which was correlated to an air conductivity value. The result were discrete points of air conductivity measurements which caused a steeper increase of the curve. The $k_a(S)$ relation was considering the saturation of the whole column consisting of the S-I sand, which brought little errors since the S-II sand might have been drained

parallel to the S-I material. Even though, both simulations showed clearly the necessity of a separate simulation of the coarse textured core and the remaining part of the sample.

The distinct influence of the structure of this column with the vertical orientation made the simple concepts of averaging of pneumatic properties obsolete for this sample. The concept of emergence point saturation as a trigger for air conductivity was invalid in this case, as the air used the paths where resistivity was low and passed the sample. This effect had been seen as preferential air-flow in analogy to terminology used in solute transport problems where comparable structure elements are a shortcut for solutes. In the same manner, the coarse textured cylinder acted as a preferential flow path for air in this sample.

Hysteresis in Hydraulic and Pneumatic Properties

The hysteresis in water dynamics has been represented well by the separate sets of parameters for drainage and imbibition. For the given structure the bimodal model could be applied successfully and measured data could be fitted for the whole drainage/imbibition cycle with the known properties of the homogeneous materials. The influence of the separate fitting on the saturation conductivity relation are shown in Figure 5.10 (right) where the hysteretic hydraulic conductivity curve is also shown.

Pneumatic measurement showed strong hysteresis which could not be represented by any of the three models. Effective air conductivity of the coarse cylinder depended strongly on the history of measurement. The sample had only two states which could be detected with the measurement method used. For full water saturation there was no air conductivity measurable. The second state started with desaturation of the coarse structure element as air conductivity reached its maximum value immediately. The influence of the S-II sand on air conductivity was displaced by the strong impact of the S-I core.

The measurement of this type of structure required exact knowledge of the initial saturation of the whole sample, since hysteresis had a strong impact. The way of saturating the sample was crucial for the experimental success, since saturation by mere capillary rise could have left the "macropores" open and the experimental result would have been different. However, these effects can be used for the analysis of macropore systems, their pore continuity, tortuosity, and other geometric factors.

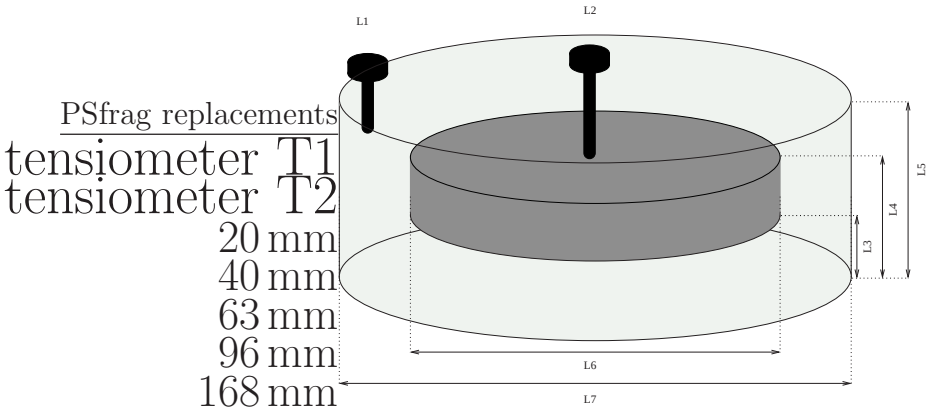

Figure 5.11: Packed sand with predefined structure – S-H-II. The major part (84 Vol. %) consists of Sand S-II (light grey) with a lens (16 Vol. %) consisting of Sand S-I (dark grey).

5.2.2 Horizontally Structured Sand Packing – S-H-II

The influence of structure on air entrapment effects was demonstrated with the horizontally structured column S-H-II. A coarse textured S-I lens was embedded into the fine S-II sand. Figure 5.11 shows the setting of the sample and the positions of two tensiometers. For the measurement of this sample, a small (3.5 mm in diameter) tensiometer was placed directly in the lens and a second tensiometer at the upper part of the column in the fine sand.

Boundary conditions were chosen with respect to measurement with the homogeneous S-II sand, which had been the dominating material for this experiment. A second demand was the availability of air conductivity measurement, accessible at pressures below $\pm 0\,\mathrm{cm}_{WC}$. The applied air pressure gradient was 4 hPa.

Experimental Results

Measured curves for this experiment are shown in Figure 5.12 (top). When the air entry was reached, at a lower boundary water pressure of $-10\,\mathrm{cm}_{WC}$ the outflow curve had a fast rise and reached a plateau. During the next two steps the S-I lens was drained resulting in a decrease of conductivity. As a result, the outflow curve had a slow rise as water from the upper part of the sample had to flow around the coarse S-I lens. The measured tensiometer potential of tensiometer 2, which was placed in the coarse lens, had been parallel to tensiometer 1 until the lens had almost dried out after 20 hours. From that point the hydraulic conductivity became too low to follow the lower boundary pressure until the water content in the lens had become 12 % after 41 hours. In the imbibition branch, dynamic effects were observed when the water had flowed back into the sample. The inflow steps showed a fast exponential response to lower boundary pressure followed by a linear part which was

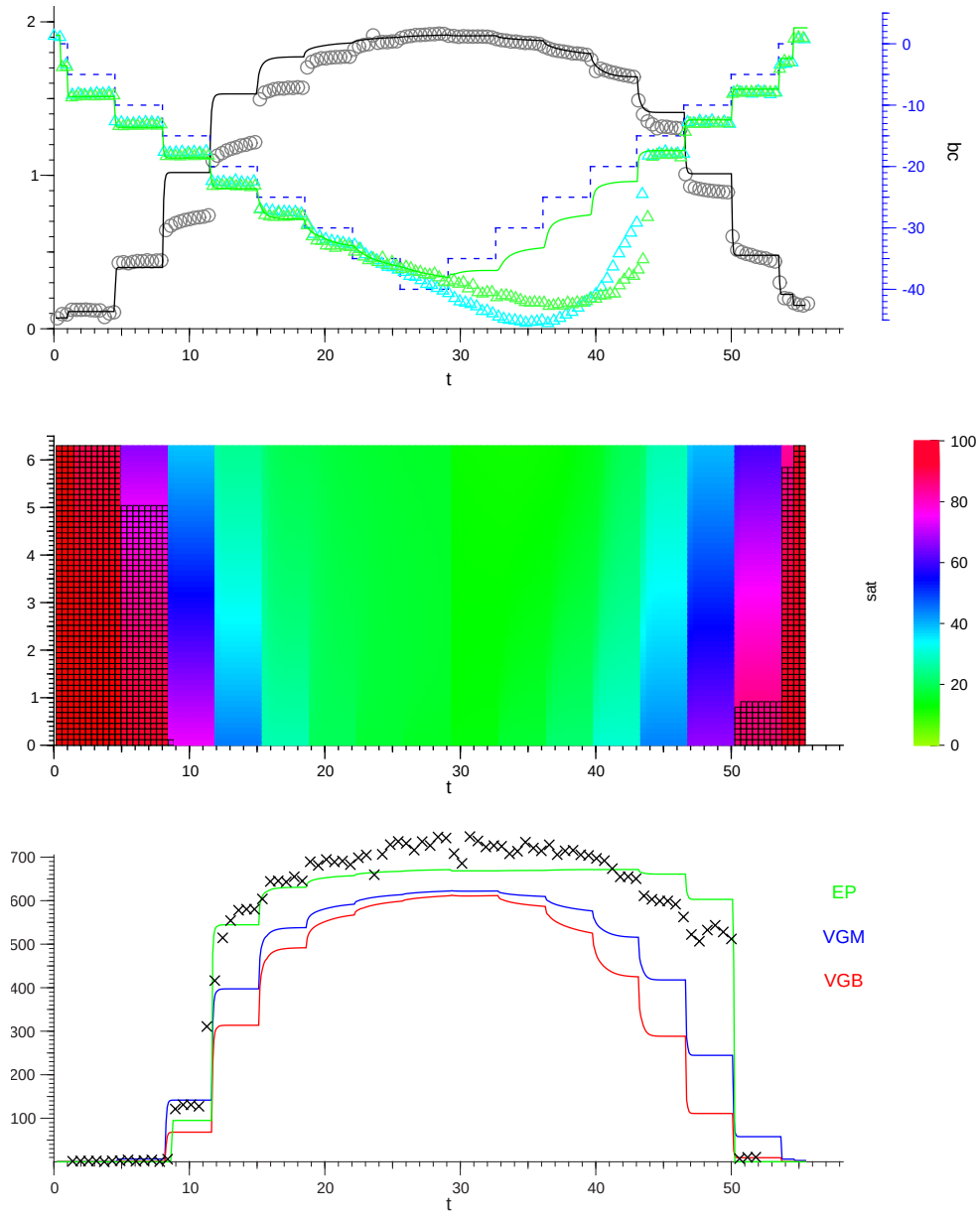

PSfrag replacements

time [h]
ve outflow [cm]
uctivity [cm/h]
essure [cm $_{WC}$]
r saturation [-]
e sample [mm]
VGM
VGB
EP

Figure 5.12: Multistep outflow and air-flow measurement with sand structure S-H-II. Top: Outflow curve (black; measured: symbols, fitted: solid line), lower boundary pressure (red dashed), tensiometer potential in fine sand (green; measured: symbols, fitted: solid line) and in coarse lens (cyan). Center: Temporal evolution of a vertical saturation profile. The black framed pixels have saturations higher than emergence point saturation used for the EP model. Bottom: Measured air conductivity (symbols) and application of VGM,VGB, and EP models.

parameter	drainage	imbibition
α_1 $[cm^{-1}]$	0.052	0.082
n_1	5.88	3.15
α_2 $[cm^{-1}]$	0.078	0.105
n_2	6.76	6.76
weight 1:2	0.16	0.16
K_{sat} $[cm/h]$	15.7	15.7
θ_s	0.39	0.39
θ_r	0.07±0.02	0.03±0.01
τ	0.67±0.05	0.57±0.12

Table 5.7: Van Genuchten parameters for heterogeneous S-H-II sample as estimated with `eshpim` and their respective 95 % confidence interval. Hysteresis was considered by separate simulation of each branch of the measured curve and influence of structure was considered by usage of a bimodal model. The values of θ_r and θ_s were fixed for simulations.

a result of air inclusions which were dissolved in the following redistribution phase. At the end of the cycle, there had been about 5 % residual air in the sample.

Gas phase continuity through the column was matched at a total water content of 14 % at a lower boundary pressure of $-15\,\mathrm{cm}_{WC}$. Conductivity rose in three steps and reached its maximum value at a water phase pressure of $-25\,\mathrm{cm}_{WC}$. In the imbibition branch conductivity showed hysteresis referring to water saturation. Continuity of the air phase was lost at a water saturation of about 30 % at the interim from the -10 to the $-5\,\mathrm{cm}_{WC}$ step.

Hydraulic Properties

Figure 5.12 (top) also shows the results of the inverse parameter estimation for the measured outflow curve which had been done with the bimodal model. The simulations are plotted in the same color as the respective measurement curve. For simulations, the tensiometer measurements of tensiometer 1 were selected as it was placed in the continuous S-II sand. For this simulation, the parameters of the homogeneous sands were fixed and only residual water saturation and tortuosity was fitted to measured data. Simulation was done separately for both branches of the measured curve.

The simulation predicted a fast outflow at the beginning of the drainage branch, caused by the coarse textured fraction. As expected for the horizontal structure the simulations did not fit the data at the -15 and $-20\,\mathrm{cm}_{WC}$ steps. This was a result of the S-I lens which still had no contact to air reservoir. For the imbibition branch simulations fitted measured data better as long as air could leave the lens. With resaturation of the S-II sand in the upper part of the column air had been

entrapped in the lens and simulation results diverge from the measurement. Parameters estimated by these simulations are listed in Table 5.7 together with the fixed parameters of the homogeneous materials.

Pneumatic Properties

For quantitative analysis of measured air conductivity data, saturation profiles were determined in two separate ways. The first approach was based on the previous knowledge of the type of structure and the material properties of the homogeneous constituents building up the structured sample. A second analysis was carried out without any preconditioned evaluation of material properties.

Based on the prior knowledge of the hydraulic properties of the homogeneous materials and the structure of the sample, air conductivity was simulated with a simplified approach. The vertical saturation profiles were calculated for the S-II sand as it had the major influence on air conductivity in this sample due to a continuity of this material and the horizontal alignment of the S-I lens. The central part of Figure 5.12 shows the temporal evolution of the saturation for a vertical profile of the sample. Air conductivity was calculated for the VGM, VGB, and EP model for the simulated saturations. Starting air-flow had been predicted by all models, but the increase of air conductivity after 11 hours could not be fitted by the VGM and VGB models and therefore both models mismatched the measured data for the rest of the drainage branch. The EP model fitted measured data best as it had the possibility to simulate the fast rise in air conductivity by adjustment of the additional emergence point saturation parameter. For the imbibition branch, both the VGM and the VGB models were not able to fit measured data as they underestimated air conductivity during the whole cycle. The EP model described the stepwise reduction of air conductivity qualitatively good but did not fit the data well. The loss of air continuity and therefore the end of the air conductivity measurement had also been fitted by the additional extinction point parameter. The underestimation of the maximum conductivity by all models was a result of the simplification of the evaluation method. The coarse S-I lense had an influence especially in the dry range of the experiment which had not been taken into account by this simulation.

For the second evaluation method no prior knowledge of the system was used. The experimental multistep outflow data was evaluated with the bimodal model for both branches of the curve. Fitting results are shown in Figure 5.13 (top). The new van Genuchten parameters which were result of these fits are listed in Table 5.8. With these sets of parameters it had been possible to fit the multistep outflow curve well but the model was not able to predict tensiometer measurements which was due to the assumption of a homogeneous distribution of the two materials reflected by the bimodal model. The saturation profiles which resulted from this simulation are shown in the center of the figure. Based on the new set of hydraulic properties and the simulated saturations the air conductivity models were applied

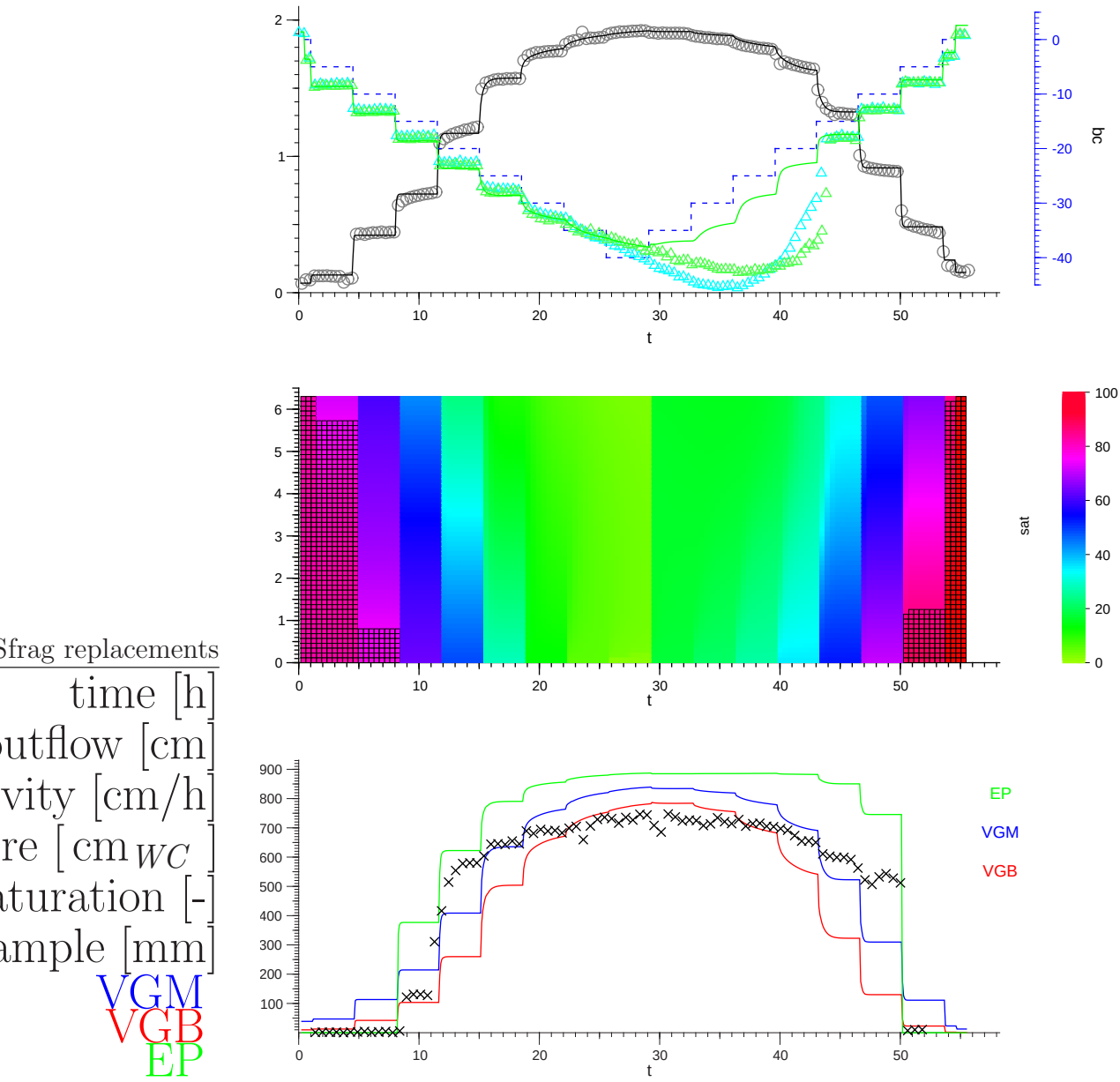

Figure 5.13: Independent evaluation of multistep outflow and air-flow measurement with sand structure S-H-II. Top: Outflow curve (black; measured: symbols, fitted: solid line), lower boundary pressure (red dashed), tensiometer potential in fine sand (green; measured: symbols, fitted: solid line) and in coarse lens (cyan). Center: Temporal evolution of a vertical saturation profile. The black framed pixels have saturations higher than the emergence point saturation used for the EP model. Bottom: Measured air conductivity (symbols) and application of VGM, VGB, and EP models.

parameter	drainage	imbibition
α_1 $[cm^{-1}]$	0.042	0.084
n_1	6.12	2.66
α_2 $[cm^{-1}]$	0.088	0.053
n_2	12.58	15.00
weight 1:2	0.83	0.91
K_{sat} $[cm/h]$	43.0	43.0
θ_s	0.32	0.37
θ_r	0.01	0.01
τ	1.05	1.55

Table 5.8: Van Genuchten parameters for heterogeneous S-H-II sample as estimated by an independent evaluation with the bimodal model. Hysteresis was considered by separate simulation of both branches.

to the temporal evolution of the saturations. The calculated air conductivities are shown in the lower part of the figure. A general effect which occurred for all three model is the overestimation of air conductivity. The coarse part of the assumed bimodal pore system had been drained fast providing continuous paths for air-flow. Especially for the VGM and the VGB model these simulations resulted in nonzero air conductivity in the first 8.5 hours of the experiment where no air-flow was detected. The same effect was observed at the end of the air-flow measurement where the models predicted a nonzero flow which was not measured. The fast changes of conductivity was best described by the EP model, but maximum air conductivity was also overestimated by this model. Altogether, the deviations between the predicted air conductivities and measured data were higher than for the simplified approach, with the known material properties and geometry although the hydraulic data was represented better by the bimodal hydraulic model.

5.3 Results of Measurement with Sand Packings

For the investigation of artificially structured samples, precise knowledge of the hydraulic and pneumatic properties of the single materials building the sample was necessary. Modeling of measured data with the Kool and Parker model combined with the van Genuchten parameterization for hydraulics and EP model for pneumatics resulted in best description of the single materials. Simulation results were able to represent measured data. For both, the S-I and the S-II sand the major deviations were in the wet and the dry range of the measurement whereas the rest was predicted well by the model. In the wet range an explicit multiphase description

would have been necessary since the assumptions made for the Richards equation might have been violated. In the dry range the parameterization did not offer enough flexibility for desrciption of the system. The observed deviations resulted in similar differences between measurements and simulations of the structured samples where the simulations were based on the material properties of the homogeneous materials.

With the fixed hydraulic properties of the homogeneous materials the simulations of the structured samples, required an adequate model. For the S-H-I sample the bimodal van Genuchten model was able to simulate measured data well, because the sample geometry met all requirements for this type of model. Pneumatic behavior could not be modeled for this structure as a whole. The models used for simulations did not reflect structure. For this case air conductivity had to be separated for all continuous structure elements. Air conductivity had to be modeled for every compartment and summed up for the whole sample to get the effective conductivity. With the knowledge of the properties of the compartments, the method can be applied for detection of vertically continuous macropore systems.

Hydraulic properties of the heterogeneous S-H-II sample could not be described by the bimodal model for the outflow branch as the coarse lens had no direct connection to the air reservoir during drainage. With the reduction to the fine textured material the pneumatic behavior could be described well. A second approach where simulations were carried out without reflecting the prior knowledge of material properties showed the connection of both the hydraulic and the pneumatic material properties.

For this type of structure explicit multidimensional simulation of the water and air dynamics of the multistep outflow and air-flow experiments would be necessary. Current simulation codes are able to use both, the van Genuchten and the Brooks and Corey parameterization (Ippisch 2001), and the more flexible type of cubic spline functions for description of the hydraulic parameters. A combination of these forward simulation programs with an adequate inversion algorithm should make parameter estimations possible, where only the structure of the sample and the multistep outflow data will be necessary.

6 Conclusions

In this study multiphase investigations were carried out on different types of porous media. For measurement of air conductivity, which is an important additional material property, an experimental device had been developed which allowed measurements of both, the hydraulic and the pneumatic state variables. The device for transient measurement of hydraulic properties within multistep outflow experiments was combined with an air permeameter which allowed simultaneous determination of air conductivity. The special lower boundary plate which was necessary for separation of phases, offered an interface to the further measurement instruments. The experimental setting was applied to two different types of porous media. Artificial sintered glass columns, a highly idealized porous media and several packings of sieved sands, representing more natural media, were examined, using the multiphase investigation approach. Although it has not been tested yet, the setup should be also suitable for the measurement of undisturbed soils. The multistep outflow part of the setup has already been tested with soil cores and with an appropriate sealing at the side boundary, it is also possible to do the additional airflow measurement.

In the case of the sintered glass material the connection between homogeneous materials and heterogeneous samples had been examined. Hydraulic properties of homogeneously textured columns were estimated from multistep outflow experiments. Measured data had been modeled inversely using the van Genuchten-Mualem parameterization with the constrained Kool and Parker approach for hysteresis. Fitting results were only satisfactory for the coarse textured material. The fine textured sintered glass required more flexibility in hysteretic hydraulic functions to describe hysteresis phenomena. For this purpose the constraint of a single conductivity function for drainage and imbibition of porous media has been released and a better description of hysteretic hydraulic functions has been achieved by the Kool and Parker model.

Measurements with a heterogeneous column, which consisted of the investigated homogeneous materials, showed important effects of structure on hydraulic and pneumatic properties. The horizontally structured sample could not be simulated with a multimodal model, when the hydraulic parameters were fixed to the values evaluated for the homogeneous samples. This was expected, as not all compartments had direct connection to air and water reservoirs throughout the whole experiment. For simulations of horizontally structured samples it would have been necessary to

use three-dimensional models based on explicit sample geometry. Furthermore there was a lack of accurate description of the hydraulic properties of homogeneous materials, as even small deviations especially in the wet and dry range lead to wrong simulations of structured samples. The van Genuchten model, with its low number of parameters and its constraint, which reduces flexibility of the function, failed especially in these ranges of saturation.

Air-flow measurements showed a sharp breakthrough of air and an increase of air conductivity due to the decreasing water saturation of the heterogeneous sample. For simulations of air conductivity it was satisfactory to simulate discrete water saturation profiles for the finer textured homogeneous material. The simulations showed that the major influence was by the lower layer of the sample which was the homogeneous lower third of the column. Continuity of air depended only on saturation of this finer material, which was continuous throughout the whole sample. Applied air permeability models described data qualitatively well. Quantitative description was best for the EP model. Simulation of air conductivity with the concept of an emergence point saturation, which was necessary to establish a continuous air phase, was the appropriate model for measured data. The VGB and VGM models which were based on a continuous air phase saturation overestimated air-flow in the wet range. Differences in the predictions of these models could be explained by the different concepts of the pore network system.

The concept of the transfer of hydraulic and pneumatic properties of homogeneous materials to heterogeneous samples was successfully demonstrated with the repacked sands. Estimation of hysteretic hydraulic properties for the coarse homogeneous sand was done with the constrained Kool and Parker model. The fine textured sand required the more flexible model. Resulting hysteretic hydraulic functions did not contradict physical principles within the measurement range. Measurement of additional scanning loops confirmed the evaluation method. Modeling of air-flow measurements based on forward simulations with estimated hydraulic properties was best with the EP model. Here, the emergence and extinction point saturations were almost constant for the scanning cycles.

Investigations with structured columns clearly showed the effect of the orientation of structure elements. For simulations of hydraulic and pneumatic properties of the structured samples, all information available from homogeneous materials was used. For the vertically structured sample a multimodal model could be used for description of hydraulics, but all air-flow models failed if both materials were considered with their respective shares as the coarse structure element acted as a preferential flow path for air. The separation of this macropore system led to better results in air conductivity predictions, if the simulations were based only on the coarse textured material.

The influence of the different horizontal layers within a sample could be shown with a second structured column. One-dimensional modeling of air conductivity could be based on the continuous fine sand only where the influence of the coarse

lense became visible only in the dry range. A comparison of two different simulations of this experiment showed the connection between hydraulic and pneumatic properties. A bimodal best fit of hydraulic data without any prior knowledge of the sample, could not fit the measured air-flow data, since the model did not reflect the influence of structure. The pressure-saturation hysteresis for this sample was causally connected to processes at two distinct scales. The residual air at the end of the multistep outflow experiment could be assigned to both the texture of the materials, where capillary effects were dominant, and additionally to the structure, where the coarse lense was embedded in the fine material.

The experiments showed that sample structure had an enormous impact on combined measurements. Effects which could not have been seen with a multistep outflow experiment were observed by the additional air-flow measurement. The vertical structure resulted in little outflow of water but had a fast breakthrough of air. Continuous preferential flow paths in vertical direction were found in fast experiment over a wide pressure range. Classically they have been detected by transport experiments at one specific saturation. For scanning a specific pressure range several tracers had to be used in very time consuming experiments. The horizontally structured sample showed the necessity for multidimensional simulations where enclosed structure elements could be represented. The bimodal model which was used was not able to predict the experimental results.

Determination of unsaturated air conductivity from hydraulic properties required a rescaling of the effective saturation as proposed by the EP model. The fast rise in air conductivity with decreasing water saturation at a specific emergence point, to a maximum value which is almost fixed over a wide range of saturation could be described best by a rescaling of both, the maximum and the residual water saturation parameters. Although both fluids share the same pore space the effective saturations of both could not be seen complementary. The experimental evidence for the different effective pore systems should be incorporated into future air conductivity modeling.

Bibliography

Averjanov, S. F. 1950. About permeability of subsurface soils in case of incomplete saturation. Engineering Collection VII:19–21.

Ball, B. C., W. Harris, and J. R. Burford. 1981. A laboratory method to measure gas diffusion and flow in soil and other porous materials. Journal of Soil Science 32:323–333.

Bear, J. 1972. Dynamics of Fluids in Porous Media. Elsevier New York.

Blunt, M. J. 2001. Flow in porous media - pore network models and multiphase flow. Current Opinion in Colloid and Interface Science 6:197–207.

Brooks, R. H. 1980. Water retention measurement for soils. Journal of Irrigation and Drainage Div. 106:105–112.

Brooks, R. H., and A. T. Corey. 1964. Hydraulic properties of porous media. Hydrol. Pap. 3, Colorado State University, Fort Collins, CO p. 27pp.

Brooks, R. H., and A. T. Corey. 1966. Properties of porous media affecting fluid flow. J. Irrigation and Drainage 92:61–88.

Brutsaert, W. 1967. Some methods of calculating unsaturated permeability. Trans. ASAE 10:400–404.

Brutsaert, W. 2000. A concise parameterization of the hydraulic conductivity of unsaturated soils. Advances in Water Resources 23:811–815.

Buckingham, E. 1907. Studies on the movement of soil moisture. Vol. Bulletin 38. U.S. Department of Agriculture, Bureau of Soils, Washington, D.C.

Burdine, N. T. 1953. Relative permeability calculations from pore-size distribution data. Trans. Am. Inst. Min. Metall. Pet. Eng. 198:71–78.

Campbell, G. S. 1974. A simple model for determining unsaturated hydraulic conductivity from moisture retention data. Soil Science 117:311–314.

Caputo, M. 2000. Models of flux in porous media with memory. Water Resources Research 36:693–705.

Celia, M. A., E. T. Bouloutas, and R. L. Zarba. 1990. A general mass-conservative numerical solution for the unsaturated flow equation. Water Resources Research 26:1483–1496.

Chatzis, I., and F. A. L. Dullien. 1983. Dynamic immiscible displacement mechanisms in pore doublets: Theory versus experiment. Journal of Colloid and Interface Science 91:199–222.

Chavent, G., G. Cohen, and M. Espy. 1980. Determination of relative permeabilities and capillary pressures by an automatic adjustment method. Paper SPE 9237 presented at the 1980 SPE Annual Technical Conference and Exhibition, Dallas, Sept 21-24.

Childs, E. C., and N. Collis-George. 1950. The permeability of porous materials. Proc. Royal Soc. London 201A:392–405.

Colonna, J., F. Brissaud, and J. L. Millet. 1972. Evolution of capillarity and relative permeability hysteresis. Trans. Am. Inst. Min. Metall. Pet. Eng. 253:28–38.

Corey, A. T. 1954. The interrelation between gas and oil relative permeabilities. Prod. Mon. 19:32–41.

Corey, A. T. 1986. Air permeability. Methods of Soil Analysis, Part 1. Physical and Mineralogical Methods. American Society of Agronomy - Soil Science Society of America. p. 1121–1136.

Corey, A. T. 1994. Mechanics of immiscible fluids in porous media. 3rd edition. Water Resources Publications, Highlands Ranch, Colorado.

Corey, A. T., and R. H. Brooks. 1975. Drainage characteristics of soils. Soil Science Society of America, Proceedings 39:251–255.

Corey, A. T., and R. H. Brooks. 1999. The brooks-corey relationship. Characterization and Measurement of the Hydraulic Properties of Unsaturated Porous Media, Proceeding of the international Workshop in Riverside, California Part 1:13–18.

van Dam, J. C., J. Stricker, and P. Droogers. 1994. Inverse method to determine soil hydraulic functions from multistep outflow experiments. Soil Science Society of America, Journal 58:647–652.

van Dam, J. C., N. M. Stricker, and P. Droogers. 1992. Inverse method for determining soil hydraulic functions from one-step outflow experiments. Soil Science Society of America, Journal 56:1042–1050.

Darcy, H. 1856. Les Fontaines de la Ville de Dijon. Dalmont, Paris.

Dixon, R. M., and D. R. Linden. 1972. Soil-air pressure and water infiltration under border irrigation. Soil Science Society of America, Proceedings 36:948–953.

Dullien, F. A. L. 1979. Porous media fluid transport and pore structure. Academic Press, New York, NY.

Dullien, F. A. L., C. Zarcone, I. F. MacDonald, A. Collins, and R. D. E. Bochard. 1988. The effects of surface roughness on the capillary pressure curves and the heights of capillary rise in glass bead packs. Journal of Colloid and Interface Science 127:362–373.

Durner, W. 1994. Hydraulic conductivity estimation for soils with heterogeneous pore structure. Water Resources Research 30:211–223.

Durner, W., B. Schultze, and T. Zurmühl. 1999. State-of-the-art in inverse modeling of inflow/outflow experiments. Characterization and Measurement of the Hydraulic Properties of Unsaturated Porous Media. Vol. Part 1. p. 661–681.

Durner, W., S. Bitterlich, and P. Knabner. 2001. Bestimmung parameterfreier bodenhydrologischer Eigenschaften aus instationären Fließexperimenten durch inverse Simulation. Mitteilungen Deutsche Bodenkundliche Gesellschaft.

Dury, O. 1997. Organic pollutants in unsaturated soils: Effect of butanol as a model contaminant on phase saturation and flow characteristics of a quartz sand packing.. PhD thesis. ETH Zürich, Switzerland.

Dury, O., U. Fischer, and R. Schulin. 1998. Dependence of hydraulic and pneumatic characteristics of soils on a dissolved organic compound. Journal of Contaminant Hydrology 33:39–57.

Dury, O., U. Fischer, and R. Schulin. 1999. A comparison of relative nonwetting-phase permeability models. Water Resources Research 35:1481–1493.

Faybishenko, B. A. 1995. Hydraulic behavior of quasi-saturated soils in the presence of entrapped air: Laboratory experiments. Water Resources Research 31:2421–2435.

Fischer, U., O. Dury, H. Flühler, and M. T. van Genuchten. 1997. Modeling nonwetting-phase relative permeability accounting for a discontinuous nonwetting phase. Soil Science Society of America, Journal 61:1348–1354.

Fischer, U., R. Schulin, and M. Keller. 1996. Experimental and numerical investigation of soil vapor extraction. Water Resources Research 32:3413–3427.

Friedman, S. P. 1999. Dynamic contact angle explanation of flow rate-dependent saturation-pressure relationships during transient liquid flow in unsaturated porous media. J. Adhesion Sci Technol. 13:1495–1518.

Fulton, P. F. 1951. The effect of gas slippage on relative permeability measurements. Prod. Mon. p. 14–19.

Gee, G. W., A. L. Ward, Z. F. Zhang, G. S. Campbell, and J. Mathson. 2002. The influence of hydraulic nonequilibrium on pressure plate data. Vadose Zone Journal 1:172–178.

van Genuchten, M. T. 1980. A closed-from equation for predicting the hydraulic conductivity of unsaturated soils. Soil Science Society of America, Journal 44:892–898.

Gerthsen, C., H. O. Kneser, and H. Vogel. 1992. Physik. 16. Auflage. Springer-Verlag, Berlin.

Hassanizadeh, S. M., M. A. Celia, and H. K. Dahle. 2002. Dynamic effect in the capillary pressure-saturation relationship and its impacts on unsaturated flow. Vadose Zone Journal 1:38–57.

Hoffmann-Riem, H., M. T. van Genuchten, and H. Flühler. 1999. General model for the hydraulic conductivity of unsaturated soils. Characterization and Measurement of the Hydraulic Properties of Unsaturated Porous Media, Proceeding of the international Workshop in Riverside, California.

Hollenbeck, K. J., and K. H. Jensen. 1999. Dependence of apparent unsaturated parameters on experiment type and estimation method. International Workshop on Characterization and Measurement of the Hydraulic Properties of Unsaturated Porous Media. Riverside, California.

Honarpour, M., L. Koederitz, and H. Harvey. 1986. Relative permeability of petroleum reservoirs. CRC p. 143pp.

Hopmans, J. W., J. Šimůnek, N. Romano, and W. Durner. 2003. Inverse methods. chapter 3 The Soil Solution Phase. p. 963–1008. Methods of Soil Analysis. 3rd edition. Soil Science Society of America.

Instruments, N. 2001. LabView 6i, Version 6.0.2. National Instruments, www.ni.com.

Ippisch, O. 2001. Coupled Transport in Natural Porous Media. PhD thesis. University of Heidelberg. www.ub.uni-heidelberg.de/archiv/1872.

Klinkenberg, L. J. 1941. The permeability of porous media to liquids and gases.

Klute, A., and C. Dirksen. 1986. Methods of Soil Analysis. chapter 28 Hydraulic Conductivity and Diffusivity: Laboratory Methods. p. 687–734. Vol. 1. 2nd Edition. Soil Science Society of America.

Kool, J. B., and J. C. Parker. 1987. Development and evaluation of closed form expressions for hysteretic soil hydraulic properties. Water Resources Research 23:105–114.

Kool, J. B., J. C. Parker, and M. T. van Genuchten. 1985. Determining soil hydraulic properties from one-step outflow experiments by parameter estimation: I.Theory and numerical studies. Soil Science Society of America, Journal 49:1348–1359.

Kozeny, J. 1927. Über kapillare Leitung des Wassers im Boden. Forschungsbericht 136, Sitzungsberichte Akadademie der Wissenschaften, Wien Mathematisch-Naturwissenschaftliche Abteilung IIa.: 271-306.

Lenhard, R. J., and J. C. Parker. 1987. A model for hysteretic constitutive relations governing multiphase flow, 2. Permeability-saturation relations. Water Resources Research 23:2197–2206.

Lenhard, R. J., J. C. Parker, and S. Mishra. 1989. On the correspondence between Brooks-Corey and van Genuchten models. Journal of Irrigation and Drainage Engineering 115:744–751.

Lenhard, R. J., T. G. Johnson, and J. C. Parker. 1993. Experimental observations of nonaqueous-phase liquids subsurface movement. Journal of Contaminant Hydrology 12:79–101.

Leverett, M. C. 1939. Flow of oil-wate mixtures through unconsolidated sands. Trans AIME 132:381–401.

Lide, D. R., and H. P. R. Frederikse. (ed.) 1996. Handbook of Chemistry and Physics. 76th Edition. CRC Press, Boca Raton, New York, London, Tokyo.

Lu, T. X., J. W. Biggar, and D. R. Nielsen. 1994. Water movement in glass bead porous media 1. Experiments of capillary rise and hysteresis. Water Resources Research 30:3275–3281.

Luckner, L., M. T. van Genuchten, and D. R. Nielsen. 1989. A consistent set of parametric models for the two-phase flow of immiscible fluids in the subsurface. Water Resources Research 25:2187–2193.

Miller, E. E., and R. D. Miller. 1956. Physical theory for capillary flow phenomena. Journal of Applied Physics 27:324–332.

Moldrup, P., T. G. Poulsen, P. Schjønning, T. Olesen, and T. Yamaguchi. 1998. Gas permeability in undisturbed soils: Measurement and predictive models. Soil Science 163:180–189.

Moldrup, P., T. Olesen, T. Komatsu, P. Schjønning, and D. E. Rolston. 2001. Tortuosity, diffusivity, and permeability in the soil liquid and gaseous phase. Soil Science Society of America, Journal 65:613–623.

Mortensen, A., R. Glass, K. Hollenbeck, and K. H. Jensen. 2001. Visualization of microscale phase displacement processes in retention and outflow experiments: Nununiqueness of unsaturated flow properties. Water Resources Research 37:1627–1640.

Mualem, Y. 1974. A conceptual model of hysteresis. Water Resources Research 10:514–520.

Mualem, Y. 1976. A new model for predicting the hydraulic conductivity for unsaturated porous media. Water Resources Research 12:513–522.

Mualem, Y. 1984. A modified dependent domain theory of hysteresis. Soil Science 137:283–291.

Mualem, Y., and G. Dagan. 1978. Hydraulic conductivity of soils: Unified approach to the statistical models. Soil Science Society of America, Journal 42:392–395.

Muskat, M., and M. W. Meres. 1936. The flow of heterogeneous fluids through porous media. Physics 7:346–363.

Naar, J., R. J. Wygal, and J. H. Henderson. 1972. Imbibition relative permeability in unconsolidated porous media. Soc. Pet. Eng. J. 2:13–17.

Nielsen, D. R., M. T. van Genuchten, and J. W. Biggar. 1986. Water flow and solute transport processes in the unsaturated zone. Water Resources Research 22:89S–108S.

Parker, J. C., and R. J. Lenhard. 1987. A model for hysteretic constitutive relations governing multiphase flow 1. Saturation-pressure relation. Water Resources Research 23:2187–2196.

Parker, J. C., R. J. Lenhard, and T. Kuppusamy. 1987. A parametric model for constitutive properties governing multiphase flow in porous media. Water Resources Research 23:618–624.

Parlange, J.-Y. 1976. Capillary hysteresis and the relationship between drying and wetting curves. Water Resources Research 12:224–228.

Pirson, S. J. 1958. Oil Reservoir Engineering. McGraw Hill, New York.

Poulovassilis, A. 1969. The effect of hysteresis of pore-water on the hydraulic conductivity. Journal of Soil Science 20:52–56.

Poulovassilis, A., and E. Tzimas. 1975. The hysteresis in the relationship between hydraulic conductivity and soil water content. Soil Science 120:327–331.

Prunty, L., and F. X. M. Casey. 2002. Soil water retention curve description using a flexible smooth function. Vadose Zone Journal 1:179–185.

Richards, L. A. 1931. Capillary conduction of liquids through porous mediums. Physics 1:318–333.

Ross, P. J., and K. R. J. Smetten. 1993. Describing soil hydraulic properties with sums of simple functions. Soil Science Society of America, Journal 57:26–29.

Roth, K. 1996. Lecture Notes in Soil Physics. University of Heidelberg, www.iup.uni-heidelberg.de/institut/forschung/groups/ts/students/lecture_notes /soil_physics/all.ps.gz

Schultze, B. 1998. Optimierung der Messung bodenhydraulischer Eigenschaften durch inverse Simulation von Aus- und Rückflussexperimenten an Bodensäulen. PhD thesis. Universität Bayreuth.

Schulz, V. 2003. Description and reconstruction of microscopic random heterogeneous media in order to estimate macroscopic hydraulic functions. PhD thesis. University of Heidelberg. www.ub.uni-heidelberg.de/archiv/3691.

Scott, P. S., G. J. Farquhar, and N. Kouwen. 1983. Hysteretic effects on net infiltration. Advances in Infiltration 11:163–170.

Šimůnek, J., T. Vogel, and M. T. van Genuchten. 1994. The SWMS_2D code for simulating water flow and solute transport in two-dimensional variably saturated media. U.S. Salinity Laboratory, USDA/ARS. Riverside, CA.

Stonestrom, D. A., and J. Rubin. 1989a. Air permeability and trapped-air content in two soils. Water Resources Research 25:1959–1969.

Stonestrom, D. A., and J. Rubin. 1989b. Water content dependence of trapped air in two soils. Water Resources Research 25:1947–1958.

Toorman, A. F., P. J. Wierenga, and R. G. Hills. 1992. Parameter estimation of hydraulic properties from one-step outflow data. Water Resources Research 28:3021–3028.

Topp, G. C. 1969. Soil-water hysteresis measured in a sandy loam and compared with the hysteretic domain model. Soil Science Society of America, Proceedings 33:645–651.

Topp, G. C., A. Klute, and D. B. Peters. 1967. Comparison of water content-pressure head data obtained by equilibrium, steady state, and unsteady state methods. Soil Science Society of America, Proceedings 31:312–314.

Topp, G. C., and E. E. Miller. 1966. Hysteretic moisture characteristics and hydraulic conductivities for glass-bead media. Soil Science Society of America, Proceedings 30:156–162.

Ustohal, P., F. Stauffer, and T. Dracos. 1998. Measurements and modeling of hydraulic characteristics of unsaturated porous media with mixed wettability. Journal of Contaminant Hydrology 33:5–37.

Viaene, P., H. Vereecken, J. Diels, and J. Feyen. 1994. A statistical analysis of six hysteresis models for the moisture retention characteristic. Soil Science 157:345–355.

Vogel, H.-J., and K. Roth. 2002. Moving through scales of flow and transport in soil. European Journal of Soil Science 272:95–106.

Vogel, H.-J., K. Roth, and P. Bastian. 2002. Using bulk density measured by X-ray tomography to estimate the hydraulic structure of soil. Transactions 17th World Congress of Soil Science, Bangkok, 2002. p. 1218/1–1218/9.

Vogel, T., M. T. van Genuchten, and M. Cislerova. 2001. Effect of the shape of the soil hydraulic functions near saturation on variably-saturated flow predictions. Advances in Water Resources 24:133–144.

White, N. F., D. K. Sunada, H. R. Duke, and A. T. Corey. 1972. Boundary effects in desaturation of porous media. Soil Science 113:7–12.

Wildenschild, D., and J. Hopmans. 1999. Flow rate dependence of hydraulic properties of unsaturated porous media. Characterization and Measurement of the Hydraulic Properties of Unsaturated Porous Media, Proceeding of the international Workshop in Riverside, California p. 893–904.

Wildenschild, D., J. W. Hopmans, and J. Simunek. 2001. Flow rate dependence of soil hydraulic characteristics. Soil Science Society of America, Journal 65:35–48.

Wu, Y. S., K. Pruess, and P. Persoff. 1998. Gas flow in porous media with Klinkenberg Effects. Transport in Porous Media 32:117–137.

Wyllie, M. R. J. 1962. Relative permeability. chapter vol. 2 Reservoir Engineering. p. 25.1–25.14. Petroleum Production Handbook. Soc. of Pet. Eng., Richardson, Tex.

Zurmühl, T. 1994. Validierung konvektiv-dispersiver Modelle zur Berechnung des instationären Stofftransports in ungestörten Bodensäulen. PhD thesis. Universität Bayreuth.

Zurmühl, T. 1996. Evaluation of different boundary conditions for independent determination of hydraulic parameters using outflow methods. Parameter Identification and Inverse Problems in Hydrology, Geology and Ecology p. 165–184.

Zurmühl, T., and W. Durner. 1998. Determination of parameters for bimodal hydraulic functions by inverse modeling. Soil Science Society of America, Journal 62:874–880.

Appendix

.

A Setup

A.1 Pressure Sensors

The sensors used are from the Honeywell[1] PC26 series with the technical features:

model	26PCBFA6G	26PCAF6D
mode	absolute	differential
pressure range	±5.0 psi	±1.0 psi
max. overpressure	20.0 psi	20.0 psi
compensated	yes	yes
response time	1 ms max.	1 ms max.
linearity	0.40% span. typ., 0.50% span. max.	0.25% span. typ., 0.50% span. max.
typical sensitivity	10 mV/psi	16.7 mV/psi
null offset	0 mV typ.	0 mV typ.
repeatability and hysteresis error	0.20% span. typ.	0.20% span. typ.
operating temperature range	-40 ℃ to 80 ℃	-40 ℃ to 80 ℃

A.2 Experimental problems

The rigid structure was one of the main features provided by the sintered glass columns. This advantage of the material was necessary during the test stage of the experimental setup as the experiments had been redone several times for development of the setting and exclusion measurement artifacts[2]. Some of these artifacts, as well as, if possible, a reason for the removal of their effects should be documented

[1] www.honeywell.com

[2] A fixed medium offers the best possibility for comparison of experiments carried out at the same setup. Differences in measured data between two measurements with the same boundary conditions has to be artifacts from anywhere in the whole measurement procedure.

in this extra section, as they may help other scientists avoid some troubles or even give focus to details, which are not obviously troublesome, but which may cause a lot of confusion.

- Never use any random type of glue for fixing porous glass plates. Some glues shrink a little while they harden and the developing shear forces can kill the glass plates.

- A major problem for gas flow experiments is the sealing of the samples. For this study several casings were tested for the glass samples. Latex casings were too weak and widened with increasing water pressure, resin was drawn in the pores of the sample and reduced the available porosity, additionally there is the problem of some vapor of a solvent which might influence surface properties. Best results were achieved by shrinking PVC tubes. They produced no surface active vapors and when fixed onto the samples they were rigid within the required pressure range.

- Never use silicone in the whole setup, as the vapor is an highly active surfactant, which repelles water efficiently and makes the porous material hydrophobic. This is true for all kinds of sealing such as lower or side boundaries, tensiometers, and TDR.

- As a soil column may have a weight of a few kilograms, the separator plate must be able to withstand this. The first approach, using a plastic grid glued in the funnel below the plate failed, as it bent till the plate cracked. A monolithic design where the plate holder and the supporting grid were milled from a single piece of plastic was much stiffer.

- The optimal way to calibrate the pressure sensors for tensiometer and lower boundary pressures was a two step procedure. In the first step the slope of the sensor (cm water-column vs. digit output) had been measured with a hanging water-column and in the second step the offset was fixed when the sensor was installed and the applied pressure is well known, e.g., in a fully saturated sample, the tensiometer pressure at a specific depth is well known.

- One of the major problems in porous plate experiments is the diffusion of air below the plate. As it is not at all possible to suppress this effect, it is necessary to have an insight on the funnel below the plate in order to monitor this effect and to convince its influence on the experiment. I quit using deaired water, since this was only effective in the initial state of the experiment. After some scanning cycles the water was exposed to air and mixed again.

- The hydraulic contact between the porous plate and the sample has to be at a maximum level. To reach this, a contact material was used for the rigid

media. The material must be thin enough not to influence the experiment, its hydraulic permeability larger than the investigated material, and it has to be permeable to air. For these purposes a gauze had been the most useful because there were fine textured filaments for the water and large wholes for the air.

- Since I forgot to poison the samples in the beginning some type of bacteria or other, grew there. Cleaning the samples with acetone, sulphuric acid, and caustic soda aided in removing these organisms in the columns and caused an increase of saturated conductivity to the values measured in the first tests.
- Different bubbling outlets for the Mariotte Bubble Tower were tested. On the one hand the smaller they were the better the resolution of the measurement but on the other a small jet was of larger resistance and the applied pressure had to be adjusted higher.

This list may be an incentive for scientists to do the same as there is not enough time for everyone to make the same mistakes him- or herself.

B Sintered glass

The sintered glass material, used for the investigations in Chapter 4 should be briefly characterized. The borosilicate glass 3.3 is specified as a standard glass - it contains mainly sand, calcium carbonate and sodium carbonate. Actually this material is taken for several filter purposes. The technical data provided by the manufacturer is given here.

B.1 Chemical composition

The following is a typical analysis of borosilicate glass 3.3:

Element	% by weight
Silica ($Si0_2$)	80.60
Boric oxide (B_20_3)	12.60
Sodium oxide (Na_20)	4.20
Alumina (Al_20_3)	2.20
Iron oxide (Fe_20_3)	0.40
Calcium oxide (Ca0)	0.10
Magnesium oxide (Mg0)	0.05
Chlorine (Cl)	0.10

There may exist heavy metals in a concentration of less than 5 ppm.

B.2 Physical Properties

Coefficient of Expansion	$33{\cdot}10^{-7}$/°C between 20 °C - 300 °C
Specific Heat	750 J/kg°C at 20 °C
Thermal Conductivity	1.13 W/K·m at 20 °C
Density	2.23 x 103 kg/m³
Poisson's Ratio	0.22 between 25 °C - 400 °C
Young's Modulus	6.500 kg/mm² at 25 °C
Rigidity Modulus E	62,5 kN/mm²
DPH (Vickers) Hardness	580 Kg/mm² with 50 gram load
Relative Hardness	1.52 (comparative Soda-Lime = 1.0)
Refractive Index	1.474 Sodium D - Line
Dielectric Constant	4.6 at 1 MHz and 20 °C

B.3 Influence of Sample Structure on Transport Processes

The structure of the heterogeneous sintered glass sample was build with respect to the influence on water and solute transport at different states of saturation. Numerical simulations with the two-dimensional flow simulation code `swms` (Šimůnek et al. 1994) were carried out to visualize the effect. The hydraulic properties of the homogeneous materials were set as estimated in the experiments (Chapter 4). To the initially dry samples a permanent flow at the upper boundary was applied and the development of the flow field in the column was calculated. When equilibrium was reached, the saturations, water pressures and the fluxes in the column were stored. Simulation of solute transport was done by a particle tracker where the formerly calculated hydraulic states were used. Based on the flow field 10.000 particles were introduced at the nodes of the upper surface. The propagation of the particles in time was based on the stochastic velocity field generated by `swms` and an additional random walk took molecular diffusion and subscale hydrodynamic dispersion in consideration. The ways the particles moved through the samples were tracked. Concentrations were calculated by dividing the number of particles in a small region by the volume of that region (Roth 1996, p. 106).

The results of simulations are shown in Figure B.1 for a low flow rate at the upper boundary. The applied flow was $10^{-12}\,m^3/s$ and simulation was calculated for $10^{10}\,s$. The upper part of the figure shows the saturation for the steady state (left), the pressure inside the column (center), and the flow field (right). The results of particle tracking are shown in the lower part where the concentration is shown for three travel times to visualize the development of the particle plume in the flow field. The plume was divided into two parts. One part had already passed whereas the other part was stored above the coarse lens. These particles were transported very slowly since they had to move around the lens where the flow rates were low.

For the high flow rate ($10^{-2}\,m^3/s$) the steady state was reached after $10^8\,s$. Figure B.2 shows the saturation, pressure, and flow field for this case. In the saturation plot the lenses cannot be identified anymore since the entire column was fully saturated. The lower part of the figure shows the shape of the tracer plume which is totally different from the first case. On its way down the plume was only shaped by the different conductivities of the lenses but kept together.

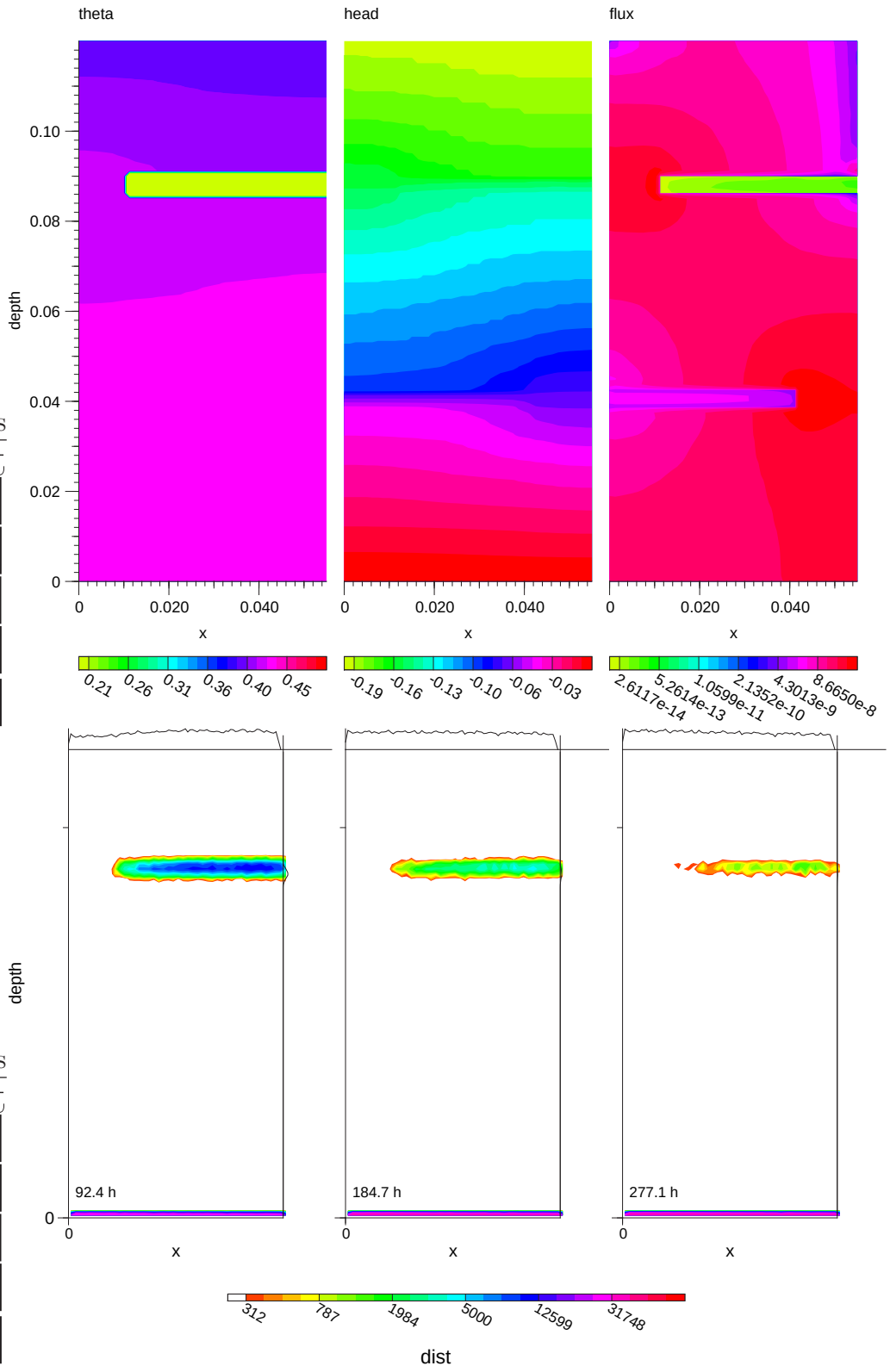

Sfrag replacements
ater content
depth z [m]
x [m]
re head [m]
$|j_w|$ [m/s]
e PDF [m^2]

Sfrag replacements
ater content
depth z [m]
x [m]
re head [m]
$|j_w|$ [m/s]
e PDF [m^2]

Figure B.1: 2-d simulation of water dynamics in the heterogeneous sintered glass column at a low flow-rate. Top: saturation (left), pressure (center), and flow field (right). Bottom: Temporal evolution of the particle plume.

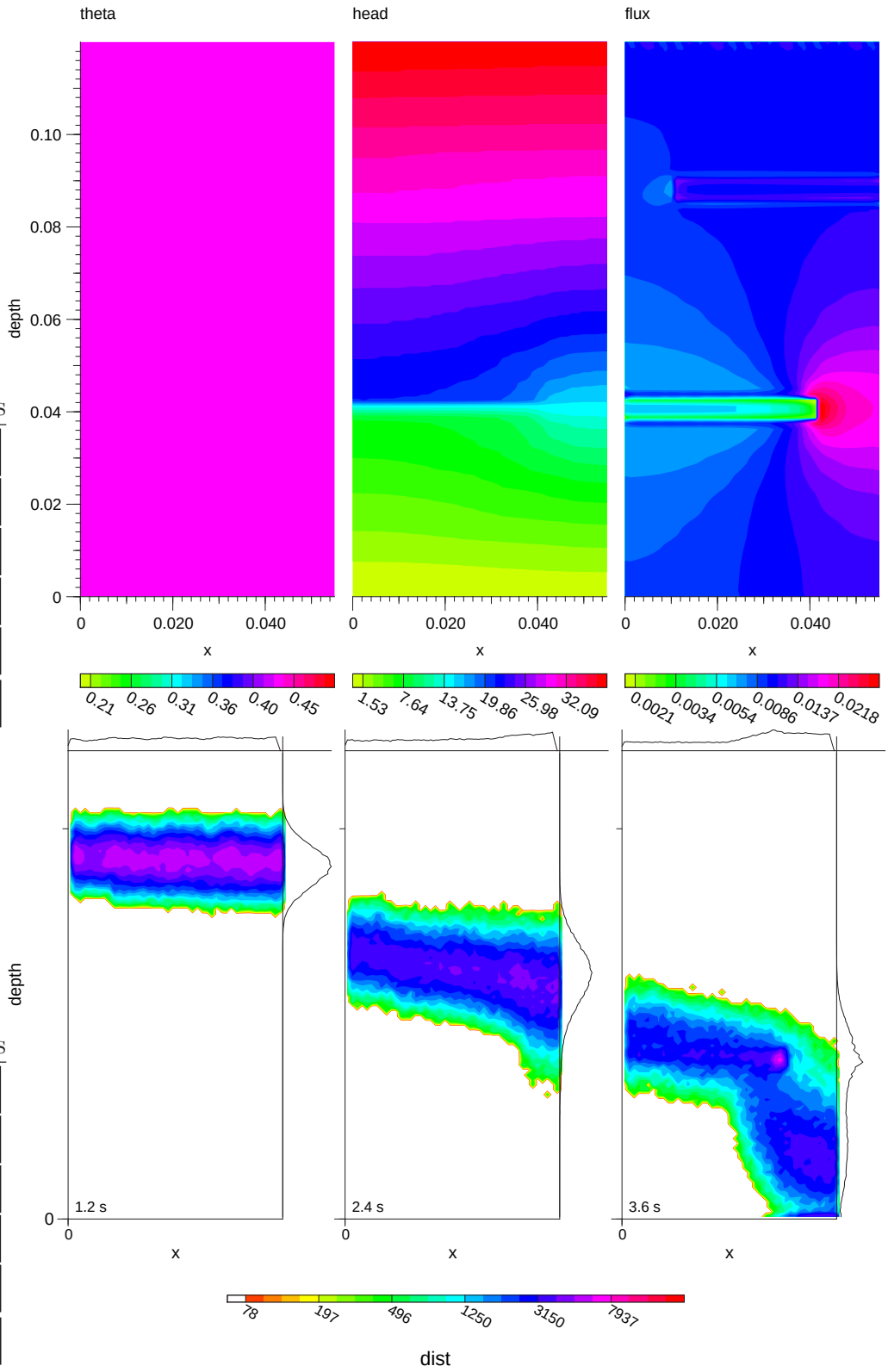

PSfrag replacements
ater content [-]]
depth z [m]
x [m]
essure head [m]
$|j_w|$ [m/s]
ance PDF [m^2]

PSfrag replacements
ater content [-]]
depth z [m]
x [m]
essure head [m]
$|j_w|$ [m/s]
ance PDF [m^2]

Figure B.2: 2-d simulation of water dynamics in the heterogeneous sintered glass column at a high flow-rate. Top: saturation (left), pressure (center), and flow field (right). Bottom: Temporal evolution of the particle plume.